

UC Berkeley

UC Berkeley Electronic Theses and Dissertations

Title

Rates and Mechanisms of Magmatic Processes: Isotopic and Geochronological Evidence

Permalink

<https://escholarship.org/uc/item/43t5w2hh>

Author

Peterson, Brook Thomas

Publication Date

2013

Peer reviewed|Thesis/dissertation

**Rates and Mechanisms of Magmatic Processes:
Isotopic and Geochronological Evidence**

by

Brook Thomas Peterson

A dissertation submitted in partial satisfaction of the
requirements for the degree of
Doctor of Philosophy

in

Earth and Planetary Science

in the

Graduate Division

of the

University of California, Berkeley

Committee in charge:

Professor Donald J. DePaolo, Chair
Professor Paul Renne
Professor M. Steve Shackley

Fall 2013

**Rates and Mechanisms of Magmatic Processes:
Isotopic and Geochronological Evidence**

Copyright 2013
by
Brook Thomas Peterson

Abstract

Rates and Mechanisms of Magmatic Processes: Isotopic and Geochronological Evidence

by

Brook Thomas Peterson

Doctor of Philosophy in Earth and Planetary Sciences

University of California, Berkeley

Professor Donald J. DePaolo, Chair

Magmatism has played an integral part in the evolution of the Earth through geologic time. Mantle-derived mafic magmatism is a primary mechanism by which the bulk silicate Earth segregated into mantle and crust, and the continental crust has further differentiated through metamorphism, anatexis, and assimilation. The study of magmatic processes has given rise to our understanding of how the Earth has evolved.

Central to this understanding are chemical, isotopic, and geochronological studies. Chemical and isotopic studies provide unparalleled richness of information; this is especially true now, as technological advances extend our analytical and computational capabilities. The difficulties presented in geochemical field studies of magmatic processes are primarily twofold: we are mostly limited to surface samples at the end of their evolutionary story (while the processes of interest are those occurring from source to surface), and it can be difficult to disentangle the myriad causes that produce the chemical and isotopic effects observed. These difficulties can be addressed by combined geochemical-geophysical-geospatial studies, by computational modeling based on an extensive (and growing) body of thermodynamic data, and by application of novel geochemical techniques.

As with chemical data, geochronological data are fundamental descriptors in their own right, but they are also crucial because they anchor rates. Almost all geologic processes or features are rate-dependent, from growth of crystals on an atomic scale, to morphologies of volcanoes, to the evolution of the crust. An understanding of chronologies and rates is therefore fundamental to understanding the processes of magmatic evolution.

The diverse chapters in this thesis reflect my diverse interests in the Earth sciences, but all are motivated by desire to understand both fundamental aspects of the chemical evolution of magmas, and how that evolution informs our broader understanding of volcanoes, volcanic fields, and continental crust evolution.

The first chapter is a geochemical study of the San Francisco Volcanic Field in central Arizona. In this study, I combine geochemical, geochronological, geospatial, and isotopic data with the computational thermodynamic modeling package alphaMELTS to understand the chemical evolution of the volcanic magmas from source to surface. I show that the

isotopic and chemical characteristics of the SFVF can be largely explained by assimilation of the deep crust by parent magma derived from fertilized asthenospheric mantle. The computational treatment with alphaMELTS allows for quantitative limits to be placed on the mineralogy, chemistry, and dynamics of the source of the volcanic field.

The second chapter is a geochronological study of magmas from the Hawaii Scientific Drilling Project phase 2 core. This study works to extend the U–Th/He dating technique to olivine phenocrysts in relatively undegassed submarine basalts, rocks which are normally difficult to date by other chronometers.

The third chapter investigates the evolution of felsic magma chemistries and the changing nature of continental crust source rocks during the Himalayan collision. In this study, I apply relatively new (Mg, Ca) and established (Sr, Nd) isotopic techniques to a sample suite of diverse crustal lithologies (primarily granitoids and felsic volcanics) from the Lhasa, Tibet region. I show that Ca and Mg isotopes are sensitive to specific mineralogies and processes, including carbonate-bearing shale assimilation, and that the Ca and Mg isotopic systems are promising tools in studies of granite petrogenesis, metamorphism, assimilation, and subduction recycling.

To the doctors, David Sinclair and James Peterson

And most of all to Cynthia

Contents

Contents	ii
List of Figures	iv
List of Tables	vi
1 The geochemistry of the San Francisco Volcanic Field: anatomy of a mid-sized intraplate volcanic system from source to surface	1
1.1 Introduction	1
1.2 Background	5
1.3 Samples	9
1.4 Data	9
1.5 Magma evolution by assimilation / fractional crystallization	14
1.6 Implications for mantle processes	26
1.7 Conclusions	35
2 U–Th/He dating and $^3\text{He}/^4\text{He}$ of Late Pleistocene submarine tholeiitic basalt from the Hawaii Scientific Drilling Project core (HSDP–2)	50
2.1 Introduction	50
2.2 Procedure	51
2.3 He data	55
2.4 Magmatic $^3\text{He}/^4\text{He}$ of the deep core	58
2.5 Provisional U–Th/He Ages	59
2.6 Sources of orphaned ^3He	63
2.7 Conclusions	66
3 Ca–Mg isotopic probe of granite petrogenesis: Lhasa region, Tibet	71
3.1 Introduction	71
3.2 Background	72
3.3 Procedures	77
3.4 Results	80
3.5 Discussion	84

3.6 Conclusions	87
A Isenthalpic AFC modeling with alphaMELTS	97
Bibliography	103

List of Figures

1.1	Distribution of Cenozoic volcanism in the southwestern United States	2
1.2	Volcanism volumes and durations plot	3
1.3	Maps of the SFVF and surrounding region	6
1.4	Total alkali-silica diagram for SFVF magmas	8
1.5	SFVF sample location maps with isotopic data	10
1.6	Major element covariation diagrams for SFVF magmas	11
1.7	Trace elements in SFVF magmas	12
1.8	Rare Earth Elements in SFVF magmas	13
1.9	Isotopic data for SFVF magmas	19
1.10	SFVF Isotopic covariation with magmatic evolution	22
1.11	Example output of a single alphaMELTS 2-stage AFC model run	24
1.12	Plot of calculated SFVF magma production rates for the AFC ensemble	28
1.13	Comparison of SFVF magmas and experimentally-generated melts of different mantle lithologies	29
1.14	Trace element results of non-modal batch melting calculations	30
1.15	Non-modal batch melting calculations in Yb-La space	31
1.16	Geobarometry and Geothermometry of SFVF samples.	32
2.1	Schematic overview of the U–Th/He procedure	52
2.2	Comparison between hot, 1500° C furnace blanks, 500° C extractions, and 1500° C extractions	54
2.3	Spectrometry data for sample 02AMK7B, 1500° C extraction	56
2.4	$^3\text{He}/^4\text{He}$ (as R/R_A) for Hawaiian lavas	57
2.5	HSDP–2 core U–Th/He ages	60
2.6	Evaluations of crushing efficiency	61
2.7	Calculated cosmogenic “exposure ages” for HSDP–2 samples	65
3.1	Simplified geologic map of the Lhasa block	73
3.2	Sr and Nd isotopes for Lhasa-region plutonic and volcanic rocks	74
3.3	Map of the study area surrounding Lhasa, Tibet	75
3.4	Comparison of $\delta^{26}\text{Mg}_{DSM3}$ standards from this study with values from the literature	78

3.5	Unspiked $^{40}\text{Ca}/^{44}\text{Ca}$ standards by date	80
3.6	ε_{Ca} vs ε_{Nd} for samples in this study	81
3.7	$\delta^{26}\text{Mg}$ and $\delta^{44}\text{Ca}$ for Lhasa-region samples	83
3.8	Dy_N/Yb_N vs $\delta^{26}\text{Mg}$	86
3.9	Comparison of leached and unleached Jiding Ophiolite samples	87
A.1	Major element covariation diagrams for full AFC ensemble results	101

List of Tables

1.1	SFVF Major and trace elements	37
1.2	SFVF isotopic data	44
1.3	Major and trace element inputs for SFVF AFC modeling	47
1.4	Isotopic inputs for SFVF AFC modeling	49
2.1	Hawaiian He data	68
2.2	U–Th/He ages	70
3.1	Lhasa-region Major and trace elements	89
3.2	Lhasa-region isotopic data	93
A.1	Input parameters for SFVF AFC modeling	102

Acknowledgments

This thesis was made possible through the assistance, generosity, understanding, and patience of faculty, staff researchers, colleagues, collaborators, students, friends, and family. My adviser, Don DePaolo, deserves my deepest thanks, as do my committee members Paul Renne and Steve Shackley; and the talented researchers at Lawrence Berkeley National Lab, especially Mack Kennedy, John Christensen, and Shaun Brown. I owe thanks to the technicians and staff whose assistance has been invaluable: Tom Owens, Marilyn Saarni, Micaelee Ellswythe, Sean Mulcahy, Margie Winn, and Tim Teague; to my collaborators Qing-Zhu Yin and Josh Wimpenny; and to undergraduate assistants Evan Kha, Tayler Hildreth, Brooke Rumley, and Wingyee Lee. I benefitted enormously from my interactions with fellow grads; in particular, I thank Karrie Weaver, Victoria Lee, Jim Watkins, Laura Nielsen, Max Rudolph, Leif Karlstrom, and Chris Huber for their discussions, suggestions, and for pushing me. I thank Bruce Nelson for introducing me to isotope geochemistry.

Part of the work constituting this thesis was funded by the Esper S. Larsen Jr. Research Fund; I extend my thanks to Eva A. Larsen for her endowment.

Staying sane in graduate school is not easy; if I achieved it at all, it was through the support of my parents, Maggie and Jon, my brothers Blake and Brian, and my circle of friends. In particular, I'd like to thank Switch Thomas, Suga Hickox, Jesper and Jessie Andersen, the Mexico Crew, and Michelle Medina for their love, support, and laughter.

I owe my deepest gratitude to my love, my wife, Cynthia. This could not have happened without her.

Chapter 1

The geochemistry of the San Francisco Volcanic Field: anatomy of a mid-sized intraplate volcanic system from source to surface

1.1 Introduction

Studies of volcano locations, volumes, types of edifices, eruptive rates, and chemical and isotopic compositions have been crucial to understanding mantle chemical geodynamics, tectonics, and the complex interplay between the two. The plate boundary features that dominate the global volcanic flux – the mid-ocean ridge systems and the subduction arcs – are understood in context of global tectonics. Less geographically or temporally persistent, and less understood, are intraplate volcanic systems and their underlying causes. Intraplate volcanism produces only 5% of the global volcanic flux (Crisp, 1984), but intraplate provinces are ubiquitous, and examples can be found on every continent. In North America, Cenozoic intraplate volcanism is widespread across the southwestern United States (Figure 1.1).

Intraplate provinces range in size, lifespan, productivity, and chemical composition, and the individual volcanic features within these provinces are also variable. In particular, the presence or lack of central volcanoes, and the sizes, morphologies, compositions, and eruptive styles can be related to growth rates and magmatic fluxes feeding the system (Figure 1.2). For a typical volcanic field with an area of 1000 km^2 and total eruption rate of $\sim 100 \text{ km}^3 / \text{Myr}$ ($10^{-7} \text{ km}^3/\text{km}^2/\text{yr}$) magma fluxes are insufficient to evolve central volcanoes, resulting in monogenetic fields. The majority of arc volcanoes have growth rates above this threshold, as do the intraplate San Francisco and the Taos Plateau Volcanic Fields. Higher flux rates ($\sim 10^{-2}$ to $10^{-3} \text{ km}^3/\text{km}^2/\text{yr}$), produce persistent silicic caldera-forming volcanic systems, such as Long Valley and Yellowstone, and vigorous arc volcanoes. At higher rates still (0.1 to $1 \text{ km}^3/\text{km}^2/\text{yr}$) are the flood basalts and ocean island hotspots attributed to mantle

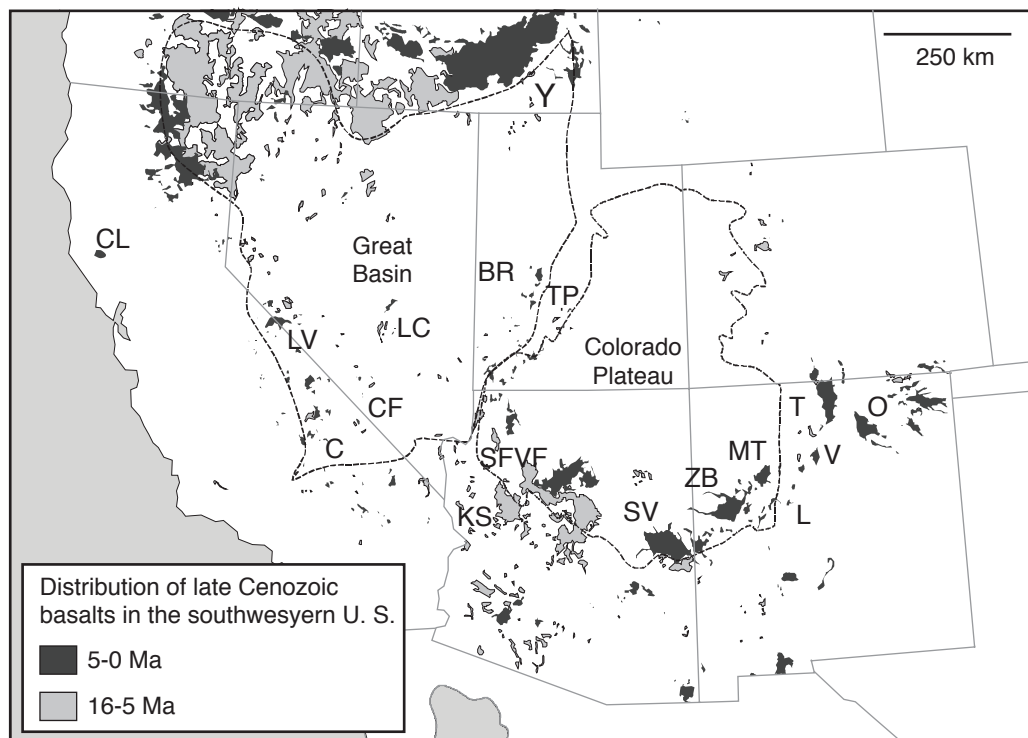


Figure 1.1: Distribution of Cenozoic volcanism in the southwestern United States (after Perry, Crowe, Valentine, and Bowker, 1998). Labels are: Y (Yellowstone), CL (Clear Lake), LV (Long Valley), C (Coso), CF (Crater Flat), LC (Lunar Crater), BR (Black Rock), KS (Kaiser Spring), TP (Twin Peaks), SFVF (San Francisco Volcanic Field), SV (Springerville), ZB (Zuni-Bandera), MT (Mount Taylor), T (Taos), V (Valles Caldera), O (Ocate), L (Lucero).

plumes.

The Hawaiian hot spot is one of the most studied examples of a long-lived, high-flux intraplate system and provides a frame of reference with regard to magma fluxes or eruption rates. The average Hawaiian volcano has a volume of roughly $35,000 \text{ km}^3$, accumulated over a time span of about 1 Myr, and has an area of about 1000 km^2 that covers the summit region where most eruptions occur. The average eruption rate is therefore about $0.035 \text{ km}^3/\text{km}^2/\text{yr}$; peak eruption rates are typically closer to $0.1 \text{ km}^3/\text{km}^2/\text{yr}$, at the lower end of the range for flood basalts. The total eruption rate for all volcanoes is typically about 50% higher than the peak rate for an individual volcano. The islands are constructed of large mafic shield volcanoes fed by persistent plumbing systems; the melting column is deep, extensive, and upwells quickly; and isotopic and tomographic evidence suggest a vigorous dynamic mantle source, probably a deep mantle plume (e.g. Watson & McKenzie, 1991; DePaolo & Stolper, 1996; DePaolo, Bryce, Dodson, Shuster, & Kennedy, 2001; C. J. Wolfe et al., 2011). In contrast, numerous, low-flux monogenetic fields are scattered across the United States Basin and Range province. These small-volume fields typically have low eruptive

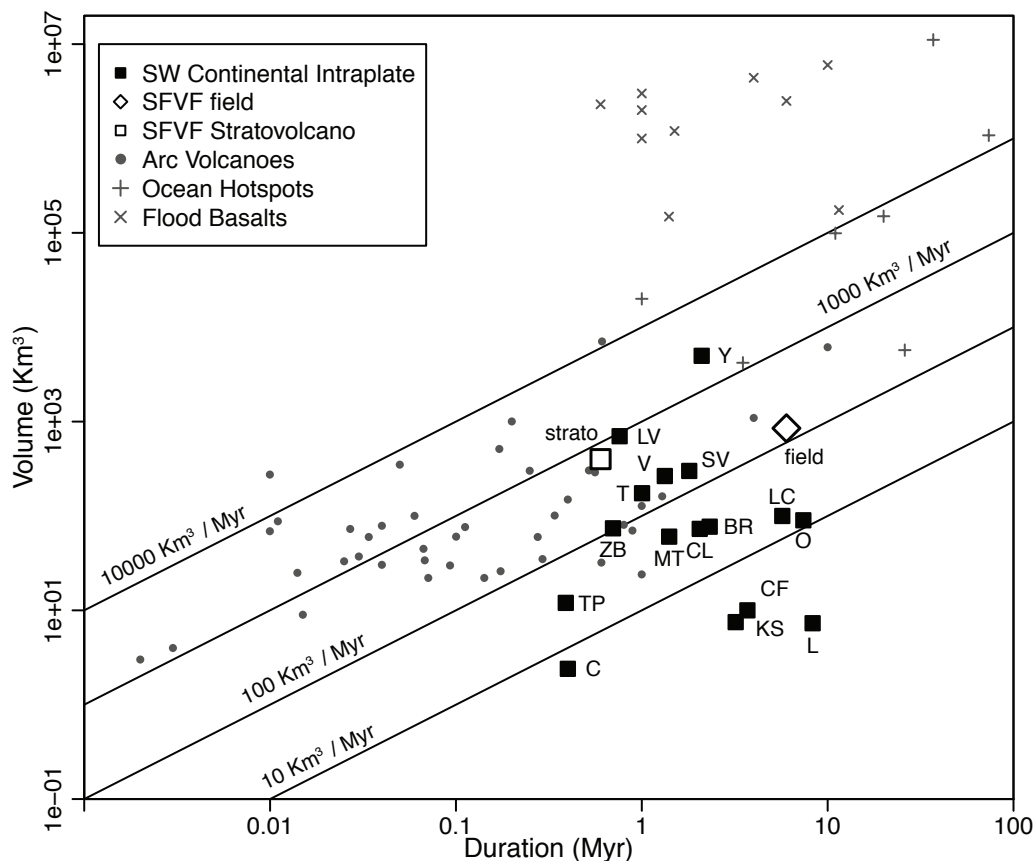


Figure 1.2: Volumes and durations plot. Diagonal lines show constant production rates. Data are from White, Crisp, and Spera (2006), Perry, Crowe, Valentine, and Bowker (1998), Wood and Kienle (1990), Laughlin et al. (1993). Arc volcano data (both continental and oceanic) are for specific volcanoes; flood basalt and oceanic hotspot data are for entire provinces. Open diamond is the total SFVF (“field”) and open square indicates just SF Mountain (“strato”). Filled squares show intraplate volcanic fields of Figure 1.1.

rates and lack persistent central plumbing systems or central volcanoes. Isotopic evidence suggests many form during passive (or nearly passive) upwelling of asthenosphere coincident with lithospheric extension (Bradshaw, Hawkesworth, & Gallagher, 1993; DePaolo & Daley, 2000).

The causes for many intermediate, “mid-range” ($\sim 10^{-2}$ to 10^{-3} $\text{km}^3/\text{km}^2/\text{yr}$) intraplate volcanic fields and “flare ups” are not presently well understood. Productivities in many of these fields are too high to be explained by lithospheric extension and/or passive upwelling, but are inconsistent with deep mantle plumes. Diverse individual models have been proposed, but they can be divided into three broad categories:

1. Mini-plumes. Based on seismic observations of low-velocity zones and perturbed mantle transition zones beneath certain volcanic provinces, small plumes, plumelets, or

mini-plumes (possibly extending to the ~ 400 km transition zone) have been proposed to explain the Erebus volcanic province and some Cenozoic European volcanic fields (Granet, Wilson, & Achauer, 1995; Ritter, Jordan, Christensen, & Achauer, 2001; Gupta, Zhao, & Rai, 2009).

2. Small-scale, edge-driven convection. Some Colorado Plateau volcanic fields, the Newer Volcanic Field, and other intraplate volcanic fields have been attributed to mantle upwelling associated with small-scale convection, generally thought to arise due to sublithospheric topography or lateral steps in lithospheric thickness (King & Anderson, 1998; King & Ritsema, 2000; Demidjuk et al., 2007; King, 2007; van Wijk et al., 2010). Models of edge-driven convection are consistent with the locations of seismic low-velocity mantle regions, thought to be lower viscosity downgoing portions of convection cells (e.g. King and Ritsema, 2000, in Africa and South America), with anisotropy indicative of lateral mantle flow, and V_P/V_S anomalies (X. Wang et al., 2008; Schmandt & Humphreys, 2010).
3. Delamination. Numerous processes fit under the “delamination” umbrella, including convective instability, drips, and hydration weakening; I use this term to describe any process of coupled deep lithospheric root removal and upwelling mantle return flow (R. W. Kay and S. M. Kay, 1993; and see recent summary by Krystopowicz and Currie, 2013). Delamination has been suggested as a source of Colorado Plateau uplift and volcanism (Bird, 1979; Lastowka, Sheehan, & Schneider, 2001), and the presence of delaminated or “dripping” lithospheric material has recently been inferred from USArray data beneath the Colorado Plateau (Levander, Schmandt, et al., 2011). Magmatism associated with delamination has been attributed to direct melting of delaminated material, melting of hydrated mantle following delamination, and to decompression melting of upwelling asthenosphere during return flow (Elkins-Tanton, 2005; Lustrino, 2005).

Hybrid conceptual models have also been proposed, where, for instance, an upwelling plume or a downgoing drip may interact with (or cause) small-scale convection (e.g. Geldmacher, Hoernle, Bogaard, Duggen, & Werner, 2005; Reid et al., 2012).

In addition to geophysical observations, quantification and modeling of the geochemistry, volumes, migration, and eruption rates of intraplate volcanic fields can provide constraints on the mantle and continental dynamics that give rise to intraplate volcanism, and further refine the above models. The San Francisco Volcanic Field (SFVF), located in Arizona, on the edge of the Colorado Plateau in the southwest United States (Figure 1.3) is ideal for a specific case study: it is easily accessible, and it was the subject of an extensive USGS field study that produced detailed maps and major element data for ~ 1200 samples (Robinson, 1913; Moore & E. W. Wolfe, 1987; E. W. Wolfe, Newhall, & Ulrich, 1987; E. W. Wolfe, Ulrich, Holm, Moore, & Newhall, 1987; Newhall, Ulrich, & Wolfe, 1987; Ulrich & Bailey, 1987). Its age progression is well-characterized by both radiometric and paleomagnetic data (Tanaka, Shoemaker, Ulrich, & Wolfe, 1986; Conway, Connor, et al., 1998), and the lithospheric and

asthenospheric structure have been recently mapped from USArray data (Bashir, Gao, Liu, & Mickus, 2011; Levander, Schmandt, et al., 2011). Over the past three decades, the SFVF has been included in several regional geochemical studies exploring the volcanism of the southwestern United States (Alibert, Michard, & Albarede, 1986; Beard & C. M. Johnson, 1997; Reid et al., 2012). To date, however, there have been only limited isotopic studies focused on the field itself (Brookins & Moore, 1975).

Although no plume structure has been seismically imaged beneath the SFVF, the field displays certain plume-like characteristics, including radial symmetry (distal, or marginal low-flux monogenetic, mafic eruptions contemporaneous with central, higher flux composite volcanoes), and migration of volcanism through time. The northeastward migration is roughly consistent with the passage of the North American plate over a quasi-stationary source. Models previously invoked to explain the SFVF - generally either delamination and edge-driven convection, or some combination of the two (but see also Roy, Jordan, and Pederson, 2009) - do not predict the plume-like characteristics of the field.

The broader purpose of this study is to advance the understanding of intraplate continental volcanism not easily associated with a subduction zone or a large mantle plume, where both central volcanoes and extensive monogenetic cinder cones are present in one field. Specifically, my goal is to understand both the shallow processes responsible for the diversity of erupted magmas, and the sources giving rise to the SFVF. Toward that end, I spend the first part of this chapter developing a 2-stage assimilation / fractional crystallization model (AFC) which I use to explain the isotopic and elemental trends in the SFVF magmas. In the second part, based on the geochemistry in primitive SFVF samples and results from the model, I make inferences about the source composition and dynamics, and review models for the genesis of the SFVF and other intraplate volcanic systems. My approach is chiefly geochemical, but I rely on additional constraints provided by geophysical, geospatial, and geochronological data.

1.2 Background

1.2.1 The Field

The SFVF is a late Cenozoic clustering of volcanic vents and evolved complexes located in north-central Arizona, on the topographic high along the southwest edge of the physiographic Colorado Plateau (Figure 1.3). It is one of a series of relatively large fields – collectively known as the Transition Zone (TZ) volcanic fields – that ring the edge of the plateau (Figure 1.1). In this sense, “Transition Zone” refers to the region where the lithosphere-asthenosphere boundary shallows from >100 km, beneath the Colorado Plateau, to ~ 50 km, beneath the Basin and Range, and not to the physiographic region of broken topography between the Colorado Plateau and Basin and Range. The SFVF includes 5 prominent silicic centers and more than six hundred basaltic vents, giving rise to flows and numerous cinder cones. Approximately 850 km^3 of erupted rocks cover $\sim 4500 \text{ km}^2$ of 2-km thick, roughly

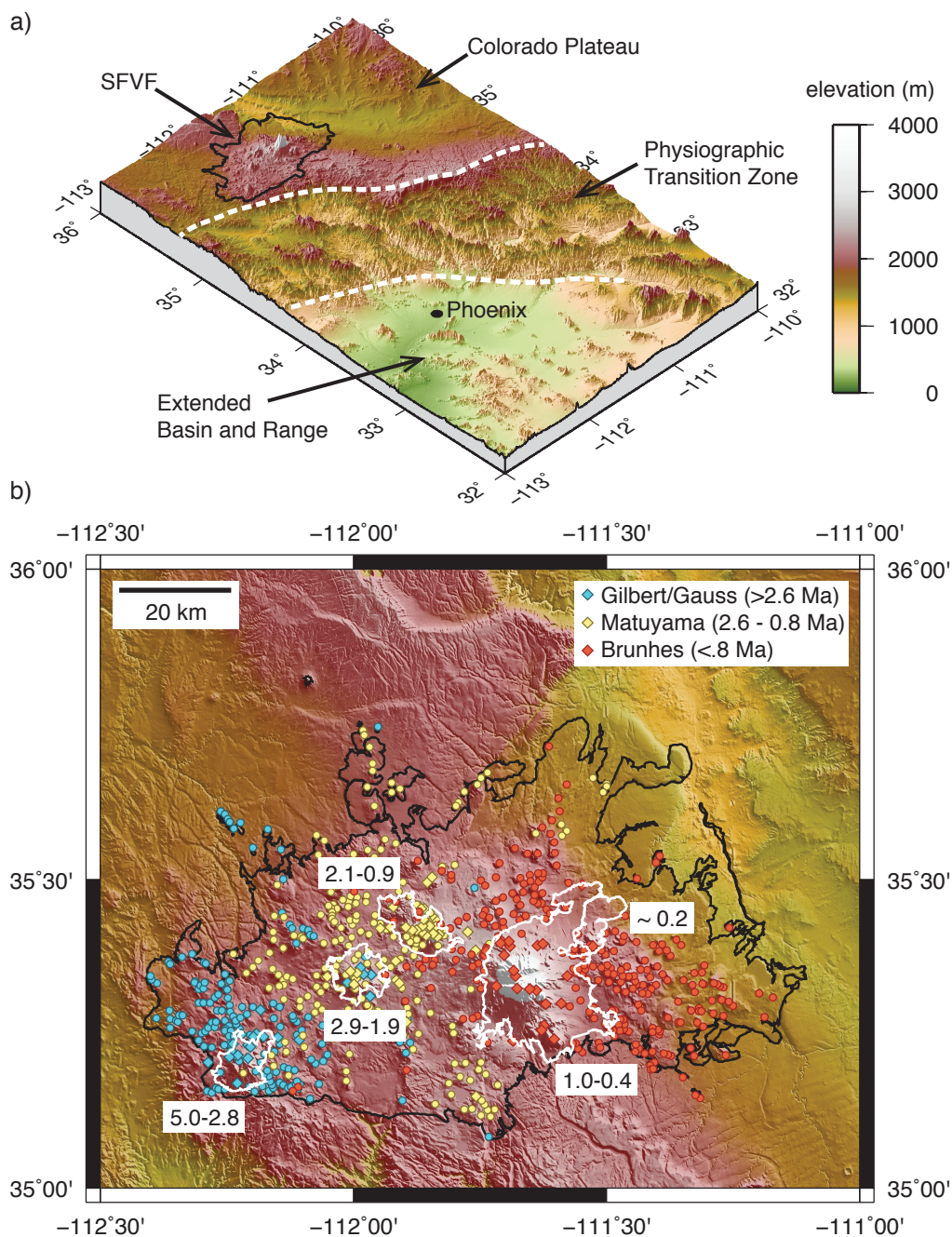


Figure 1.3: Maps of the SFVF and surrounding region. (a) shows vertically-exaggerated 3D perspective plot of the SFVF and surroundings. (b) shows the field outlined in black. Major silicic centers are outlined in white; numbers give K/Ar age ranges (Newhall et al., 1987; Wolfe, et al., 1987; Moore and Wolfe, 1987). Points are paleomagnetic data from Tanaka et al. (1986), color coded by age.

horizontal, Paleozoic and Mesozoic sediments (E. W. Wolfe, Newhall, & Ulrich, 1987). Basement rocks in the region are Proterozoic. The field lies within the Yavapai province defined by Bowring and Karlstrom (1990), and straddling the boundary of two lithotectonic blocks of differing Nd model age ($T_{DM} = 1.7\text{--}1.8$ Ga to the south, $1.8\text{--}2.0$ Ga to the north; Bennett and DePaolo, 1987). Structural features in the region include sub-parallel, \sim NE-striking, normal fault systems (including the Mesa Butte and Cedar Ranch Faults), believed to be Precambrian faults re-activated during the late Cenozoic (E. W. Wolfe, Newhall, & Ulrich, 1987; Wittke, Smith, & Wooden, 1989). It is likely that these and other inferred faults have exerted some control on the spatial distribution of volcanism, resulting in NE-striking linear chains of cinder cones and SW-NE-elongated silicic centers (Mullaney, 1996; Conway, Ferrill, et al., 1997; Morgan et al., 2004).

In addition to numerous mafic flows and cones erupted in the SFVF, the field includes \sim 12 evolved centers. Some are small extrusions of felsic magma. Five (Bill Williams Mountain, Sitgreaves Mountain, Kendrick Peak, Government Mountain, and O’Leary Peak) are sizeable silicic composite cones and domes, and one is a large, extinct (active from $1\text{--}0.4$ Ma), intermediate stratovolcano. The stratovolcano has a present volume of \sim 180 km³, but appears to have suffered sector collapse, possibly from an explosive, Mt. St. Helens-type eruption, and is heavily eroded; its maximum volume may have been closer to 350 or 400 km³. Prominent peaks in the remaining edifice are individually named and collectively known as the San Francisco Peaks; for purposes of this research, I refer to the stratovolcano edifice as SF Mountain.

The field is currently active; the most recent eruption (at Sunset Crater) occurred about 1 ka (Smiley, 1958; Ort, Elson, & Champion, 2002). Oldest flows in the field were erupted \sim 6 Ma, although this distinction is semi-arbitrary, as the SFVF is effectively the continuation of Neogene magmatism (erupted to the south and southwest) back to \sim 15 Ma. The field has migrated over time; oldest eruptions were in the southwest and youngest eruptions in the east (Figure 1.3b; Tanaka et al., 1986; Conway, Connor, et al., 1998). The magmatic flux has changed through the field’s history, qualitatively apparent from the $1.0\text{--}0.4$ Ma construction of SF Mountain. This change is also reflected in the formation rate of mafic vents, which increased from \sim 1 vent per 17 kyr in pre-Matuyama time, to \sim 1 per 8 kyr in the Matuyama and \sim 1 per 3 kyr in the Brunhes. Recent production has slowed; only \sim 20 vents have been produced during the last 100 kyr (\sim 1 per 5 kyr; Tanaka et al., 1986).

SFVF magmas range from basalt/trachybasalt to rhyolite, and are generally trachytic and weakly alkaline (Figure 1.4). Their evolution may be variable, depending on the particular magmas involved. Both shallow seismic surveys and geochemical studies of SF Mountain suggest crystal fractionation in a semi-persistent network or chamber was an important differentiation mechanism (Durrani, Doser, Keller, & Hearn, 1999; Stauber, 1982; Wenrich-Verbeek, 1979). In contrast, neighboring mafic flows may have entirely independent differentiation histories from one another (Mullaney, 1996), and the diversity of products at the smaller evolved centers, such as O’Leary Peak, appears to have been due to crustal melting and magma mixing rather than significant fractionation (Bloomfield & Arculus, 1989). Isotopic evidence suggests that even monogenetic, mafic magmas have undergone some amount of

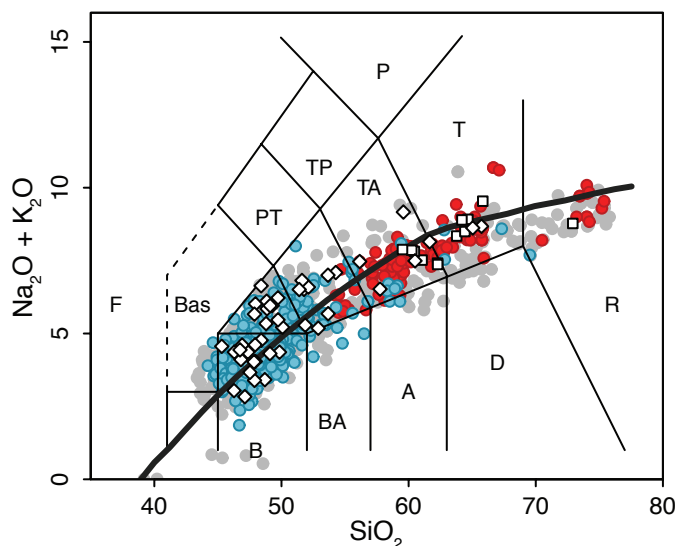


Figure 1.4: Total alkali-silica diagram of Le Bas and Streckeisen (1991), showing SFVF magma compositions. The solid line of Irvine and Baragar (1971) distinguishes between alkaline / subalkaline fields. Circles are USGS data (Moore & E. W. Wolfe, 1987; E. W. Wolfe, Newhall, & Ulrich, 1987; E. W. Wolfe, Ulrich, et al., 1987; Newhall et al., 1987); red are SF Mountain magmas, blue are Brunhes-aged monogenetic samples, gray are samples from the remainder of the field (Matuyama and older). Squares and diamonds are SF Mountain and monogenetic flows analyzed in this study, respectively.

deep crust assimilation (e.g. Alibert et al., 1986).

Geochemical and isotopic studies suggest that Colorado Plateau TZ mantle sources are mixtures of heterogeneous, enriched mantle (generally thought to be the subcontinental lithospheric mantle, enriched by metasomatic fluids, pyroxenite veins, or subducted sediment) and depleted asthenospheric mantle (Everson, 1979; Perry, Baldrige, & DePaolo, 1987; Cooper & W. K. Hart, 1990; Kempton, Fitton, Hawkesworth, & Ormerod, 1991; Beard & C. M. Johnson, 1997; Reid et al., 2012).

1.2.2 Transition Zone lithospheric structure

In the TZ beneath the SFVF, the crust thickens from 30–35 km in the eastern Basin and Range to 45 km beneath the Colorado Plateau (Zandt, Myers, & Wallace, 1995; Durrani et al., 1999). Seismic and gravity studies, and analyses of xenoliths entrained in SFVF magmas, suggest that a lower density upper crust ($\sim 2750 \text{ kg/m}^3$) extends to ~ 20 km, and is underlain by mafic to ultramafic ($\sim 2900\text{--}3100 \text{ kg/m}^3$) deep crust (W. Chen & Arculus, 1995; Bashir et al., 2011). The lithosphere-asthenosphere boundary (LAB) also deepens, from ~ 60 km beneath the Basin and Range to >100 km beneath the central Colorado Plateau; beneath the SFVF, the boundary is at ~ 75 km (Levander, Schmandt, et al., 2011; Levander & Miller, 2012). The TZ volcanic fields, including the SFVF, are located above a region of seismically

slow, high- V_P/V_S mantle at 80–100 km depth that encircles the southern Colorado Plateau (Levander, Schmandt, et al., 2011; Reid et al., 2012). Variations in seismic velocities and V_P/V_S in this region have been attributed to variable mantle melt content (up to 1% retained partial melt), temperature contrasts of several hundred degrees over lateral distances as small as 100 km, and variable water contents (Schmandt & Humphreys, 2010; Sine et al., 2008).

1.3 Samples

In order to investigate the plume-like characteristics of the SFVF, I have divided the field into two major units: SF Mountain (from which 12 samples were collected), and the surrounding monogenetic flows and cones (44 samples; locations are shown in Figure 1.5). To evaluate a snapshot in time (consistent with the 1–0.4 Ma age of SF Mountain), monogenetic samples were selected from flows known to be <1 Ma (constrained by K/Ar dates and field relations, or mapped as Brunhes). Samples were collected from flow interiors lacking obvious secondary mineralization.

Monogenetic samples are commonly vesicular and aphyric or microcrystalline. Dominant matrix phases include plagioclase laths and abundant oxides, but clinopyroxene and occasional olivine may also be present. Rare, heavily resorbed amphibole and spongy-cored, resorbed plagioclase phenocrysts are present in some evolved, trachyandesite monogenetic samples. Cumulophyric clusters of clinopyroxene and plagioclase are common.

Evolved SF Mountain samples are porphyritic, with low crystal contents (up to a few percent). The matrix phases are similar to the monogenetic samples. Common phenocryst minerals include simply-zoned, tabular, rounded plagioclase (which may or may not have spongy cores), heavily resorbed clinopyroxene, and amphibole. Reaction rims on the amphiboles range from barely present to almost complete replacement.

1.4 Data

1.4.1 Major Elements

Major element abundances in samples collected for this study (Figure 1.6) were measured at the GeoAnalytical Lab at Washington State University (D. M. Johnson, Hooper, & Conrey, 1999). The USGS data collection procedures are outlined in E. W. Wolfe, Newhall, and Ulrich (1987).

SiO₂ contents for the whole field range from relatively low (<45 wt%; excluding xenoliths/cumulates) up to rhyolitic and are generally weakly alkaline. Monogenetic samples evolve to trachyandesite (up to ~60 wt% SiO₂), but the median silica content of monogenetic samples (excluding the evolved centers) is ~48 wt% SiO₂. Of the major evolved complexes, most are intermediate to rhyolitic; mean SiO₂ contents of O’Leary Peak, Bill Williams Mountain, and Kendrick Peak are all ~64 wt%. SF Mountain is slightly lower, ~60 wt%, and Sitgreaves Peak is higher, ~74 wt% SiO₂.

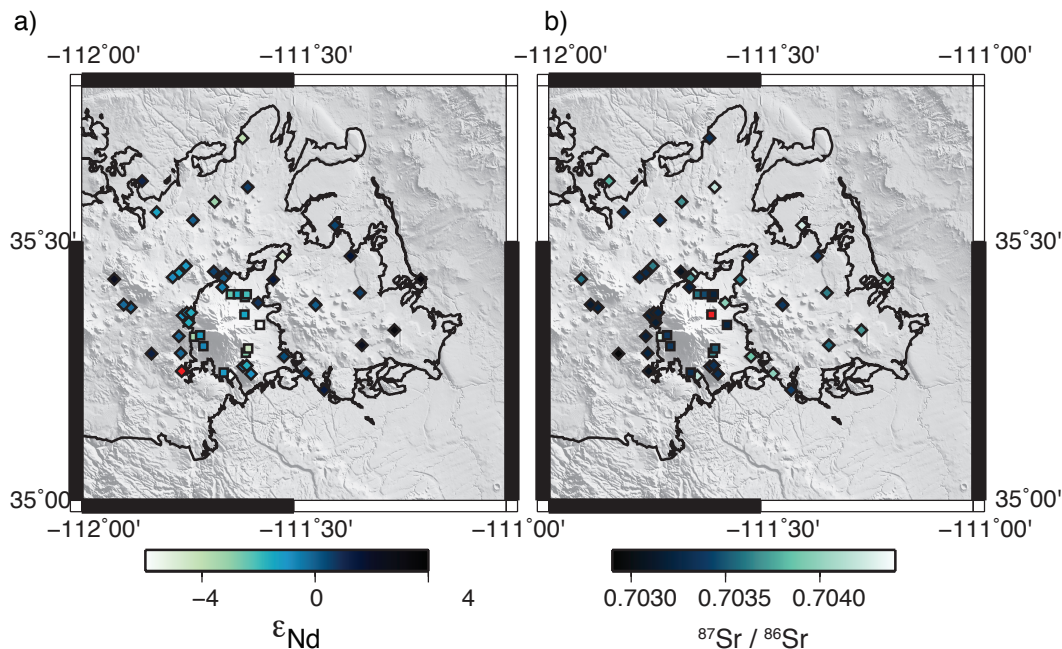


Figure 1.5: Location maps with isotopic data. Field and SF Mountain are outlined in black. Monogenetic samples plotted as diamonds; SF Mountain as squares. Color scheme shows isotopic values: ϵ_{Nd} in (a) and $^{87}Sr/^{86}Sr$ in (b). The two red points mark the samples with outlier isotopic ratios: a trachyandesite in (a) with $\epsilon_{Nd} = -11.0$; and a rhyolite in (b) with $^{87}Sr/^{86}Sr = 0.708296$.

The major element trends of the SFVF magmas are broadly similar to those observed in settings characterized by small degrees of melting under thick lids (many OIB and other intraplate provinces, for instance). Primitive SFVF magmas are SiO_2 -poor, and mafic-to-intermediate magmas show evolution in many elemental concentrations with little change in SiO_2 content. Alkalis are moderately enriched, and reach ~ 4.5 wt% K_2O and ~ 5 wt% Na_2O in the most evolved rocks. Al_2O_3 contents evolve from low to high values (up to 18–19 wt%), while Fe contents (expressed as FeO_T) tend to remain below 12 wt%. The TiO_2 contents of the monogenetic magmas are scattered (similar to many intraplate volcanic systems) and intermediate to OIB and MORB.

1.4.2 Trace Elements

Trace element abundances for samples in this study (Figures 1.7 and 1.8) were measured at the GeoAnalytical Lab at Washington State University. Similar to OIB, SFVF magmas are enriched in trace elements with respect to depleted mantle and/or MORB. SFVF magmas have weakly fractionated HREE, enrichment in LREE and fluid-mobile elements, and lack prominent Nb–Ta depletions generally associated with subduction zones (Figure 1.7c). Excepting the sole rhyolite, these magmas also lack Eu depletions, and only the more evolved

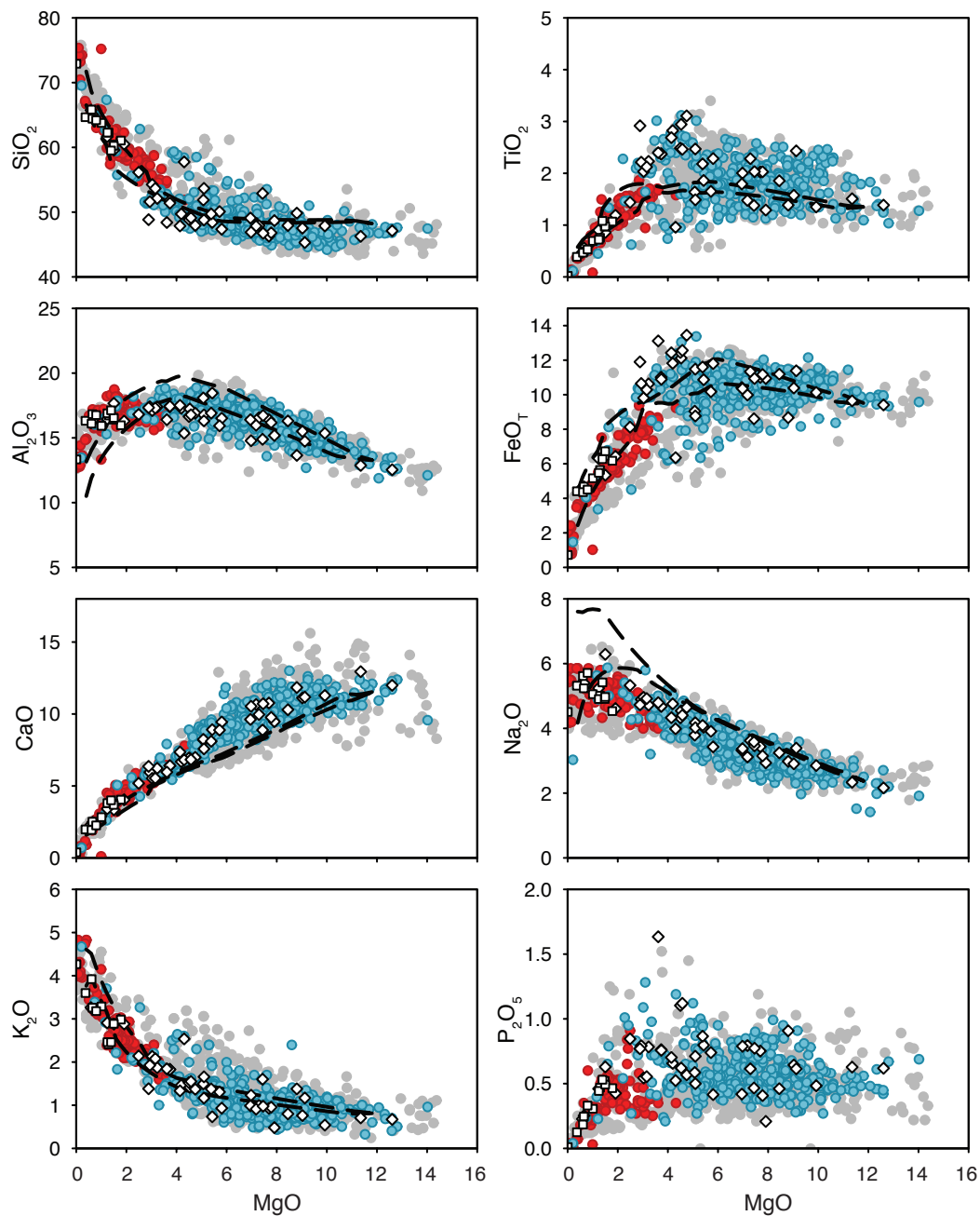


Figure 1.6: Major element covariation diagrams for SFVF magmas. Symbols and colors are as described in Figure 1.4. Dashed black lines delineate the envelope of AFC ensemble model results.

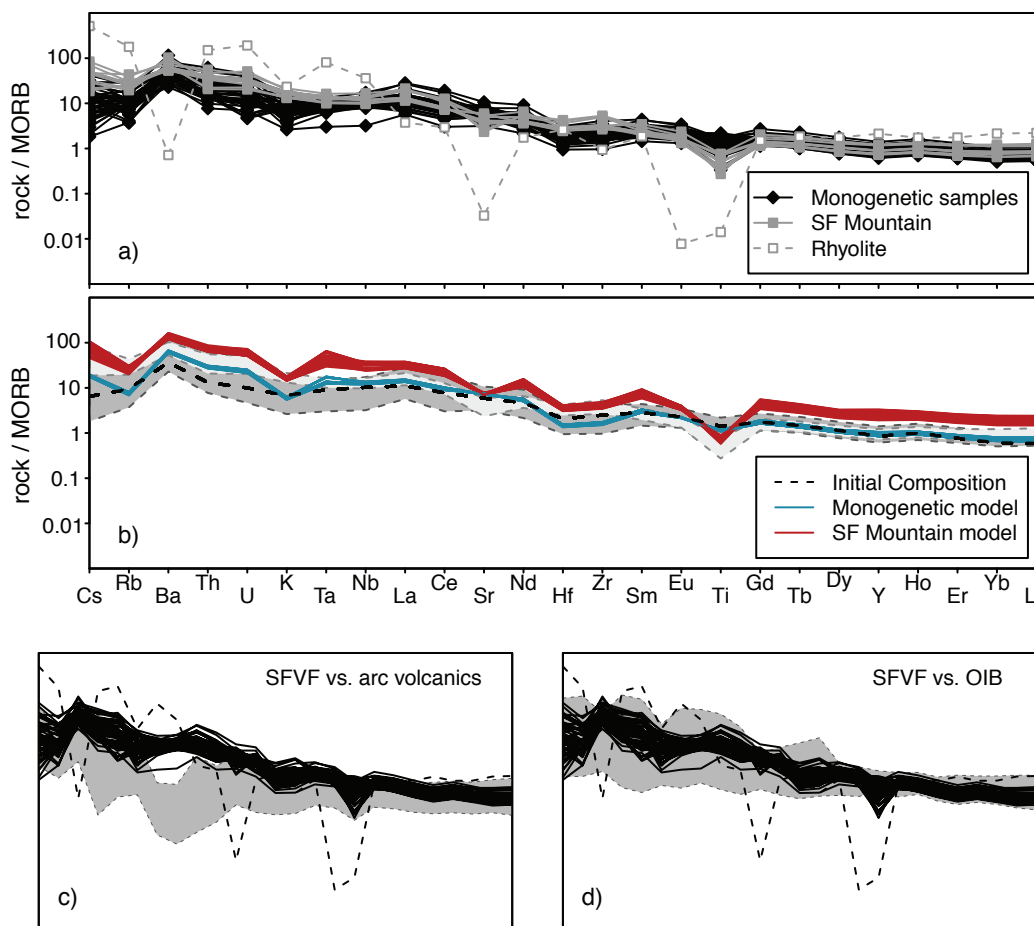


Figure 1.7: Trace element diagrams. (a) trace element spidergram with samples organized into monogenetic and stratovolcano categories; the rhyolite is the dashed line. (b) Similar to (a), but samples are grouped and shown as fields, while colored lines indicate model output: dark grey indicates monogenetic samples; light grey indicates SF Mountain (the rhyolite has been omitted); model parent composition is the dashed black line; modeled monogenetic composition are in blue; modeled SF Mountain compositions in red. Abundances are normalized to the MORB composition of McDonough and Sun (1995). (c) and (d) show data (black lines) from this study compared to fields encompassing arc and OIB volcanics, respectively (arc and OIB data compiled from the PetDB online database, <http://www.earthchem.org/petdb>).

SF Mountain samples show minor Sr depletions. The rhyolite is compositionally distinct, and exhibits patterns commonly associated with crustal melts, including depleted Ba, Sr, Eu, and Ti. While this sample is enriched in HREE with respect to the remainder of the field, it also has the most depleted LREE. Aside from the rhyolite, there is otherwise a good overlap in the data from SF Mountain flows and the flows from the monogenetic centers.

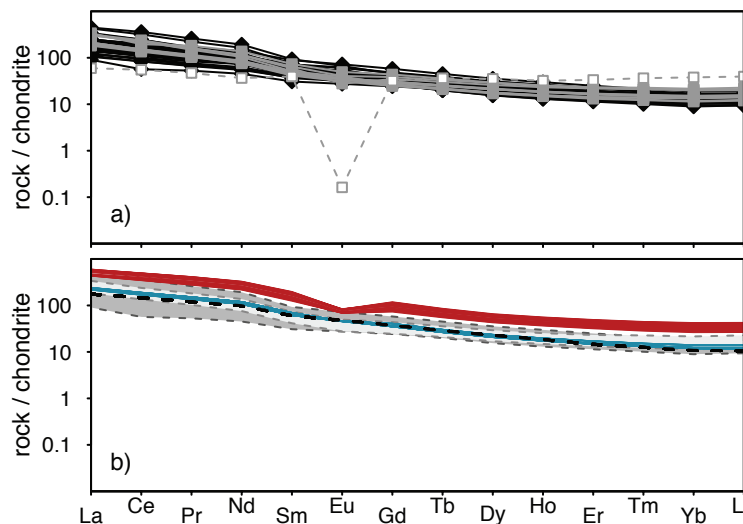


Figure 1.8: Rare Earth Element diagrams. (a) REE from samples normalized to chondritic values of Sun and McDonough (1989). (b) Comparison with model REE output; colors as in Figure 1.7.

1.4.3 Isotopes

Sample preparation and measurement of Sr, Nd, and Pb isotopes was carried out at the Center for Isotope Geochemistry at the University of California, Berkeley. Sr and Nd isotopes were measured for all 56 SFVF samples; 30 were chosen for Pb isotopic analysis. Samples were cut and chipped to ~ 1 cm size and hand-picked to remove weathered or sawed surfaces. Rinsed chips were powdered using an alumina-silicate shatterbox (double-cleaned between samples using sand and pre-contaminant). Powder splits for Pb analyses were subsequently leached in warmed 1 N HCl for 60 min prior to dissolution. No leaching was performed for Sr and Nd analyses except for one sample (12PSF-59), which exhibited vesicle-filling secondary carbonate; this sample was leached for 24 hr in room-temperature 1 N Acetic acid and the leachate was removed by sequential triplicate centrifugation. Samples were sub-boiling digested in $\text{HF} + \text{HNO}_3 + \text{HClO}_4$ in Savillex. Sr was separated using cation-specific Eichrom Sr-Spec resin. Nd was separated during a period of procedure transition, and was recovered both using LN-Spec resin and methylactic acid chemistry. Pb was separated using two stages of AG-1 anion exchange resin chemistry. HNO_3 acids were mixed from double-distilled trace grade stock; the HF, HClO_4 , and acetic acid used were SEASTAR™ BASELINE® grade.

Sr isotopic analyses followed procedures of DePaolo and Daley (2000), but were performed on a Thermo Scientific TRITON TIMS multicollector; Sr isotope ratios were normalized to $^{88}\text{Sr}/^{86}\text{Sr} = 0.1194$. Nd was measured as a metal on the same machine and Nd isotopes were normalized to $^{146}\text{Nd}/^{144}\text{Nd} = 0.7219$. Ce, Sm, and Pr interferences were monitored; Nd separation using LN-Spec resin resulted in higher $^{140}\text{Ce}/^{144}\text{Nd}$ ratios, but still low enough that corrections were negligible. ϵ_{Nd} are reported with respect to $^{143}\text{Nd}/^{144}\text{Nd}_{\text{CHUR},(0)} =$

0.512638. Pb analyses were carried out on a MicroMass Isoprobe MC-ICP-MS with an Airidus II (dry plasma) sample introduction system using a Tl spike to correct for mass fractionation.

For Nd isotopes, ε_{Nd} ranges from +3.4 to -6.0 for most of the samples, excepting a monogenetic trachyandesite with $\varepsilon_{Nd} = -10.97$. The majority of samples cluster fairly close to ε_{Nd} of 0. There is a weak spatial pattern in the ε_{Nd} data: monogenetic magmas tend to have higher ε_{Nd} , while SF Mountain has lower ε_{Nd} (Figure 1.5a). The Sr isotopes for all of the SFVF flows are distinctly unradiogenic, and range from $^{87}\text{Sr}/^{86}\text{Sr} = 0.7029$ to 0.7043 (the rhyolite has an anomalously high $^{87}\text{Sr}/^{86}\text{Sr} = 0.708296$). Magmas from SF Mountain and the monogenetic volcanics overlap in their $^{87}\text{Sr}/^{86}\text{Sr}$ ranges, and spatial trends are less readily apparent within the Sr data set (Figure 1.5b). A number of samples have both unradiogenic Sr and Nd. This is apparent in a plot of ε_{Nd} vs. $^{87}\text{Sr}/^{86}\text{Sr}$ (Figure 1.9a), where the SFVF data are almost orthogonal to the “normal” OIB/MORB mantle array. Pb isotopes plot above the Northern Hemisphere Reference Line (NHRL) of S. R. Hart (1984) (Figures 1.9e, g), similar to many OIB (cf. Zindler & S. R. Hart, 1986), but SFVF magmas also extend to uncharacteristically unradiogenic Pb isotope ratios: $^{206}\text{Pb}/^{204}\text{Pb}$ from 17.4 to 18.7; $^{207}\text{Pb}/^{204}\text{Pb}$ from 15.4 to 15.6; $^{208}\text{Pb}/^{204}\text{Pb}$ from 36.9 to 38.5).

In terms of Pb and Nd isotopes, differentiated samples (both SF Mountain and monogenetic trachyandesites and trachytes) are more unradiogenic (lower ε_{Nd} and $^{206}\text{Pb}/^{204}\text{Pb}$) than primitive monogenetic basalts and trachybasalts (Figure 1.10); this is especially apparent in the Pb system, where the SF Mountain magmas are among the most unradiogenic samples in the suite. The $^{87}\text{Sr}/^{86}\text{Sr}$ data exhibit a similar trend; lower $^{87}\text{Sr}/^{86}\text{Sr}$ with increasing SiO_2 , but the most silicic, evolved samples also show the highest $^{87}\text{Sr}/^{86}\text{Sr}$ ratios.

1.5 Magma evolution by assimilation / fractional crystallization

The co-variation between differentiation and isotopic evolution toward unradiogenic compositions suggests SFVF magmas undergo assimilation/fractional crystallization (AFC) and incorporate isotopically distinct, unradiogenic rock material in the assimilation process. There is ample evidence suggesting this assimilation occurs in the deep crust:

1. Deep crustal xenoliths, including granulites, are ubiquitous in SFVF magmas. In particular, the mafic and intermediate granulites extend to unradiogenic isotopic compositions ($^{87}\text{Sr}/^{86}\text{Sr}$ as low as 0.7030) and have Rb/Sr and U/Pb ratios that are an order of magnitude less than depleted mantle (W. Chen & Arculus, 1995). Similar unradiogenic granulite xenoliths are found in Tertiary diatremes and minettes in the interior of the Colorado Plateau (Wendlandt, DePaolo, & Baldrige, 1993), suggesting the deep crust of the plateau may be largely composed of unradiogenic material.

2. Mineralogical studies on Colorado Plateau xenoliths suggest that they have been stored in relatively cold crust, at 15–25 km and $<450^{\circ}$ C (Wendlandt, Depaolo, & Baldrige, 1996). This depth range overlaps with that of a seismic low-velocity region beneath the SFVF, inferred as a zone of deep magma infiltration (Stauber, 1982; Durrani et al., 1999).
3. Petrochemical evidence supports deep fractionation: the evolution to high Al_2O_3 and the lack of Eu, Sr, and Ba depletions all suggest significant fractionation at depths below plagioclase stability. The presence of pyroxenite cumulate xenoliths, thought to be genetically related to SFVF magmas (W. Chen & Arculus, 1995), also suggests significant deep fractionation below plagioclase and olivine stability.

Alternatively, the isotopic arrays in Figure 1.9 could be explained by melting mixtures of OIB-like asthenosphere and unradiogenic, eclogite-rich sub-continental lithospheric mantle. Eclogite melting at mantle conditions has been shown to produce evolved, higher- SiO_2 melts (Pertermann, 2003; Spandler, Yaxley, Green, and Rosenthal, 2007), but it also results in high TiO_2 and fractionated HREE. If evolved liquids were generated by preferential eclogite melting rather than AFC, one would expect the SF Mountain magmas to have trace element characteristics substantially different from the primitive monogenetic samples (e.g. fractionated HREE). This is not observed; both SF Mountain and monogenetic magmas have very similar, nearly overlapping trace element patterns (Figures 1.7 and 1.8). Additionally, eclogite xenoliths are not found in SFVF magmas, and those present in interior Colorado Plateau volcanics are too radiogenic to be suitable end-members ($^{87}\text{Sr}/^{86}\text{Sr} = 0.7066\text{--}0.7089$; Wendlandt, DePaolo, and Baldrige, 1993). Thus it is unlikely that the isotopic trends in Figures 1.9 and 1.10 are produced by different mantle sources (I discuss the potential role of pyroxenite in the SFVF source in detail in section section 1.6.1).

In addition to deep AFC, the high $^{87}\text{Sr}/^{86}\text{Sr}$ of the most evolved samples (see trends in Figure 1.10c, d) suggests that additional assimilation of high- $^{87}\text{Sr}/^{86}\text{Sr}$ material occurs in the magmatic system during the production of higher- SiO_2 liquids, probably in the upper crust. Evidence for shallow, upper crust assimilation is supported by the presence of upper crust xenoliths in SFVF magmas. No isotopic analyses of SFVF silicic xenoliths have yet been performed, but similar interior Colorado Plateau xenoliths (paragneisses and metagranites) have very high values of $^{87}\text{Sr}/^{86}\text{Sr} = 0.72\text{--}0.81$ (Wendlandt, DePaolo, & Baldrige, 1993). Assimilation of upper crust lithologies is not necessarily easily traceable; although they have high $^{87}\text{Sr}/^{86}\text{Sr}$, they also have low Sr contents in comparison to most SFVF magmas, which mutes the isotopic shifts due to assimilation. Only the most evolved magmas show evidence of this second, shallow assimilation process, either because they have resided for sufficient time in the shallow crust, or because they have evolved to sufficiently low Sr concentrations to be susceptible to contamination.

1.5.1 AFC modeling with alphaMELTS

To evaluate the details of the evolution of SFVF magmas by AFC and to quantitatively constrain mantle processes such as magmatic flux, I model the chemical evolution of the SFVF lavas numerically using the alphaMELTS software package. alphaMELTS is a scriptable, command-line executable interface that extends the functionality of the MELTS, pMELTS, and phMELTS thermodynamic calculation subroutines (Ghiorso & Sack, 1995; Asimow & Ghiorso, 1998; Ghiorso, Hirschmann, Reiners, & Kress, 2002). Technical information on alphaMELTS can be found in D. Smith and Griffin (2005); the appendix of Thompson et al. (2007); Antoshechkina and Asimow (2010), Antoshechkina, Asimow, Hauri, and Luffi (2010); on the website <http://magmasource.caltech.edu/alphamelts/> and in Appendix A. I chose to use alphaMELTS for AFC modeling for several reasons:

1. Isotopic compositions of SFVF assimilants have either never been measured (as with Pb) or are variable and ambiguous (as with Nd, where assimilants show a wide range in ε_{Nd} , and deep and shallow assimilants have overlapping compositions). This makes AFC models based solely on isotope ratios and trace element abundances (which depend on well-constrained end-members; e.g. DePaolo, 1981; Spera and Bohron, 2004) limited in their utility. alphaMELTS can model major elements, trace elements, and isotopes; this is advantageous because AFC can be constrained with robust data (major elements trends, Sr isotopes), while unknowns (such as the Pb isotopic composition of the deep assimilant) can be inferred. Additionally, modeling with alphaMELTS allows the use of the extensive USGS major element database.
2. As SFVF magmas evolve, their fractionating assemblages also change. While previous models have accounted for this by relatively coarse parameterization (e.g. Hammerley & DePaolo, 2006), alphaMELTS thermodynamically computes the fractionating assemblage and bulk partition coefficients at each model iteration.
3. alphaMELTS can be run in isenthalpic mode, which applies a conservation of energy balance to the AFC process. This constraint, combined with the thermodynamic computation of fractionating phases, allows me to quantify amounts of assimilation and crystallization, and produce estimates for mantle magma fluxes into the base of the volcanic system.
4. alphaMELTS is batch-executable and can be run from scripts. This allows for construction of model ensembles to explore how AFC processes operate over a range of pressures, crust geotherms, and degrees of assimilant partial melting.

I include a short overview of my approach below. Additional technical information is detailed in Appendix A.

Conceptually, I treat SFVF magmatic evolution as a two-stage process. Primitive magma undergoes a phase 1 deep AFC process at 0.40–0.55 GPa (15–20 km). The liquid undergoes

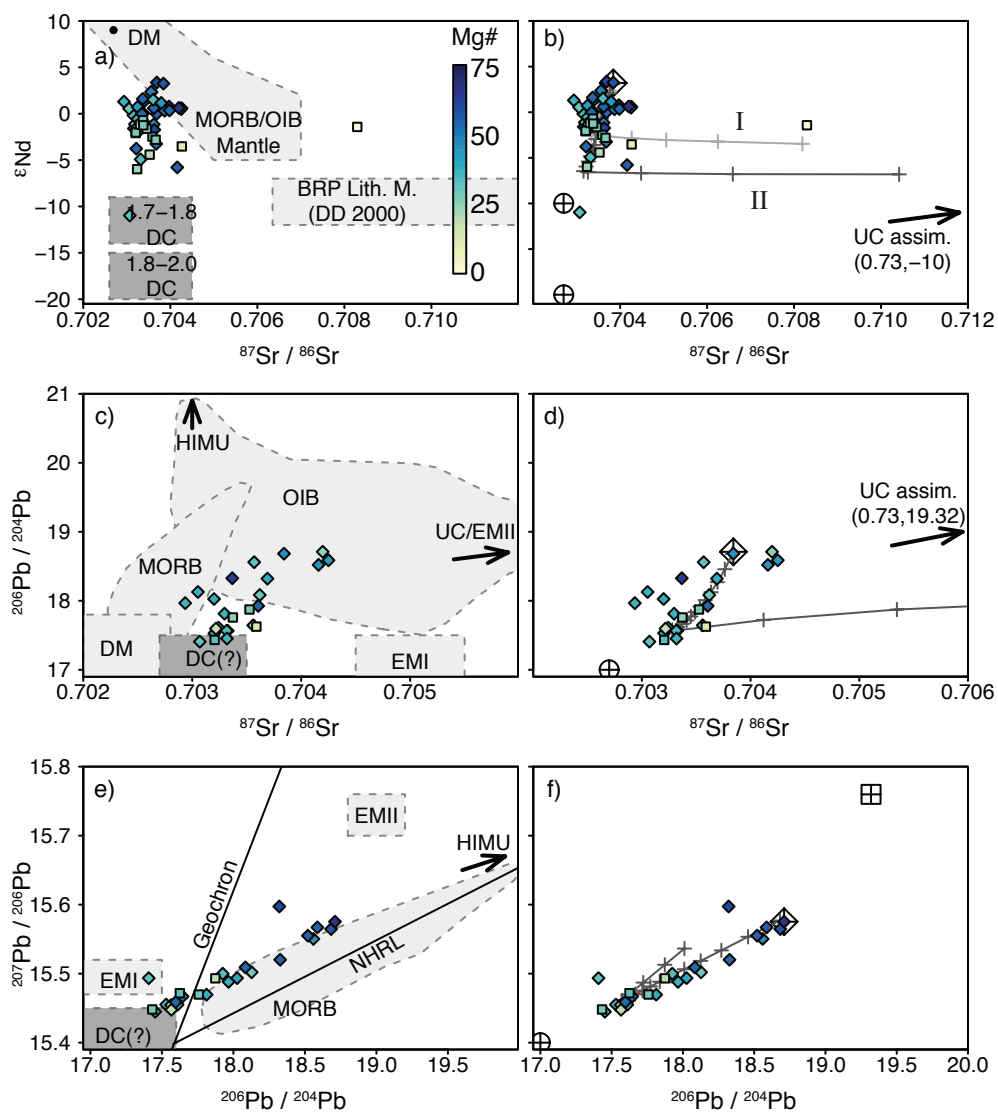
isobaric, isenthalpic AFC until it reaches sufficiently evolved Mg# and low $^{87}\text{Sr}/^{86}\text{Sr}$. Subsequently, the liquid is decompressed isentropically to 0.13 GPa (5 km), where phase 2 AFC takes place. I systematically vary input parameters and run a selection of models to produce an ensemble of results.

My two-stage AFC model is a simplification of what is almost certainly a continuous, stochastic process experienced to different degrees by individual magma batches. For instance, some SFVF magmas contain dense ultramafic xenoliths and must have ascended rapidly. Some of these xenoliths are pyroxenite cumulates, formed by magmatic fractionation in the deep crust (W. Chen & Arculus, 1995), requiring that other magma batches slowed or stalled. Although I model deep AFC, a deep, persistent, well-stirred magma chamber is not necessarily present. Similarly, although storage and fractionation occurs in the shallow crust beneath SF Mountain (Wenrich-Verbeek, 1979), this system may have been only semi-persistent (similar to Mount Taylor; cf. Perry, Baldrige, DePaolo, and Shafiqullah, 1990).

The parent magma and assimilant compositions used in the model are presented in tables 1.3 and 1.4. AFC modeling with alphaMELTS requires fixed assimilant compositions, which I assume are partial melts of two crustal lithologies: mafic granulite (for phase 1); and mean upper crust (phase 2). I compute the partial melt compositions using alphaMELTS in batch mode for several different degrees of melting. Because the mafic granulite is refractory, and has a calculated liquidus temperature comparable to that of the intruding magma, it likely melts less ($F = 0.2\text{--}0.6$), while the more silicic upper crustal lithology melts more ($F = 0.6\text{--}1.0$).

MELTS-based calculations, including those performed by alphaMELTS, track FeO and Fe_2O_3 , both of which are reported in the USGS data and in the granulite xenolith data. Rather than re-compute the Fe speciation, compositions are based on actual data, when both Fe_2O_3 and FeO are reported. The resulting $\text{Fe}_2\text{O}_3 / \text{FeO}$ of the parent magma is somewhat oxidized with respect to most mantle-derived magmas (cf. E. W. Wolfe, Newhall, & Ulrich, 1987). For the upper crust assimilant (where only FeO_T is reported by Rudnick and Gao, 2003), Fe speciation is calculated at 0.13 GPa by alphaMELTS assuming QFM buffer. During the model calculations, oxygen fugacity is unconstrained (this is a limitation in the alphaMELTS implementation of isenthalpic assimilation).

USGS-reported H_2O contents in SFVF magmas vary from 0 to 1.7 wt%, but may not be representative of initial H_2O contents due to degassing and shallow interaction with the water table (e.g. Valentine, 2012). However, primitive SFVF magmas were likely hydrated and/or carbonated (discussed in greater detail in section 1.6.1). For the parent magma composition, water contents are derived from actual data. In many cases, trace amounts of water are required to stabilize the alphaMELTS calculations; I assign the mafic granulite lithology an initial water content of 0.01 wt% and the upper crust 1.0 wt%. Because partial melts of these compositions are used in the model, actual water contents in the assimilated material is variable.



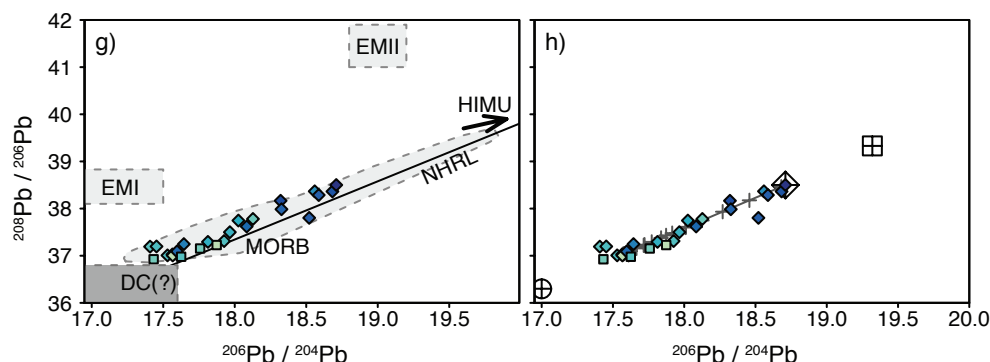


Figure 1.9: Isotopic data for SFVF magmas. Diamonds are monogenetic samples, squares are SF Mountain. Color scheme shows sample Mg#. Plots in the left column show the data with respect to mantle sources and potential contaminants. Plots in the right column compare this same data with a representative AFC model run (solid line). Ticks on the model lines denote every tenth iteration. Only one line out of the ensemble is shown for clarity (more information about the ensemble modeling process and the ranges over which I vary the parameters is provided in Appendix A). Initial isotope compositions of the parent magma in the model are indicated with crossed diamonds, phase 1 assimilant with crossed circles, phase 2 assimilants with crossed squares. BRP Lith. M. refers to the inferred Basin and Range subcontinental lithospheric mantle of DePaolo and Daley (2000). DM = depleted mantle of Salters and Stracke (2004). DC boxes are isotopic compositions of phase 1 assimilant. Also plotted are MORB and OIB fields, mantle source end-members from Zindler and S. R. Hart (1986), and NHRL of S. R. Hart (1984). I and II label output from different assimilant composition models; see main text for additional details.

1.5.2 AFC model output: major elements

Model output is shown in comparison with major element data in Figure 1.6 (and in Appendix A). Although SFVF magmas range in composition from primitive basalt to rhyolite, the majority have mafic to intermediate compositions, and are largely explained by the deeper, phase 1 AFC process. At 0.40–0.55 GPa, clinopyroxene plus lesser orthopyroxene and spinel are fractionated by the model, while plagioclase and olivine are initially suppressed (Figure 1.11). The model clinopyroxene has roughly the same SiO_2 content as the liquid from which it crystallizes, resulting in little change in liquid SiO_2 as crystallization progresses. Plagioclase suppression causes the liquid Al_2O_3 concentration to increase with progressive crystallization, and the fractionating assemblage computed by the phase 1 model compares favorably with the petrography of the monogenetic samples; most lack phenocrystic plagioclase and none contain phenocrystic olivine.

There is greater misfit between the model and the data at evolved compositions. This is especially apparent in the overestimated Na_2O contents, but also in the Al_2O_3 trend (Figure 1.6). The misfit could be due to the lack of amphibole fractionation in the model (into which both Na_2O and Al_2O_3 partition). Trachytes and the more evolved trachyandesites have amphibole phenocrysts, but the model fails to crystallize any until the liquid reaches

rhyolitic compositions (Figure 1.11). Presumably the failure of the model to crystallize amphibole is a function of the magmatic water contents used in the modeling, which are difficult to estimate accurately.

1.5.3 AFC model output: trace elements

Modeled trace elements and REE are compared with data in Figures 1.7b and 1.8b. Trace element abundances are output for each iteration in a model run, but the complete output for all iterations is not shown. Model output is shown for two different extents of AFC progress: one where the model has evolved to a major element composition similar to the monogenetic lavas; and one where the model composition is comparable to those of the SF Mountain samples (the method of constraining the extent of AFC is discussed in greater detail in section 1.6 below).

Trace elements are little enriched in SFVF magmas as evolution proceeds. Modeling successfully reproduces this behavior when compositions are mafic, but the simulations result in excess trace element enrichments in evolved magmas. In all models, the liquid eventually reaches plagioclase saturation, resulting in modest Eu depletions that are absent in SFVF samples (Figure 1.8b). Given the major and trace element data, and petrographic evidence, it is likely that amphibole fractionates and plagioclase is suppressed at intermediate compositions, whereas the model crystallizes plagioclase well before amphibole. Plagioclase stability is inhibited by pressure, but may also be suppressed by H₂O (e.g Gaetani, Grove, & Bryan, 1993), and as noted above, the model compositions may have water contents that are somewhat too low.

1.5.4 AFC modeling: isotopes

Candidate SFVF assimilants have isotopic compositions that are known reasonably well (Sr), variable (Nd, Hf) or poorly characterized (Pb). For modeling purposes, both a primitive basaltic magma composition (and associated isotopic ratios), and various crustal lithologies that can be partially melted and the liquid assimilated into the primitive magma (each with associated isotopic ratios) are required. I base the primitive magma composition, both chemical and isotopic, on the data, because the basalt compositions as measured are not far from primitive, but I specify the assimilant compositions, especially the isotopic ratios, such that the model best fits the trends shown in Figures 1.9 and 1.10. In this way it is possible to assess which lithologies are the most likely assimilants, which allows for comparison of the various samples of crustal rocks that are available and the rocks that were most heavily involved in the SFVF magmatic evolution.

Xenoliths of crustal rocks from almost all levels of the continental crust of the Colorado Plateau and neighboring areas are available from diatremes and other volcanic features erupted since the mid-Cenozoic. Colorado Plateau mafic granulite xenoliths from the Four Corners area and from the SFVF have ϵ_{Nd} that varies over a wide range from +7.0 to -16.8, and some intermediate-to-felsic granulites reach as low as -23.5 (W. Chen & Arculus,

1995; Wendlandt, DePaolo, & Baldrige, 1993). The variability in ε_{Nd} expected in the crust beneath the SFVF is the result of variation in lithology from mafic granulite and amphibolite to silica-rich granitic gneiss and schist, and partly also because the SFVF straddles two ancient lithotectonic blocks of differing ages (Bennett & DePaolo, 1987). The difference in age results in different isotopic compositions due to the difference in the amount of time available for radioactive decay since the crust was formed (denoted by dark gray DC boxes in Figure 1.9a). For the phase 1 AFC process, I model the effects of two different Nd isotopic compositions representing a range in lithology likely to be present in the lower-to-middle crust beneath the SFVF: $\varepsilon_{Nd, \text{MaficGranulite}} = -10.0$ (model I in Figure 1.9b, 1.10a, and 1.10b); and $\varepsilon_{Nd, \text{MaficGranulite}} = -20.0$ (model II). For the upper crust, I assign $\varepsilon_{Nd} = -10.0$ (the proposed limit of the shallow crust from Farmer and DePaolo, 1983).

The Sr isotopes in Colorado Plateau crustal lithologies cover a wide range, but are distinct to specific rock-types. Mafic granulite xenoliths have the most unradiogenic Sr, from $^{87}\text{Sr}/^{86}\text{Sr}$ of 0.705 down to 0.703; intermediate and felsic granulites overlap but extend to higher values (up to 0.715; Wendlandt, DePaolo, and Baldrige, 1993; W. Chen and Arculus, 1995). Mid-crustal garnet amphibolites have major element and isotopic compositions similar to those of the granulites ($^{87}\text{Sr}/^{86}\text{Sr} = 0.704\text{--}0.715$), and may be related. Eclogite xenoliths have not been reported in SFVF magmas, but are present in interior Colorado Plateau diatremes and minettes; these eclogites have Sr isotopic compositions ratios that are more radiogenic than SFVF magmas ($^{87}\text{Sr}/^{86}\text{Sr} = 0.707\text{--}0.708$). Felsic lithologies tend to be the most radiogenic; granites from throughout the United States southwest have $^{87}\text{Sr}/^{86}\text{Sr} = 0.705\text{--}0.720$ while ancient supracrustal meta-lithologies, including gneisses, may reach up to $^{87}\text{Sr}/^{86}\text{Sr} = 0.817$ (Wendlandt, DePaolo, & Baldrige, 1993; Farmer & DePaolo, 1983).

The required assimilant $^{87}\text{Sr}/^{86}\text{Sr}$ the phase 1 AFC model is not represented by available samples of granulite xenoliths from the SFVF field; most have $^{87}\text{Sr}/^{86}\text{Sr}$ that is too high. Even the SFVF granulite sample with the lowest reported $^{87}\text{Sr}/^{86}\text{Sr} = 0.70297$ fails to generate the negative trend versus MgO. This failure may be only partly due to the $^{87}\text{Sr}/^{86}\text{Sr}$ value; the model magmas evolve to high Sr abundances during the AFC process because there is no plagioclase fractionation (as an example real lava composition, the monogenetic trachyandesite 03HSF-1 has 1385 ppm Sr). Also, partial melts of granulite have even lower Sr concentration than the bulk granulite sample due to the presence of residual plagioclase (compare F=0.2 granulite melt vs. its parent in table 1.3). I have specified $^{87}\text{Sr}/^{86}\text{Sr} = 0.7027$ for the phase 1 assimilant, which is a very low value equivalent to “depleted mantle” of Salters and Stracke (2004). The phase 2 assimilant, on the other hand, could have high and variable $^{87}\text{Sr}/^{86}\text{Sr}$, based on the xenolith samples available. Sr concentrations may be variable as well. To explore the effect of varying Sr concentration in the assimilant, I ran ensembles with different phase 2 assimilants: output III in Figures 1.10c and 1.10d shows results assuming 320 ppm Sr (mean upper crust of Rudnick and Gao, 2003) and $^{87}\text{Sr}/^{86}\text{Sr} = 0.73$; output IV shows results assuming 65 ppm Sr (the lowest abundance in local Proterozoic granites of Bryant, Wooden, and Nealey, 2001) and $^{87}\text{Sr}/^{86}\text{Sr} = 0.79$.

There are fewer constraints on the Pb isotopic composition of the deep crust in the SFVF area, since Pb isotopes of the local xenoliths have not been measured. However, based on

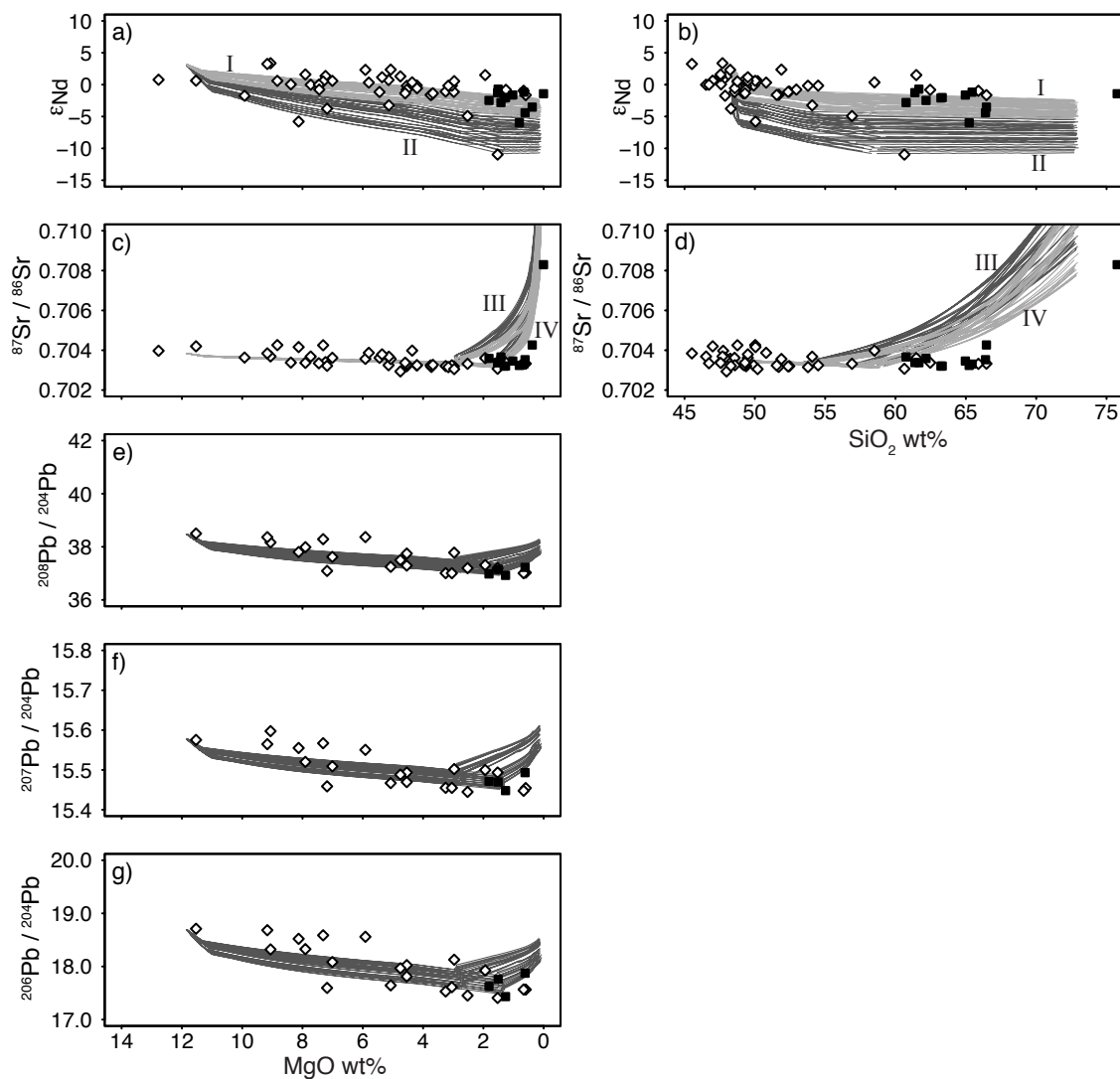


Figure 1.10: SFVF Isotopic covariation with magmatic evolution. Closed squares are SF Mountain samples, open diamonds are monogenetic, surrounding samples. Each line is output from a single AFC model run in the ensemble (similar to the lines shown in Figure 1.9, except rather than a single representative run, all model output is shown in this figure – the 10th iteration ticks have been omitted for clarity). Different groups labeled I, II, III, and IV illustrate the effects of choosing different compositions for the assimilants; see main text for details. Plots in the left column show isotopic results against MgO wt% content as an indicator of differentiation; plots in the right are against SiO₂ wt%.

the relatively extreme nature of the Sr isotope trend, it could be inferred that the assimilants must be depleted in U, as that is another of the hallmarks of granulite facies rocks. Rather than basing the model assimilant Pb isotopic compositions on xenolith data, I have selected values that sufficiently reproduce the trends observed in Figures 1.9 and 1.10. The Pb isotope ratios that work well in the model for the phase 1 assimilant are $^{206}\text{Pb}/^{204}\text{Pb} = 17.0$; $^{207}\text{Pb}/^{204}\text{Pb} = 15.4$; $^{208}\text{Pb}/^{204}\text{Pb} = 36.3$. For the phase 2 assimilant, I assign mean upper crust Pb isotope compositions of Asmerom and Jacobsen (1993), although there are few enough felsic samples that the shallow process is largely unconstrained.

The Sr, Nd, and Pb isotopic data are plotted versus MgO concentrations in Figure 1.10, where decreasing MgO corresponds to increasing magma compositional evolution during the inferred AFC process. The Sr data follow a straightforward evolutionary trend of slowly decreasing $^{87}\text{Sr}/^{86}\text{Sr}$ with decreasing MgO, followed by rapidly increasing $^{87}\text{Sr}/^{86}\text{Sr}$ at very low MgO (Figures 1.10a). The Phase 1 part of this trend departs markedly from the usual or expected behavior; in most cases assimilation of crustal rocks results in increasing $^{87}\text{Sr}/^{86}\text{Sr}$ because almost all crustal lithologies have higher $^{87}\text{Sr}/^{86}\text{Sr}$ than the mantle rocks from which basalts are typically derived (Perry, Baldrige, & DePaolo, 1987; Perry, Baldrige, DePaolo, & Shafiqullah, 1990; Hildreth, Halliday, & Christiansen, 1991; Yogodzinski, Naumann, Smith, Bradshaw, & Walker, 1996; Cousens, 1996; Hammersley & DePaolo, 2006). The $^{87}\text{Sr}/^{86}\text{Sr}$ versus MgO trend of the SFVF lavas is a distinguishing characteristic and one that is diagnostic; the assimilant must be composed of granulite facies crustal rocks that are depleted in Rb.

The most primitive (highest MgO) basalts from the SFVF have ϵ_{Nd} of ~ 0 to $+4$, values that generally are lower than those found in oceanic basalts, but relatively common in continental basalts. Most crustal lithologies have lower values, as discussed above (-10 to -20 in the SFVF region). Consequently, for the AFC process, decreasing ϵ_{Nd} with decreasing MgO are expected (and observed; Figure 1.10c). The overall shift in ϵ_{Nd} from the most primitive to the high silica lavas is about 5 units; most of the difference is between the lavas with $\text{SiO}_2 < 50\%$ and those with $\text{SiO}_2 > 52\%$ (Figure 1.10d). This pattern for AFC processes in volcanic systems is common and suggests that most of the assimilation occurs in the transition between basalt and basaltic andesite (or basaltic trachyandesite), probably at relatively high temperatures deep in the crust. The remainder of the magmatic evolution is predominantly fractional crystallization in shallower, small magma chambers (Perry, Baldrige, DePaolo, & Shafiqullah, 1990; Perry, Depaolo, & Baldrige, 1993; Hammersley & DePaolo, 2006).

The Pb isotopic trends in Figures 1.9c-h and 1.10e-g suggest SFVF magmas evolve toward low $^{206}\text{Pb}/^{204}\text{Pb}$ and $^{207}\text{Pb}/^{204}\text{Pb}$ as would be expected in old, U-depleted rocks. There is also a trend toward lower $^{208}\text{Pb}/^{204}\text{Pb}$, which is not necessarily to be expected as a result of granulite facies metamorphism, but is probably a reflection of the relatively high $^{208}\text{Pb}/^{204}\text{Pb}$ of most mantle-derived lavas.

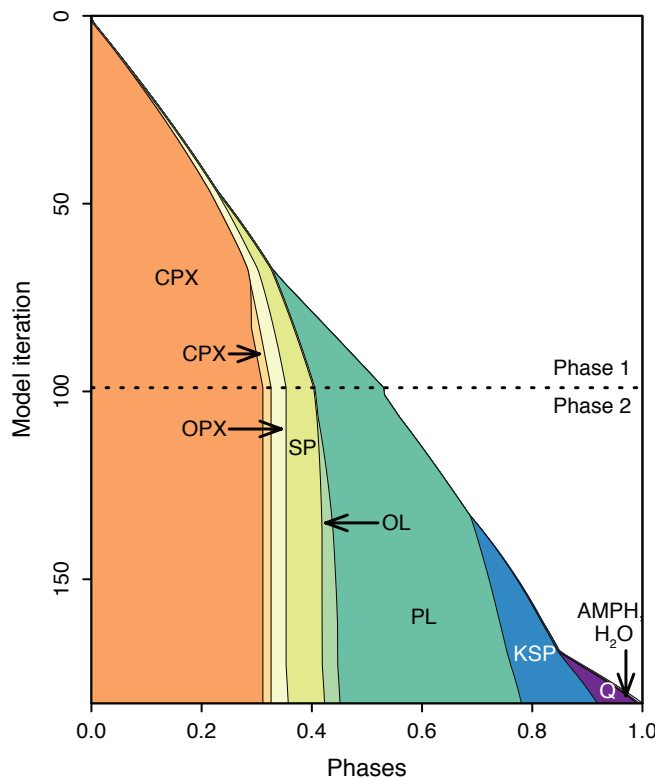


Figure 1.11: Example output of a single alphaMELTS 2-stage AFC model run (for phase 1 pressure of 0.55 GPa) showing cumulative phases fractionated. Phase masses are shown as fractions of the total. CPX = clinopyroxene, OPX = orthopyroxene, SP = spinel, OL = olivine, PL = plagioclase, KSP = alkali feldspar, Q = quartz, AMPH = amphibole. Dotted line delineates phase 1 AFC from phase 2.

1.5.5 AFC summary

Major and trace element trends in both the SF Mountain and monogenetic magmas can be mostly explained by deep AFC, where clinopyroxene fractionates and olivine and plagioclase are suppressed. Almost all samples show isotopic evidence of contamination by an unradiogenic (in terms of Sr, Nd, and Pb) assimilant. The models successfully reproduce the data using phase 1 assimilant Sr and Pb compositions that correspond to Rb- and U-depleted granulite facies lower crustal lithologies. For Nd, more normal crustal isotopic compositions are required, with ϵ_{Nd} from -10.0 to -20.0 as would be expected for typical 2 billion year old crustal rocks from this region (Bennett & DePaolo, 1987; DePaolo, Linn, & Schubert, 1991). The Sr and Nd isotopic compositions of the highest silica SFVF magmas require additional late-stage assimilation of material with high $^{87}\text{Sr}/^{86}\text{Sr}$ and low ϵ_{Nd} , but do not require a chemically distinct source lithology. This radiogenic material is likely derived from the upper crust. The SFVF data are fit by a Phase 2 assimilant with 320 ppm Sr, $^{87}\text{Sr}/^{86}\text{Sr} = 0.73$, or 65 ppm Sr, $^{87}\text{Sr}/^{86}\text{Sr} = 0.79$, and $\epsilon_{Nd} = -10.0$, values that should be fairly common

in upper crustal rocks of the region.

I note that the model best fits the data in the mafic to intermediate range. At felsic compositions, there is increasing misfit, possibly because the model overestimates plagioclase stability, and fails to produce amphibole until rhyolitic compositions. Despite these failings, alphaMELTS appears to be a useful tool for modeling magmatic evolution by AFC.

1.5.6 A comment on the ε_{Hf} nature of some SFVF magmas

As noted by Beard and C. M. Johnson (1997), Reid et al. (2012), some volcanic rocks from the southwestern United States (the SFVF included) have anomalously high ε_{Hf} values (they plot above the terrestrial $\varepsilon_{Nd-\varepsilon_{Hf}}$ array, denoted with positive $\Delta\varepsilon_{Hf}$; cf. Beard and C. M. Johnson, 1997). While this could be due to pelagic clays and muds that were recycled into the mantle at some time in the geologic past (Vervoort, Patchett, Blichert-Toft, & Albarede, 1999), Reid et al. (2012) point out that Colorado Plateau samples characterized as sediment-influenced in terms of their Hf isotopes also have low $^{206}\text{Pb}/^{204}\text{Pb} < 18.5$, opposite what would be expected from a source contaminated by old radiogenic sediments.

In the SFVF, the most primitive magmas have $^{206}\text{Pb}/^{204}\text{Pb}$ of ~ 18.7 , similar to oceanic basalts. The lower values in the more evolved SFVF samples (down to ~ 17.5) are probably due to assimilation. Correlated high ε_{Hf} and low $^{206}\text{Pb}/^{204}\text{Pb}$ is not necessarily expected, but clearly implies that the assimilant has high ε_{Hf} . Such mafic granulites have been found (e.g. Schmitz, Vervoort, Bowring, & Patchett, 2004), although they are not common (Vervoort et al., 1999).

Whether unradiogenic $^{206}\text{Pb}/^{204}\text{Pb}$ correlates with $+\Delta\varepsilon_{Hf}$ for SFVF samples is unclear. To my knowledge, only two SFVF samples have been directly analyzed for Pb, Hf, and Nd isotopes in a single study ($^{206}\text{Pb}/^{204}\text{Pb} = 18.297, 18.356$ and $\Delta\varepsilon_{Hf} = 2.1, 6.8$, respectively; Beard and C. M. Johnson, 1997). Nd and Hf – but not Pb – isotopes were measured on SFVF samples by Reid et al. (2012). In this study (and in Alibert et al., 1986), Sr, Nd, and Pb – but not Hf – were measured. Among the three studies there are too few overlapping samples to verify a correlation. However, in the Reid et al. (2012) data, the SFVF samples with the most unradiogenic ε_{Nd} also have large $+\Delta\varepsilon_{Hf}$ (cf. Figure 3a in Reid et al., 2012). As the SFVF magmas with the most unradiogenic ε_{Nd} are also those that experience highest degrees of assimilation, the deviation from the terrestrial $\varepsilon_{Nd-\varepsilon_{Hf}}$ array may be a product of assimilation in the deep crust. Further combined Nd-Sr-Hf-Pb studies must be conducted to test this hypothesis; such studies should focus not only on the most primitive samples, but also on those shown to have undergone deep AFC. In general, the isotopic characteristics of the SFVF are unusual, and the Hf characteristics relative to the other isotopic systems are no exception.

1.6 Implications for mantle processes

As noted in the introduction, the SFVF has a bimodal distribution of eruptive products, with a central region of relatively large, basalt-intermediate composite volcanoes, and a surrounding region of mostly monogenetic cones and flows of nominally basaltic composition. This distribution implies a correlated variation in magma production rates. In this section, I use the results of the AFC modeling to help clarify the magnitude of this difference in melt production rates.

The AFC model output includes the amounts of assimilation and crystal fractionation required to generate a specific chemical composition, and allows for calculation of the minimum total mass that must have entered the crust to account for the erupted column of lava. This minimum total mass (M_M) introduced into the system is related to the erupted mass (M_S), fractionated mass (F), and assimilated mass (A) by: $M_M = M_S - A + F$. This is a minimum total mass because it does not account for that magma which freezes beneath the surface, which could be substantial. For any given iteration in the AFC model, ratios of A/M_M and F/M_M are known. Assuming the surface mass is equivalent to the residual liquid mass, M_S/M_M is also known (the surface mass is computed from topography). If the extent of model progress can be constrained (the iteration where the model best fits the data), M_M can be calculated. Dividing by time yields a production rate.

Because the isotopes in the assimilant end-members are inferred and there is little evolution in the trace elements, I rely on the major elements to constrain the extent of AFC. I treat the <1 Ma SFVF as two main units: SF Mountain and the monogenetic field that surrounds it. To estimate the chemical compositions of these units, I use median values from the flows composing each unit (the distributions of most major elements are unimodal and slightly skewed; in practice, the median and mean nearly coincide for most elements). Although the SFVF is comprehensively mapped and major element data exist for most units, the thicknesses and lateral extents are ambiguous for many flows; hence the volumes and masses for these flows are poorly constrained, making a flow-by-flow method impractical.

The extent of AFC for any single model run is found by least squares minimization:

$$S_i = \sum_i (M_{model,i} - M_{median})^2 \quad (1.1)$$

where subscript i refers to the model iteration number, $M_{model,i}$ is the wt% of element M in the model run at iteration i , and $M_{median,i}$ is the wt% of element M in either the monogenetic field or SF Mountain. Each model run generates a vector S ; the minimum in S corresponds to the iteration wherein the model best approximates the chemical composition. To perform the minimization, SiO_2 , TiO_2 , Al_2O_3 , CaO , MgO , FeO_T , and K_2O are used (I have not included P_2O_5 or MnO in the modeling because they increase the difficulty of computational convergence. Na_2O is excluded from the minimization because of the misfit between the data and the model). For each run in the ensemble, the extent of AFC and an initial mass are calculated.

To generate model compositions equivalent to the $\sim 180 \text{ km}^3$ monogenetic field, the AFC ensemble requires only a slightly larger amount of initial primitive magma ($175\text{--}195 \text{ km}^3$). This does not mean that AFC does not occur, but rather that the material gained ($36\text{--}49 \text{ km}^3$ of assimilant) is balanced by the material fractionated ($37\text{--}48 \text{ km}^3$). For SF Mountain, the models require a minimum $520\text{--}935 \text{ km}^3$ initial material, assuming the stratovolcano's original volume was 350 km^3 (similar to modern Mt. Shasta or Mt. Adams, and consistent with its base area of $\sim 420 \text{ km}^2$). The models additionally suggest that $178\text{--}258 \text{ km}^3$ was assimilated, and the majority of that ($143\text{--}256 \text{ km}^3$) occurred in the deep crust. Significantly more shallow crystal fractionation occurred, as would be expected for magma chilled by the cool shallow crust. For both the monogenetic field and SF Mountain, the ensembles suggest that the assimilated mass is 20–30% that of the initial magma mass.

Given a lifespan of 0.6 Ma for SF Mountain and the implied growth rate of $\sim 580 \text{ km}^3/\text{Myr}$ (or $0.00058 \text{ km}^3/\text{yr}$; similar to Mt. Shasta), magma production rates are in the range $0.0009\text{--}0.00016 \text{ km}^3/\text{yr}$. In contrast, the monogenetic mafic field requires growth rates of $\sim 180 \text{ km}^3/\text{Myr}$ and comparable production rates, which are about 3 times lower than those required for the central volcano.

To directly compare magma genesis rates between the monogenetic field and SF Mountain, I normalize the production by area (420 km^2 for SF Mountain, 1000 km^2 for the $<1 \text{ Ma}$ monogenetic field). The normalized rates, in units of mm/yr , are shown for the ensemble of model runs in Figure 1.12. The absolute production rates are minima and likely semi-quantitative at best, but ratios of fluxes suggest the stratovolcano grew as a consequence of a 7- to 14-fold increase in melt production over the background rate, sustained from 1.0–0.6 Ma. Based on the results of the chemical and isotopic AFC modeling, this increase in flux does not appear to have been a consequence of melting a compositionally distinct source.

1.6.1 Source geochemistry and geobarometry

The enriched trace element characteristics of Colorado Plateau volcanic rocks (the SFVF included; Figures 1.7 and 1.8), could be attributed to relatively recent mass transfer from the Farallon slab (e.g. Humphreys et al., 2003); ancient metasomatism (e.g. Reid et al., 2012); and pyroxenite veining (e.g. Beard & C. M. Johnson, 1997).

In terms of the major element chemistry, primitive SFVF magmas share some characteristics with ocean island basalts (OIB) that have been attributed to melting of silica-depleted garnet pyroxenite: they have elevated $\text{CaO}/\text{Al}_2\text{O}_3$, consistently low Al_2O_3 relative to peridotite-derived melts, and they extend to low SiO_2 contents (green squares, Figure 1.13; for a review, see Lambart, Laporte, and Schiano, 2013). However, SFVF magmas lack the high FeO_T contents of garnet pyroxenite melts. Moreover, pyroxenite melts reach low Al_2O_3 and high $\text{CaO}/\text{Al}_2\text{O}_3$ as a consequence of increased garnet stability at greater pressures (Kogiso, Hirschmann, & Frost, 2003; Lambart, Laporte, & Schiano, 2013); therefore the major elements would require a deep, *garnet-rich* pyroxenite source.

Trace element abundances, however, are consistent with only small amounts of mantle garnet: non-modal batch melting calculations shown in Figures 1.14 and 1.15 suggest that

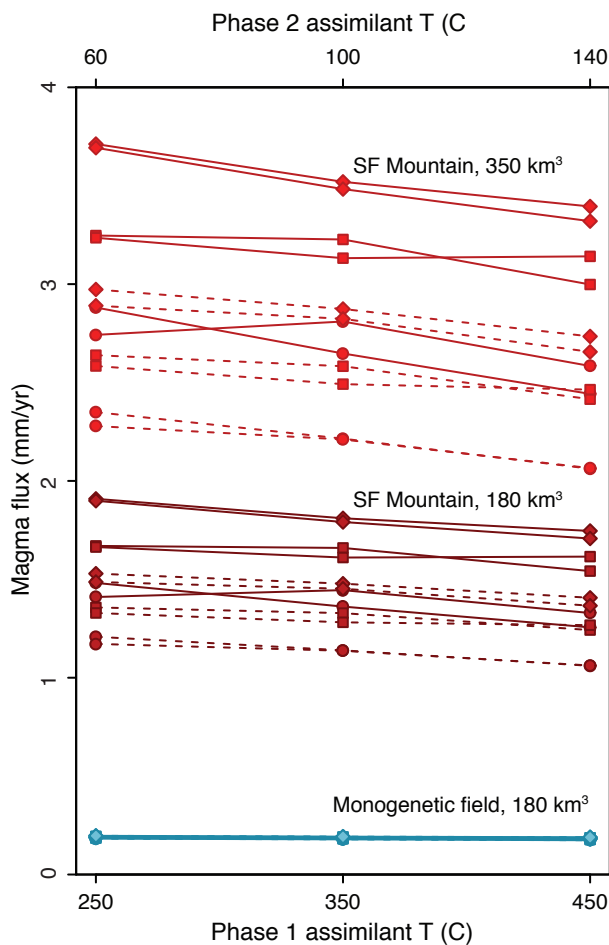


Figure 1.12: Plot of calculated magma production rates for the AFC ensemble. Monogenetic production rates indicated by blue and SF Mountain production rates indicated in red. For SF Mountain, two families of rates are shown, one assuming the current SF Mountain volume of 180 km^3 and one assuming 350 km^3 . In this plot, individual points represent single model runs, and they have been plotted against the temperatures of assimilants on the x-axis to show model temperature dependence. Additional model parameters are indicated by symbol and line-type. Solid lines are for runs wherein phase 1 AFC continued to $\text{Mg}\#=25$; dashed lines for $\text{Mg}\#=35$. Symbols indicate different degree melting of assimilants; circles are for low degree melting, squares for moderate degree melting, diamonds for high degree of melting.

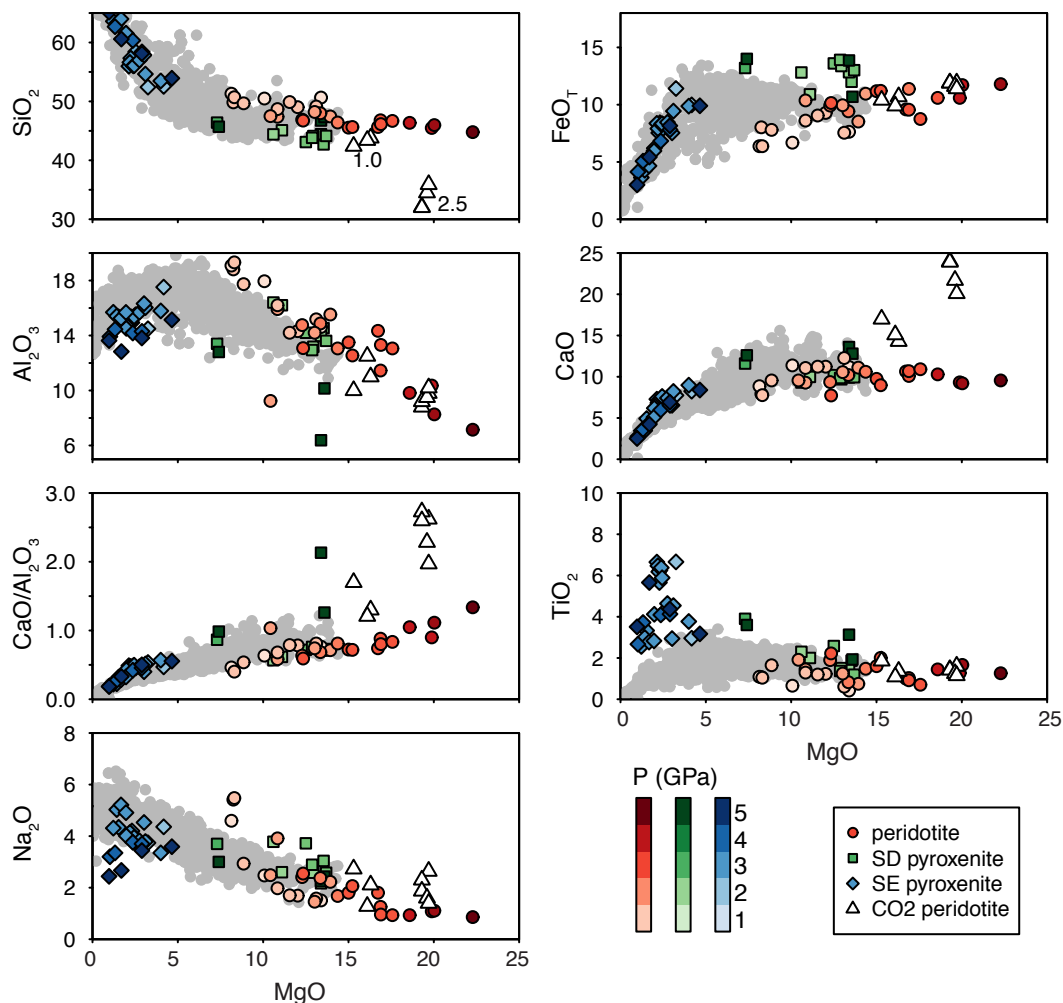


Figure 1.13: Comparison of SFVF magmas and experimental melts of different mantle lithologies. Circles (red-shaded) are peridotite melts; squares (green-shaded) are silica-deficient pyroxenite melts; diamonds (blue-shaded) are silica-enriched pyroxenite melts; triangles are carbonated peridotite melts. Numbers (1.0 and 2.5) refer to CO₂ wt% of the carbonated peridotite sources. Gradation in color schemes shows pressure at which individual experimental runs were carried out. Peridotite data are from Hirose and Kushiro (1993), Kushiro (1996), Walter (1998). Silica-deficient pyroxenite data are from Hirschmann, Kogiso, Baker, and Stolper (2003), Kogiso, Hirschmann, and Frost (2003), Keshav, Gudfinnsson, Sen, and Fei (2004), Kogiso and Hirschmann (2006). Silica-enriched pyroxenite data are from Pertermann and Hirschmann (2003), Spandler, Yaxley, Green, and Rosenthal (2007). Carbonated peridotite data are from Dasgupta, Hirschmann, and Smith (2007). The experimental data shown are filtered to include only results from 1.0 to 5.0 GPa experiments that yielded melt degrees <20% for peridotites and <50% for pyroxenites.

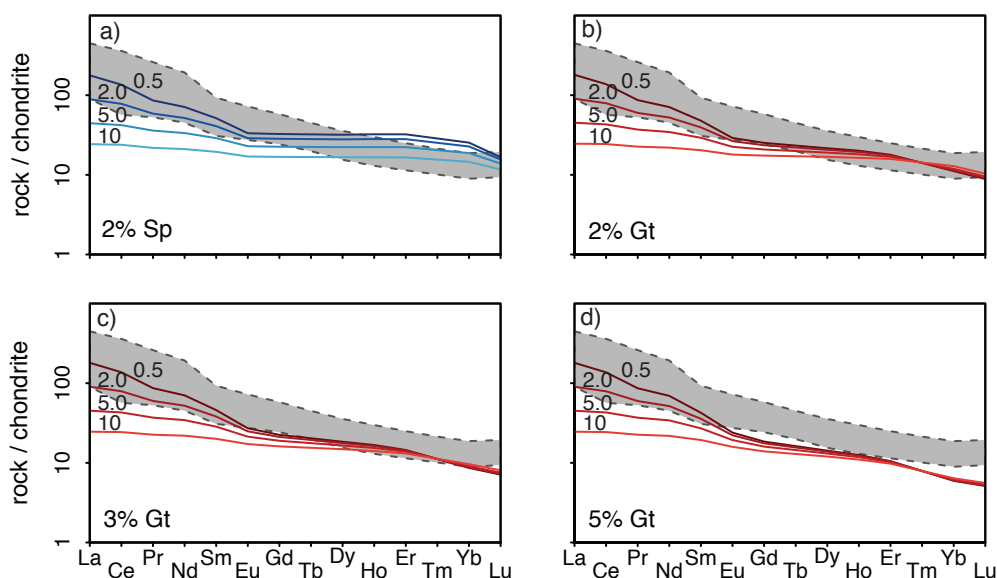


Figure 1.14: Trace element results of non-modal batch melting calculations (Shaw, 1970). (a)–(d) show results for REE modeling with 4 different mantle sources (SFVF monogenetic data are plotted as gray fields); numbers indicate F , degree of melting. Color indicates different mantle sources: blue for spinel-bearing mantle, red for garnet bearing sources; garnet and spinel abundances are as labeled. The initial mantle sources were modeled as 16% clinopyroxene, 26% orthopyroxene, 53–56% olivine, and either 2% spinel or 2–5% garnet (These modes were calculated from the major element depleted mantle composition of Salters and Stracke, 2004 at 2.0 GPa using MELTS). Initial mantle REE abundances are from the primitive mantle composition of Hofmann (1988). Melting modes are from Jourdan et al. (2007), after Walter (1998) and are clinopyroxene: 55%; orthopyroxene: 20%; olivine: 20%; spinel: 5% for spinel-bearing mantle; and clinopyroxene: 81%; orthopyroxene: -12%; olivine: 16%; garnet: 15% for garnet-bearing mantle. Partition coefficients are from the compilation of Halliday et al. (1995) and references therein, supplemented with additional data from Higuchi and Nagasawa (1969), Salters and Longhi (1999), Green, Blundy, Adam, and Yaxley (2000).

greater than ~ 3 wt% garnet results in excess depletion of HREE and Lu. The trace elements are best explained by low degree melting (up to $F = \sim 0.03$) of an enriched, dominantly peridotite mantle with only a few percent garnet; this is also consistent with the relatively restricted Zn/Fe ratios of $\sim 11 \times 10^4$ in SFVF magmas (cf. Reid et al., 2012; Le Roux, Lee, & Turner, 2010).

Although there are few data (experiments conducted at 3 GPa with 2.5 and 1.0 wt% CO_2 ; Dasgupta, Hirschmann, and Smith, 2007), melts of carbonated peridotite exhibit major element trends similar to SFVF magmas, including SiO_2 deficiency and elevated $\text{CaO}/\text{Al}_2\text{O}_3$ ratios (open triangles in Figure 1.13). There is evidence of fluid transfer from the Farallon slab during Laramide flat subduction in the high water contents of Colorado Plateau mantle xenoliths (Z.-X. A. Li, Lee, Peslier, Lenardic, & Mackwell, 2008; D. Smith & Griffin, 2005); in addition to H_2O , either CO_2 or carbonate may also have been transferred. Low degree melting of such a carbonated / hydrated garnet peridotite mantle could explain both the ma-

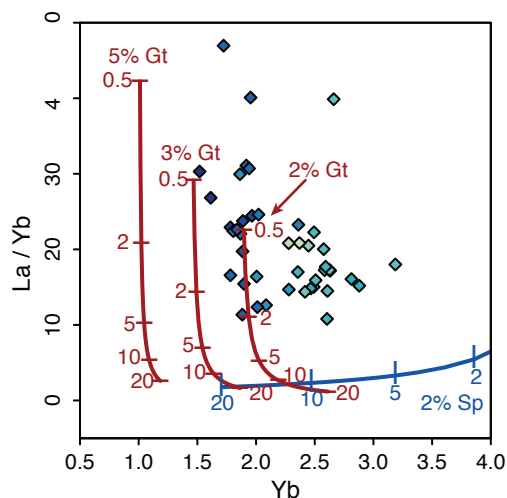


Figure 1.15: Non-modal batch melting calculations in La-Yb space. Lines show melting models with different mantle sources (as in Figure 1.14). Numbered ticks denote F . Also shown are SFVF data (mafic samples only); color scheme indicates sample $Mg\#$ as in Figure 1.9. Initial mantle source, melting modes, and partition coefficients are as in Figure 1.14.

major and trace element systematics in primitive SFVF magmas. Either significant pyroxenite was not present in the SFVF source, or any pyroxenite melts must have been subsequently reacted with peridotite (Mallik & Dasgupta, 2012; Lambart, Laporte, Provost, & Schiano, 2012). I also note that no SFVF products, including the more evolved magmas, have sufficiently high TiO_2 or low Al_2O_3 to be generated by melting silica-enriched pyroxenites (e.g. eclogites; blue diamonds, Figure 1.13).

Previous geobarometry estimates for SFVF magmas (in Reid et al., 2012, using the major element method of C.-T. A. Lee, Luffi, Plank, Dalton, and Leeman, 2009) suggest that magmas were formed in a pressure range of 3.5–1.3 GPa (120–50 km; Figure 1.16a). The maximum depth estimates are consistent with an asthenospheric source below the garnet-spinel transition. The shallowest depths are almost coincident with the Moho beneath the SFVF. This geobarometry (which I have filtered to samples with $68 < Mg\# < 73$, open circles in Figure 1.16a) suggests that a substantial proportion of SFVF magmas are generated in the subcontinental lithospheric mantle within the spinel stability field. However, trace elements require melting under garnet stability. In fact, melting of a garnet-free source overestimates HREE abundances (blue lines, Figure 1.14a). Additionally, the more primitive SFVF magmas have coupled low Yb and high La/Yb, and the latter are not sufficiently fractionated by partial melting of spinel peridotite (Figure 1.15).

The geobarometry of C.-T. A. Lee et al. (2009) is based on SiO_2 activity, and does not account for the potential effects of CO_2 . The first order result of a carbonated source is decreased SiO_2 ; thus pressures from this barometer would be overestimates. Additionally, the C.-T. A. Lee et al. (2009) calibration is based on experiments where liquids are in equilibrium

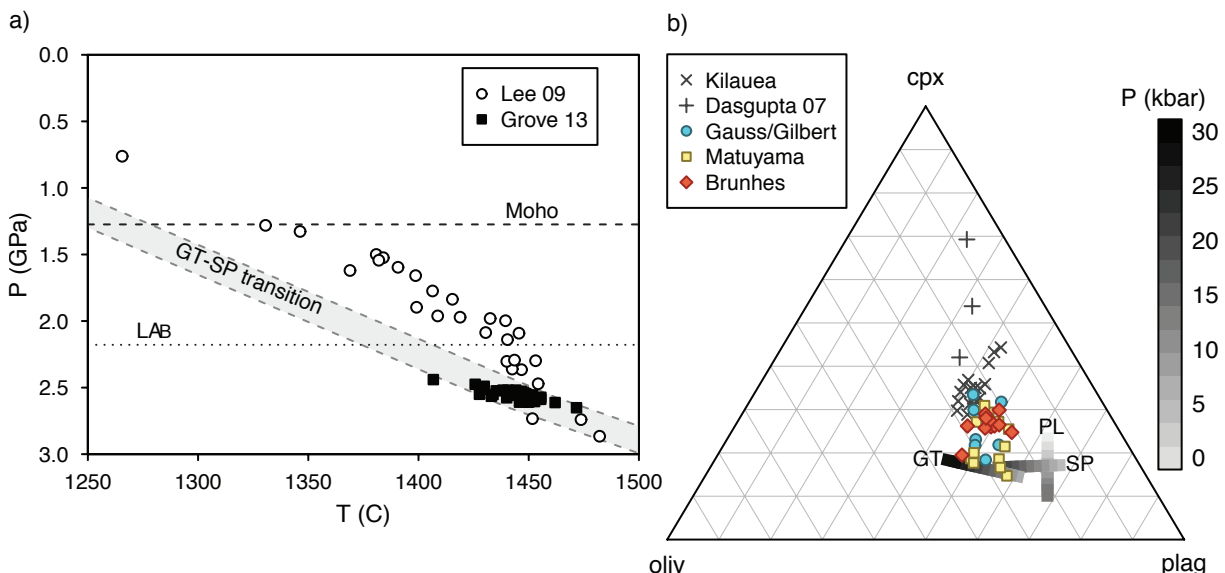


Figure 1.16: (a) Geobarometry and geothermometry of SFVF samples. Pressure and temperature estimates from geobarometry of C.-T. A. Lee et al. (2009) and Grove, Holbig, Barr, Till, and Krawczynski (2013), labeled “Lee 09” and “Grove 13”, respectively. Because even mafic SFVF samples show evidence of AFC, only samples with $68 < \text{Mg}\# < 73$ were used to estimate pressure and temperature, and no additional attempt was made to correct the samples for fractionation. The P/T-dependent garnet-spinel transition of Grove, Holbig, Barr, Till, and Krawczynski (2013) is also shown. Moho and lithosphere-asthenosphere boundary (LAB) depth are from Levander, Schmandt, et al. (2011). (b) Pseudo-ternary plot; olivine, plagioclase, quartz sub-projection (after Grove, Holbig, Barr, Till, & Krawczynski, 2013; Tormey, Grove, & Bryan, 1987); SFVF data are color-coded by paleomagnetic age as in Figure 1.3b; also shown are Kilauea basanite-nephelinite data from Sisson, Kimura, and Coombs (2009), and experimental melts of carbonated peridotite from Dasgupta et al. (2007). Solid gray-shaded lines show multiple saturation points for plagioclase, spinel, and garnet lherzolite (PL, SP, GT, respectively); gray-scale indicates pressure. These lines are calculated for the mean composition of the SFVF data shown, following equations in Till, Grove, and Krawczynski (2012), Grove, Holbig, Barr, Till, and Krawczynski (2013).

with olivine and orthopyroxene, whereas trace element modeling supports garnet on the liquidus. Using the geobarometry of Till, Grove, and Krawczynski (2012), Grove, Holbig, Barr, Till, and Krawczynski (2013), which is calibrated for multiple saturation with four phases (olivine, clinopyroxene, orthopyroxene, and plagioclase/spinel/garnet), I calculate more restricted pressure and temperature ranges for SFVF magmas, placing them at ~ 2.55 GPa (depth of 85 km), and 1400–1470° C. This calculation places the magma source depth beneath the LAB and at about the same pressure and temperature as the garnet-spinel transition (Figure 1.14). There may be some systematic error in these estimates as the Till et al. (2012), Grove et al. (2013) geobarometry has also not been calibrated for carbonated melts; however, these depths are consistent with the trace element modeling.

I note that many primitive SFVF samples do not plot near calculated multiple sat-

uration points for either garnet or spinel peridotite (the olivine-plagioclase-clinopyroxene sub-projection is shown in Figure 1.15). Instead, they overlap with Kilauea nephelinites and basanites thought to be products of carbonated lherzolite (Sisson, Kimura, and Coombs, 2009; and see discussion in Grove et al., 2013), which supports the interpretation of a carbonated peridotite source for the SFVF.

It is interesting to note that at least a few primitive SFVF samples plot near garnet multiple saturation points during the Gauss / Gilbert, and Matuyama epochs, while only one Brunhes point does so. Data are admittedly scarce, but if this is a temporal trend, it could suggest that during the Brunhes, the source of the SFVF was more CO₂-rich than during prior epochs.

1.6.2 Mantle dynamics and models for magma genesis

The total melt production rate (G , in km³/Myr) can be related to source geometry and dynamics by the scaling relationship $G = W \Gamma h A$, where W is the mantle upwelling velocity (km/Myr), Γ is a mantle production factor (fraction of melt produced per km, or units of km⁻¹), h is vertical dimension of the melting column (km), and A is the area of the melting region (km²). For the core of the SFVF source, $G = 500\text{--}900$ km³/0.6 Myr, and $A = 400$ km² (about the basal area of the stratovolcano). For the monogenetic field, $G = 180$ km³/1 Myr and $A = 1000$ km² (an area which includes the <1 Ma monogenetic cones and vents but excludes laterally extensive sheets that flowed to the northeast edge of the field). Γ ranges over an order of magnitude for Earth volcanism, from ~ 0.00035 km⁻¹ to as much as 0.0033 km⁻¹ for mid-ocean ridges (Plank, Spiegelman, & Langmuir, 1995). The production factor for plumes may be intermediate; for Hawaii, an average of 6.6% melt, generated in a column of $h = 55$ km (Watson & McKenzie, 1991), requires $\Gamma = 0.0012$. I assume $\Gamma = 0.001$ as an upper bound for the SFVF source. The vertical extent of the melting region, h , is constrained by geobarometry. SFVF samples cluster around ~ 2.55 GPa, but these are average equilibration depths, and may not indicate the base of the melting region. I assume melting occurs from 2.9 to 2.2 GPa (up to about the LAB depth), yielding $h = \sim 23$ km. This produces an average of 2.2% melt, consistent with trace element modeling (but a lower degree than previously estimated; cf. Reid et al., 2012).

Using these constraints, calculated upwelling velocities are 5.5–10 cm/yr in the core of the SFVF source and 0.8 cm/yr at the margins. Using the minimum $\Gamma = 0.00035$ produces an average of 0.8% melt and upwelling velocities of 16–28 cm/yr and 2.3 cm/yr in the core and margins, respectively. For reference, similar scaling arguments for the Hawaiian plume ($\Gamma = 0.0012$, $A = 1000$ km², $h = 55$ km, $G = 0.1\text{--}0.2$ km³/yr) suggest upwelling rates orders of magnitude greater, from $\sim 150\text{--}300$ cm/yr. The marginal rate, over the lifespan of the field, requires a mantle domain of $\sim 50\text{--}140$ vertical km. The core rate, sustained for only 0.6 Myr, requires a domain of similar size, $\sim 30\text{--}170$ km. If the SFVF is reaching the end of its lifespan (as suggested by decreasing vent production in the past 100 ka), these dimensions may be maxima.

The duration, upwelling rates, mini-plume characteristics, and major element geochemistry of the SFVF can be explained by decompression melting of a spatially limited CO₂- and H₂O-rich mantle domain. Both trace element modeling and geobarometry require deep melting, below the LAB and the garnet-spinel transition. Much of the evidence points to decompression of asthenosphere, possibly re-fertilized as a consequence of flat subduction during Laramide time. However, the most primitive SFVF magmas are isotopically distinct from the convecting, depleted mantle; their OIB-like Pb, Sr, and Nd compositions require a domain, such as Proterozoic subcontinental lithosphere, that was isolated for a substantial stretch of geologic time of order 1 billion years. Either asthenospherically-derived melts received their lithospheric imprint during transit through the lithosphere (which may perhaps explain the shallow depths calculated by the C.-T. A. Lee et al., 2009 barometer), and / or lithospheric mantle was recycled into the asthenosphere.

One possible recycling mechanism is delamination, although this is unlikely to have produced the SFVF for several reasons. The field is located too far south to be related to the currently-in-progress delamination, and volcanism in the field is migrating orthogonally to the direction of delamination propagation (cf. Levander, Schmandt, et al., 2011; Reid et al., 2012). Additionally, the foundering material appears to include lowermost crust (Levander, Schmandt, et al., 2011), which should be pyroxenite or eclogite (Wendlandt, DePaolo, & Baldrige, 1993), neither of which can be present in the SFVF source in significant quantities based on geochemical arguments. Finally, localized delamination provides no explanation as to why the Transition Zone should be the focus of numerous volcanic fields.

Small-scale convection is an alternate mechanism for subcontinental lithospheric recycling. In edge-driven convection models, hydrated, lower viscosity subcontinental lithospheric mantle is entrained in the downgoing limbs of convection cells (King & Ritsema, 2000; van Wijk et al., 2010). By this mechanism, ancient, isotopically distinct peridotite mantle could have been recently enriched, hydrated, carbonated, and then peeled away from the base of the Colorado Plateau lithosphere by convecting asthenosphere. The ability of edge-driven cells to move these re-fertilized upwelling domains to the right place depends on the geometry of the convection. The characteristic length-scale is apparently model dependent: for instance, King and Ritsema (2000) and King (2007) model large convection cells where the upwelling is 660–1000 km from edges, while van Wijk et al. (2010) predict smaller cells, with upwelling centered beneath the Transition Zone.

The mini-plume-like characteristics and the geochemistry of the SFVF are not easily reconciled with a delamination origin. Edge-driven convection, however, provides a viable method for recycling and upwelling re-fertilized mantle. In addition, it could explain the clustering of volcanic fields along the TZ. Edge-driven convection cannot, by itself, explain the mini-plume-like nature of the SFVF. I suggest a hybrid model, where a fertile mantle domain entrained by edge-driven convection experienced buoyant decompression melting. The rapid upwelling in the core of the SFVF could be a consequence of buoyancy feedback from melting a CO₂-, H₂O-rich domain (e.g. Tackley & Stevenson, 1993; Raddick, 2002), resulting in the pulse of productivity from ~1.0–0.4 Ma that produced the SF Mountain stratovolcano. In this sense, while the SFVF has mini-plume-like characteristics, it is different

from the European Cenozoic volcanic provinces, like Eifel and the French Massif Central, in that it has no 400 km-long conduit of upwelling material (e.g. Granet et al., 1995); nor does it require one.

1.7 Conclusions

The petrographic, major element, trace element, and isotopic trends exhibited by young (<1 Ma) SFVF magmas are consistent with ubiquitous mid or deep crust assimilation accompanied by fractional crystallization (AFC), where mafic-to-intermediate composition granulite is assimilated and mostly clinopyroxene is fractionated. The SFVF stratovolcano magmas lie on continuous chemical and isotopic evolutionary trends with the monogenetic magmas, precluding a significantly different source composition, although they require a 7- to 14-fold increase in magma flux from the mantle, sustained over 0.6 Myr, above the background magma generation rates.

Isenthalpic AFC modeling with the alphaMELTS software package is successfully able to reproduce most of the observed evolutionary trends; it works best at mafic to intermediate compositions, and appears to be less reliable for silicic and/or water-rich magmas. From the AFC modeling, I infer unradiogenic (in terms of Sr, Pb, and Nd) compositions for the granulite assimilant, which results in a trend in $^{87}\text{Sr}/^{86}\text{Sr}-\varepsilon_{\text{Nd}}$ space orthogonal to the mantle array. This trend can be entirely explained by deep crust assimilation, and suggests the possibility that the anomalous ε_{Hf} characteristics observed in some SFVF magmas may also be due to deep assimilation. The most evolved (rhyolite) samples associated with the central SF Mountain stratovolcano show evidence of a second stage of AFC involving radiogenic Sr. The contrast between the radiogenic shallow and unradiogenic deep crust allows me to effectively distinguish between shallow and deep assimilation.

The major and trace element geochemistry of the most primitive SFVF magmas are consistent with genesis by low degree melting (melt fraction up to 0.03) of a fluid-enriched, hydrated / carbonated peridotite mantle source, within the garnet stability field. Trace element abundances are inconsistent with pyroxenite melting, but do require 1-3 wt% garnet in the melt residue. Geobarometry (using the methods of Till et al., 2012; and Grove et al., 2013) suggests melting within the garnet stability field at pressures of ~ 2.55 GPa (85 km depth), just below the seismically-imaged lithosphere-asthenosphere boundary. Assuming the LAB caps the upwelling column, the mantle upwelling rate may reach 10–28 cm/yr in the core of the magma-producing region (responsible for genesis of SF Mountain, sustained over 0.6 Myr). Lower upwelling rates of 0.8–2.2 cm/yr are sufficient to generate the surrounding monogenetic field.

Although geobarometry suggests asthenospheric depths for basaltic magma generation, isotope ratios of the most primitive SFVF magmas are compositionally distinct from the typical convecting, depleted mantle as represented by mid-ocean ridge basalts and most other oceanic basalts. This difference could be a result of ancient subcontinental lithosphere being recycled into the convecting mantle by delamination or edge-driven convection,

but the former process is incompatible with the geochemistry of SFVF magmas, the mini-plume-like characteristics of the field, and its location with respect to inferred delamination. Alternatively, a hydrated, carbonated, low-viscosity domain could have been removed from the Colorado Plateau subcontinental lithospheric mantle, leading to buoyant decompression melting that gave rise to the SFVF.

Table 1.1: Major and trace elements.

Sample ID	03HSF-1	03HSF-2	03HSF-3	03HSF-4	03HSF-5	03HSF-6	03HSF-7	03HSF-8
Lat	35.2499	35.2848	35.3174	35.3441	35.3170	35.3577	35.3632	35.3627
Long	111.7644	111.7672	111.7716	111.7477	111.7360	111.7620	111.7521	111.7424
Unit	Mono	Mono	Mono	Mono	SF Mtn	Mono	Mono	Mono
SiO ₂	59.59	49.72	49.27	51.76	64.66	52.11	51.61	51.39
TiO ₂	0.86	2.82	2.94	2.37	0.39	2.23	2.21	2.37
Al ₂ O ₃	17.67	17.30	17.23	17.40	16.32	17.39	17.40	17.44
FeO _T	5.35	11.82	12.12	11.01	4.41	10.63	10.65	10.89
MnO	0.18	0.18	0.18	0.17	0.13	0.17	0.18	0.17
MgO	1.50	4.19	4.53	3.73	0.37	3.23	2.94	3.74
CaO	3.35	6.69	6.92	6.41	1.98	6.23	5.95	6.41
Na ₂ O	6.29	4.76	4.54	4.68	5.32	4.72	4.89	4.68
K ₂ O	2.88	1.46	1.42	1.83	3.60	1.87	1.93	1.83
P ₂ O ₅	0.63	0.66	0.62	0.76	0.12	0.78	0.79	0.76
Sum	98.28	99.60	99.77	100.13	97.29	99.36	98.55	99.69
LOI	0.29	-0.08	-0.35	-0.11	1.68	0.12	0.20	-0.34
Mg#	33.37	38.73	39.99	37.66	12.99	35.14	32.95	37.95
Ni	3.95	7.29	10.73	12.55	3.64	6.48	4.86	12.85
Cr	1.52	0.00	0.40	1.32	3.24	0.30	0.00	0.81
V	15.38	118.81	134.19	140.47	3.34	113.85	112.33	140.36
Ga	20.95	16.80	17.00	21.05	22.97	21.86	21.96	20.54
Cu	3.04	21.76	25.70	30.87	4.05	20.75	15.08	26.01
Zn	114.96	87.64	89.56	110.61	99.58	104.74	117.39	109.19
La	106.13	37.43	36.56	45.18	73.82	44.56	45.34	45.89
Ce	220.54	77.93	72.90	86.85	135.66	90.16	91.57	86.67
Pr	24.70	9.84	9.39	10.67	15.14	10.97	11.28	11.34
Nd	90.02	41.26	39.57	43.03	54.06	43.87	44.47	45.36
Sm	14.24	8.90	8.59	8.68	9.85	8.78	9.02	9.05
Eu	3.87	2.92	2.87	2.75	2.35	2.77	2.83	2.82
Gd	9.26	7.81	7.63	7.78	7.90	7.65	7.81	7.97
Tb	1.25	1.17	1.15	1.15	1.24	1.14	1.17	1.19
Dy	6.45	6.52	6.42	6.43	7.27	6.44	6.53	6.64
Ho	1.19	1.24	1.22	1.27	1.42	1.23	1.25	1.25
Er	3.05	3.06	3.03	3.15	3.84	3.17	3.18	3.21
Tm	0.43	0.41	0.41	0.43	0.58	0.43	0.44	0.44
Yb	2.66	2.49	2.47	2.63	3.66	2.58	2.63	2.59
Lu	0.41	0.37	0.36	0.39	0.58	0.40	0.41	0.40
Ba	1914.07	575.79	580.22	736.14	1429.06	764.06	785.95	752.58
Th	6.51	3.16	3.01	3.34	10.17	3.64	3.81	3.28
Nb	50.02	38.51	36.46	37.17	46.91	39.52	40.86	36.91
Y	31.22	30.58	30.48	32.29	36.61	31.01	31.31	31.53
Hf	7.50	4.97	4.83	5.16	10.21	5.40	5.67	5.13
Ta	2.67	2.15	2.02	2.11	2.77	2.34	2.44	2.22
U	1.70	0.78	0.77	0.62	4.09	1.14	1.22	0.46
Pb	17.81	4.23	4.08	6.84	19.59	5.17	5.98	6.18
Rb	28.62	16.21	17.92	14.26	58.46	17.68	19.42	14.09
Cs	0.28	0.15	0.27	0.08	1.60	0.20	0.10	0.04
Sr	1384.98	1067.47	1004.87	738.89	331.49	757.51	736.62	730.01
Sc	4.75	13.55	14.53	14.53	4.87	13.12	13.26	15.02
Zr	369.23	221.86	213.83	228.23	480.75	243.75	251.95	227.38

Table 1.1: Continued

Sample ID	03HSF-9	03HSF-10	03HSF-11	03HSF-12	03HSF-13	03HSF-14	03HSF-15	03HSF-16
Lat	35.2843	35.3734	35.3781	35.4278	35.4393	35.4312	35.4528	35.4425
Long	111.8360	111.8842	111.9011	111.9235	111.7711	111.7857	111.7539	111.6888
Unit	Mono							
SiO ₂	47.95	54.27	53.66	47.36	48.40	48.86	48.40	48.84
TiO ₂	3.11	2.03	2.12	2.28	2.40	2.48	1.86	2.92
Al ₂ O ₃	16.90	17.10	17.30	16.51	16.40	16.65	18.46	17.34
FeO _T	13.45	9.81	10.28	11.80	13.11	12.45	10.87	11.90
MnO	0.19	0.16	0.17	0.17	0.23	0.20	0.18	0.17
MgO	4.75	3.03	3.15	5.80	3.61	4.50	5.43	2.89
CaO	6.99	5.53	5.54	9.44	5.96	6.94	8.91	6.36
Na ₂ O	4.65	4.96	4.92	3.43	4.79	4.33	4.04	4.73
K ₂ O	1.37	2.13	2.08	0.93	1.84	1.52	0.73	1.38
P ₂ O ₅	0.57	0.54	0.55	0.42	1.63	1.10	0.80	0.77
Sum	99.92	99.57	99.77	98.16	98.40	99.04	99.67	97.29
LOI	-0.09	-0.55	-0.27	1.35	-0.02	-0.42	-0.37	0.89
Mg#	38.63	35.52	35.35	46.72	32.95	39.18	47.09	30.19
Ni	22.97	4.25	4.55	81.06	15.48	32.59	24.09	7.79
Cr	4.15	0.00	0.00	195.42	3.85	20.24	10.52	0.00
V	169.31	105.45	113.04	241.67	62.54	108.79	213.53	132.17
Ga	19.73	20.85	20.95	20.04	21.05	21.56	18.42	16.80
Cu	41.29	17.81	21.25	42.50	15.79	32.38	29.96	18.11
Zn	105.86	110.00	114.05	95.84	132.27	119.11	84.20	78.94
La	28.11	39.91	37.80	26.30	57.37	43.70	55.80	34.76
Ce	60.60	78.92	76.25	51.09	125.82	92.41	103.33	73.83
Pr	7.94	9.57	9.22	6.28	15.67	11.88	11.93	9.36
Nd	34.09	37.55	36.71	25.53	65.46	50.49	44.98	38.87
Sm	7.93	7.84	7.90	5.77	13.59	10.84	8.02	8.39
Eu	2.67	2.43	2.46	1.95	4.19	3.50	2.44	2.80
Gd	7.43	6.98	7.02	5.62	11.91	9.67	6.10	7.45
Tb	1.14	1.05	1.07	0.88	1.68	1.42	0.87	1.11
Dy	6.46	6.00	6.03	5.16	9.04	7.84	4.67	6.25
Ho	1.24	1.16	1.18	0.99	1.69	1.47	0.91	1.17
Er	3.14	3.04	3.09	2.54	4.14	3.68	2.25	2.96
Tm	0.44	0.42	0.42	0.35	0.54	0.49	0.31	0.41
Yb	2.60	2.51	2.61	2.09	3.19	2.88	1.86	2.42
Lu	0.40	0.40	0.40	0.31	0.49	0.43	0.27	0.37
Ba	380.51	766.77	772.22	492.50	791.87	997.40	811.36	636.47
Th	2.15	3.75	3.49	3.29	3.87	3.01	6.53	3.13
Nb	30.56	31.75	31.61	28.94	42.88	35.47	33.77	39.99
Y	31.00	29.45	29.79	24.79	42.21	37.31	22.39	29.44
Hf	5.03	5.65	5.64	3.65	5.82	4.95	2.91	4.92
Ta	1.97	2.00	1.98	1.66	2.63	2.15	1.64	2.42
U	0.69	0.82	0.89	0.90	0.70	0.46	1.53	0.91
Pb	2.89	7.37	6.89	3.77	6.00	4.68	5.45	3.82
Rb	13.82	20.58	19.60	11.08	17.62	13.49	5.67	16.51
Cs	0.16	0.24	0.16	0.28	0.11	0.08	0.03	0.20
Sr	798.56	651.76	640.32	650.84	736.08	757.43	1188.31	1113.07
Sc	16.45	12.62	13.26	25.49	11.79	14.85	18.06	13.23
Zr	220.79	249.00	249.65	152.77	256.03	216.40	123.34	215.60

Table 1.1: Continued

Sample ID	03HSF-17	03HSF-18	03HSF-19	03HSF-20	03HSF-21	03HSF-22	03HSF-23	03HSF-24
Lat	35.4375	35.4313	35.4296	35.4121	35.3981	35.3983	35.3935	35.3988
Long	111.6598	111.6711	111.6660	111.6686	111.6488	111.6325	111.6157	111.6107
Unit	Mono	Mono	Mono	Mono	SF Mtn	SF Mtn	SF Mtn	SF Mtn
SiO ₂	49.84	48.79	46.29	47.87	61.06	63.78	62.28	62.28
TiO ₂	1.39	2.47	2.03	2.69	1.07	0.69	0.75	0.72
Al ₂ O ₃	13.65	16.78	16.41	17.51	15.97	15.93	16.73	16.90
FeO _T	8.67	11.48	11.01	12.43	6.18	5.16	5.64	5.47
MnO	0.17	0.19	0.18	0.18	0.12	0.12	0.13	0.13
MgO	8.80	5.09	7.69	4.14	1.78	1.01	1.29	1.24
CaO	11.84	8.16	10.76	7.35	4.05	2.83	3.79	3.81
Na ₂ O	2.98	4.17	3.43	4.33	4.53	5.06	5.01	4.91
K ₂ O	1.38	1.17	0.93	1.33	2.98	3.29	2.41	2.46
P ₂ O ₅	0.91	0.71	0.75	0.70	0.47	0.31	0.47	0.44
Sum	99.63	99.01	99.49	98.54	98.21	98.18	98.50	98.36
LOI	-0.12	0.00	-0.22	0.57	0.48	0.89	0.66	1.33
Mg#	64.40	44.17	55.46	37.26	33.95	25.79	29.00	28.83
Ni	124.48	33.90	85.51	19.33	4.66	3.24	3.14	3.95
Cr	310.08	40.18	92.60	3.85	1.82	3.04	2.43	2.13
V	232.05	158.28	244.80	156.66	57.28	17.61	24.69	22.26
Ga	18.32	19.53	19.84	18.11	20.44	19.53	19.53	20.85
Cu	101.91	29.75	79.54	21.25	12.35	1.42	6.48	6.58
Zn	75.19	100.09	98.47	99.07	88.15	83.19	89.26	90.98
La	101.24	33.46	59.60	40.05	47.12	50.07	44.47	43.19
Ce	195.15	69.28	116.30	81.88	89.92	92.91	85.91	82.77
Pr	21.17	8.75	13.44	10.26	10.44	10.51	10.06	9.77
Nd	76.40	36.22	51.09	41.62	39.01	38.41	37.34	36.30
Sm	11.49	7.62	8.99	8.53	7.60	7.17	6.82	6.52
Eu	2.87	2.79	2.70	2.72	1.99	1.96	2.05	1.98
Gd	7.15	6.99	6.93	7.37	6.33	5.87	5.41	5.30
Tb	0.90	1.04	0.95	1.10	0.96	0.91	0.81	0.78
Dy	4.62	5.91	5.23	6.13	5.53	5.30	4.49	4.32
Ho	0.83	1.12	0.96	1.15	1.07	1.05	0.87	0.84
Er	2.02	2.81	2.43	2.90	2.77	2.80	2.27	2.18
Tm	0.27	0.39	0.32	0.39	0.40	0.41	0.32	0.31
Yb	1.59	2.28	1.92	2.36	2.47	2.59	1.98	1.94
Lu	0.25	0.34	0.29	0.36	0.38	0.40	0.31	0.30
Ba	1375.88	600.67	879.20	568.40	961.89	1015.66	1113.55	1178.76
Th	13.53	2.88	7.44	3.75	7.67	8.13	4.86	4.54
Nb	59.40	30.38	45.95	39.73	33.31	41.12	35.96	34.83
Y	20.59	27.78	24.08	28.83	27.21	26.77	22.51	21.69
Hf	4.37	4.16	3.73	5.03	5.97	7.10	5.93	5.86
Ta	2.96	1.86	2.49	2.41	2.27	3.03	2.36	2.25
U	3.56	0.81	1.90	0.73	2.78	2.74	1.80	1.63
Pb	8.98	3.78	5.53	4.25	15.13	15.56	12.70	12.53
Rb	14.42	13.85	11.01	17.59	45.14	42.03	31.98	29.27
Cs	0.36	0.09	0.21	0.61	1.34	0.97	0.61	0.55
Sr	1016.29	748.35	985.03	937.27	541.46	450.57	738.74	775.30
Sc	31.18	20.22	26.94	16.13	8.57	5.97	5.09	5.13
Zr	185.95	179.97	162.51	222.86	239.57	300.98	261.28	259.35

Table 1.1: Continued

Sample ID	03HSF-25	03HSF-26	03HSF-27	03HSF-28	03HSF-29	03HSF-30	03HSF-31	03HSF-32
Lat	35.2590	35.2615	35.2443	35.2414	35.2471	35.2986	35.3192	35.2854
Long	111.6200	111.6114	111.6010	111.6502	111.6654	111.7137	111.7207	111.6139
Unit	Mono	Mono	Mono	Mono	SF Mtn	SF Mtn	SF Mtn	SF Mtn
SiO ₂	61.66	65.73	65.04	48.69	64.43	60.45	60.25	59.52
TiO ₂	0.90	0.48	0.56	1.29	0.49	0.97	0.97	1.08
Al ₂ O ₃	16.45	16.16	16.35	15.19	16.83	16.41	16.55	17.13
FeO _T	6.30	4.63	4.66	10.94	4.68	6.47	6.73	6.27
MnO	0.14	0.11	0.11	0.18	0.11	0.14	0.14	0.17
MgO	1.24	0.59	0.66	7.91	0.65	1.48	1.50	1.39
CaO	3.41	2.30	2.47	9.47	2.51	3.78	3.68	4.00
Na ₂ O	5.24	5.42	5.39	2.94	5.24	4.91	4.97	5.42
K ₂ O	2.91	3.26	3.23	0.48	3.26	2.91	2.89	2.46
P ₂ O ₅	0.46	0.23	0.25	0.21	0.25	0.52	0.49	0.53
Sum	98.70	98.90	98.71	97.28	98.44	98.03	98.16	97.96
LOI	0.00	0.13	0.39	0.23	1.42	0.80	0.48	0.50
Mg#	25.91	18.46	20.08	56.30	19.77	28.99	28.44	28.30
Ni	4.35	2.73	4.96	191.27	2.83	4.55	3.74	4.05
Cr	1.62	2.23	4.55	405.81	2.43	1.62	1.21	0.91
V	24.79	7.69	12.95	206.45	12.85	27.53	26.51	26.41
Ga	21.96	20.14	19.43	18.32	20.64	20.85	19.53	21.35
Cu	7.39	3.85	4.76	93.00	5.67	4.25	6.98	3.74
Zn	95.13	66.59	72.05	103.22	76.30	97.05	96.24	107.37
La	50.14	49.39	47.42	21.37	50.11	48.40	50.00	80.27
Ce	93.98	89.86	94.28	34.74	92.01	91.36	92.67	120.01
Pr	10.79	9.92	10.05	5.02	10.08	10.57	10.97	17.32
Nd	39.81	35.35	35.95	21.09	35.38	39.65	40.52	64.16
Sm	7.42	6.45	6.47	4.72	6.34	7.45	7.49	11.22
Eu	2.03	1.77	1.83	1.59	1.81	2.10	2.07	2.87
Gd	6.13	5.19	5.23	4.98	5.05	6.13	6.28	9.00
Tb	0.92	0.81	0.81	0.79	0.79	0.95	0.95	1.33
Dy	5.19	4.71	4.68	4.64	4.48	5.34	5.35	7.44
Ho	1.01	0.91	0.91	0.91	0.88	1.03	1.03	1.44
Er	2.67	2.44	2.44	2.31	2.37	2.71	2.68	3.72
Tm	0.38	0.37	0.36	0.31	0.35	0.39	0.38	0.54
Yb	2.45	2.37	2.28	1.88	2.29	2.47	2.44	3.35
Lu	0.37	0.36	0.35	0.29	0.35	0.38	0.38	0.51
Ba	928.09	1007.72	1013.82	468.29	1058.49	879.76	895.58	1104.91
Th	8.04	8.56	8.53	1.69	9.04	7.50	7.78	7.63
Nb	41.00	40.04	41.37	11.01	40.75	39.77	40.31	48.69
Y	25.86	24.06	23.10	24.00	22.58	26.97	26.40	35.29
Hf	6.98	7.12	7.42	2.27	6.98	6.67	6.73	6.76
Ta	2.98	3.14	3.14	0.68	3.27	2.88	2.94	2.91
U	2.72	2.83	2.67	0.56	2.79	2.51	2.36	2.74
Pb	12.82	11.47	13.76	2.90	14.27	12.55	13.01	17.96
Rb	44.47	44.56	42.94	6.11	40.37	41.44	37.14	36.79
Cs	0.53	0.78	0.57	0.19	0.96	0.95	0.86	0.41
Sr	485.53	438.46	441.08	410.25	480.62	525.03	508.93	687.95
Sc	5.54	3.74	4.31	25.22	3.37	5.39	5.71	7.37
Zr	296.46	299.28	312.65	86.77	295.94	285.60	288.03	290.38

Table 1.1: Continued

Sample ID	03HSF-33	03HSF-34	03HSF-35	03HSF-36	03HSF-37	03HSF-38	03HSF-39	03HSF-40
Lat	35.2943	35.3393	35.3597	35.3820	35.3799	35.3776	35.2782	35.2455
Long	111.6076	111.5798	111.6171	111.5842	111.4497	111.4492	111.5238	111.4714
Unit	SF Mtn	SF Mtn	SF Mtn	Mono	Mono	Mono	Mono	Mono
SiO ₂	65.83	64.19	72.91	47.12	47.88	47.94	50.08	57.75
TiO ₂	0.47	0.53	0.02	1.39	1.35	1.86	1.65	0.96
Al ₂ O ₃	16.10	16.76	13.33	12.54	15.36	16.31	15.93	15.36
FeO _T	4.36	4.50	0.72	9.41	10.13	11.19	10.17	6.35
MnO	0.12	0.14	0.08	0.18	0.18	0.18	0.18	0.13
MgO	0.61	0.80	0.01	12.60	9.92	8.45	5.72	4.31
CaO	1.94	2.26	0.39	11.99	11.29	10.30	8.88	6.81
Na ₂ O	5.62	5.71	4.51	2.16	2.85	3.25	3.91	3.99
K ₂ O	3.92	3.18	4.27	0.67	0.54	0.80	1.31	2.54
P ₂ O ₅	0.18	0.33	0.01	0.62	0.48	0.46	0.74	0.52
Sum	99.15	98.40	96.24	98.68	99.98	100.71	98.58	98.72
LOI	0.26	0.27	2.20	-0.35	-0.16	-0.68	0.48	0.50
Mg#	20.02	23.94	1.32	70.49	63.57	57.36	50.04	54.71
Ni	4.55	4.76	4.05	263.93	171.94	125.39	91.38	46.35
Cr	3.74	3.24	4.96	1033.15	363.71	259.27	315.14	89.56
V	10.22	8.30	3.34	249.15	237.52	239.54	164.05	139.86
Ga	22.26	18.32	29.35	14.78	17.71	19.53	18.42	17.51
Cu	6.38	5.97	2.43	88.85	78.94	68.61	62.04	51.92
Zn	97.76	90.68	103.12	78.03	94.01	100.59	101.71	69.93
La	75.20	71.48	14.13	46.04	40.83	29.27	54.90	80.92
Ce	145.98	139.89	33.80	90.20	76.50	57.94	106.10	151.27
Pr	15.33	14.13	4.46	10.89	8.93	7.23	12.64	15.26
Nd	53.02	48.71	17.10	41.33	34.09	29.28	48.40	52.87
Sm	9.08	7.82	6.06	7.24	6.28	6.16	8.87	7.98
Eu	1.61	2.28	0.01	2.08	1.99	2.00	2.58	2.12
Gd	7.15	5.58	6.58	5.45	5.33	5.46	7.22	5.35
Tb	1.13	0.81	1.35	0.74	0.77	0.83	1.05	0.74
Dy	6.60	4.51	8.94	3.93	4.49	4.75	5.84	3.98
Ho	1.31	0.88	1.82	0.73	0.84	0.91	1.10	0.75
Er	3.63	2.34	5.52	1.89	2.13	2.32	2.78	1.94
Tm	0.54	0.35	0.93	0.26	0.29	0.32	0.40	0.28
Yb	3.52	2.27	6.44	1.52	1.78	1.90	2.36	1.72
Lu	0.53	0.37	1.00	0.24	0.26	0.29	0.36	0.28
Ba	1200.63	1716.11	11.87	799.27	610.63	493.80	915.99	1269.83
Th	12.16	7.30	32.96	5.94	5.20	2.76	6.93	11.61
Nb	57.28	44.46	123.78	38.39	28.88	26.96	42.78	43.01
Y	34.99	23.14	63.77	18.44	21.21	22.47	28.11	19.09
Hf	9.78	8.64	6.25	2.97	2.62	3.28	4.69	5.66
Ta	3.64	2.68	18.08	2.07	1.36	1.49	2.25	2.23
U	3.48	2.11	15.29	1.51	1.38	1.03	1.60	3.55
Pb	16.00	13.97	52.92	4.50	4.94	3.50	7.83	11.64
Rb	65.52	39.53	267.32	8.37	5.55	9.59	19.52	24.50
Cs	0.89	0.36	9.77	0.23	0.15	0.16	0.33	0.50
Sr	303.86	648.65	4.26	708.05	757.76	822.60	756.84	678.68
Sc	4.26	3.56	5.09	35.56	31.52	27.42	23.49	17.86
Zr	452.85	445.82	84.43	127.60	106.70	133.62	208.16	246.17

Table 1.1: Continued

Sample ID	03HSF-41	12PSF-42	12PSF-43	12PSF-45	12PSF-47	12PSF-49	12PSF-51	12PSF-52
Lat	35.2140	35.3007	35.3291	35.4273	35.4015	35.4726	35.5308	35.4266
Long	111.4286	111.3401	111.2631	111.2006	111.3448	111.3670	111.4036	111.5488
Unit	Mono							
SiO ₂	47.93	51.87	47.52	45.30	49.09	46.81	47.84	60.50
TiO ₂	2.28	1.64	1.58	2.43	1.79	2.03	1.48	1.19
Al ₂ O ₃	16.55	18.08	15.50	14.74	16.40	16.18	15.97	16.29
FeO _T	11.34	9.05	10.39	11.39	10.41	11.17	9.98	6.43
MnO	0.17	0.15	0.18	0.18	0.16	0.17	0.18	0.13
MgO	7.29	5.07	9.03	9.12	6.95	7.78	7.18	1.91
CaO	9.96	8.24	11.12	11.17	9.62	9.76	10.66	4.04
Na ₂ O	3.62	3.79	2.91	3.39	3.32	3.15	3.12	4.61
K ₂ O	0.99	1.49	0.76	1.17	0.99	0.95	0.91	2.88
P ₂ O ₅	0.61	0.59	0.64	0.61	0.42	0.41	0.79	0.43
Sum	100.76	99.96	99.62	99.50	99.17	98.41	98.11	98.41
LOI	-0.50	0.40	0.21	-0.08	0.08	0.81	0.54	0.74
Mg#	53.41	49.99	60.77	58.81	54.34	55.38	56.17	34.60
Ni	91.28	33.17	130.87	141.83	92.23	116.23	68.23	2.79
Cr	189.95	17.13	303.88	324.10	217.63	192.93	97.81	2.69
V	234.18	189.94	241.43	247.41	221.81	212.05	231.47	53.78
Ga	20.24	22.41	15.74	19.32	19.22	19.32	18.23	17.53
Cu	68.31	43.43	72.01	65.44	71.71	60.36	85.56	4.88
Zn	98.16	95.12	94.92	101.99	90.74	92.73	88.74	75.60
La	41.18	40.48	48.05	37.20	29.51	24.84	78.31	51.60
Ce	78.60	78.29	91.92	75.52	56.58	51.06	149.68	94.44
Pr	9.31	9.20	10.78	9.37	6.82	6.47	16.08	10.76
Nd	36.72	35.21	41.11	37.65	27.10	26.67	58.18	39.38
Sm	7.25	6.58	7.53	7.95	5.58	5.96	9.33	7.53
Eu	2.30	1.99	2.28	2.50	1.83	1.97	2.53	1.98
Gd	6.14	5.37	6.13	6.72	5.19	5.56	6.69	6.38
Tb	0.91	0.79	0.88	0.97	0.78	0.87	0.92	0.99
Dy	5.09	4.46	4.86	5.28	4.42	5.01	4.99	5.61
Ho	0.97	0.85	0.91	0.97	0.86	0.97	0.95	1.09
Er	2.39	2.13	2.34	2.43	2.25	2.46	2.37	2.89
Tm	0.31	0.29	0.33	0.32	0.31	0.34	0.33	0.41
Yb	1.87	1.81	1.97	1.89	1.78	2.01	1.95	2.58
Lu	0.29	0.27	0.30	0.28	0.28	0.32	0.30	0.40
Ba	593.57	954.91	787.19	564.36	587.44	446.41	1070.62	936.60
Th	5.17	4.43	5.68	4.01	3.32	2.59	10.93	8.57
Nb	35.16	31.23	35.81	44.06	27.53	28.62	47.94	42.66
Y	23.66	21.06	23.05	23.83	21.45	24.01	23.33	28.12
Hf	3.79	3.99	3.37	4.63	3.30	3.95	3.69	5.99
Ta	1.93	1.80	1.89	2.76	1.54	1.78	2.26	2.90
U	1.14	1.27	1.44	1.52	0.97	0.78	3.14	2.85
Pb	4.56	7.20	5.46	3.88	5.09	2.64	7.79	13.43
Rb	12.85	14.11	8.72	15.46	11.37	11.15	9.83	37.71
Cs	0.16	0.31	0.25	0.24	0.12	0.11	0.30	0.80
Sr	811.99	887.80	842.98	838.23	688.31	645.13	930.30	560.63
Sc	23.84	17.85	30.56	27.32	25.10	25.17	29.96	7.96
Zr	164.29	169.12	143.78	199.16	139.51	168.81	159.91	245.03

Table 1.1: Continued

Sample ID	12PSF-56	12PSF-57	12PSF-59	12PSF-62	12PSF-65	12PSF-66	12PSF-68	12PSF-70
Lat	35.4714	35.6050	35.6991	35.5766	35.5410	35.5408	35.6162	35.5567
Long	111.5261	111.6092	111.6209	111.6865	111.7381	111.7113	111.8577	111.8237
Unit	Mono							
SiO ₂	56.15	46.27	46.90	53.67	46.74	52.89	49.73	49.11
TiO ₂	1.44	1.51	2.00	1.49	2.03	1.38	2.18	2.46
Al ₂ O ₃	16.81	12.87	14.78	16.31	16.73	14.89	16.91	16.78
FeO _T	8.12	9.65	10.35	8.77	10.94	8.61	11.60	12.57
MnO	0.16	0.17	0.17	0.16	0.18	0.15	0.21	0.21
MgO	2.49	11.35	6.98	5.10	7.46	7.44	5.39	4.58
CaO	5.18	12.94	10.53	7.58	10.71	8.88	8.10	6.83
Na ₂ O	5.33	2.33	3.37	4.02	3.46	3.58	4.09	4.40
K ₂ O	2.14	0.71	1.23	1.66	0.98	1.60	1.38	1.55
P ₂ O ₅	0.85	0.63	0.79	0.50	0.77	0.47	0.87	1.12
Sum	98.67	98.43	97.11	99.25	100.00	99.89	100.45	99.61
LOI	0.77	1.07	1.98	0.11	0.08	0.17	-0.30	-0.10
Mg#	35.34	67.72	54.59	50.88	54.86	60.63	45.28	39.37
Ni	1.89	195.32	136.45	49.60	77.29	130.87	48.80	36.45
Cr	0.50	602.98	301.39	72.01	82.37	433.26	82.47	22.91
V	43.72	257.47	191.43	159.16	243.12	182.07	163.05	110.36
Ga	18.03	15.14	19.62	19.52	20.82	18.92	19.52	20.22
Cu	8.86	103.48	55.48	52.99	78.29	67.33	33.57	25.10
Zn	88.15	78.19	121.21	93.33	96.61	86.35	105.28	118.32
La	55.51	43.30	41.59	49.72	59.58	44.86	32.87	45.19
Ce	112.71	85.65	89.47	91.84	117.85	85.32	66.22	94.15
Pr	13.56	10.40	11.38	10.54	13.36	9.86	8.41	12.32
Nd	53.45	40.61	46.08	39.24	50.70	36.80	35.36	51.85
Sm	10.24	7.52	9.22	7.37	9.01	6.91	7.62	11.03
Eu	3.02	2.15	2.75	2.22	2.67	2.01	3.26	3.59
Gd	8.32	5.75	7.59	6.12	6.98	5.62	6.96	9.90
Tb	1.14	0.81	1.06	0.90	0.99	0.84	1.03	1.46
Dy	6.24	4.37	5.74	4.98	5.25	4.62	5.65	7.86
Ho	1.17	0.81	1.03	0.95	0.98	0.88	1.05	1.49
Er	2.96	2.00	2.42	2.44	2.41	2.22	2.61	3.65
Tm	0.42	0.27	0.32	0.34	0.33	0.31	0.34	0.47
Yb	2.49	1.61	1.84	2.02	1.94	1.89	2.00	2.81
Lu	0.38	0.24	0.27	0.33	0.30	0.30	0.31	0.43
Ba	1008.85	840.85	604.87	1007.14	903.36	854.56	1209.74	772.52
Th	5.05	5.44	2.89	6.35	7.47	6.31	3.17	3.11
Nb	38.56	37.26	35.22	37.00	46.20	39.12	29.19	36.01
Y	30.19	20.07	25.56	24.08	24.49	22.20	25.97	36.59
Hf	5.68	2.96	4.95	4.35	3.83	4.71	3.66	5.09
Ta	2.33	2.00	2.04	2.04	2.50	2.39	1.81	2.19
U	1.66	1.46	0.80	1.90	1.91	1.76	0.37	0.39
Pb	8.05	4.52	4.84	9.62	5.52	7.67	4.14	4.97
Rb	25.25	9.17	14.12	19.50	11.73	20.53	15.23	14.58
Cs	0.46	0.32	0.12	0.42	0.26	0.28	0.06	0.06
Sr	1023.70	704.11	763.37	808.82	1034.89	612.73	733.21	772.74
Sc	8.06	35.73	20.40	19.91	25.97	24.82	20.71	15.60
Zr	253.77	123.73	223.82	186.40	166.92	206.50	158.05	222.97

Unit: Mono=monogenetic; SF Mtn=SF Mountain. Major elements in wt%; trace elements in ppm.

Table 1.2: Isotopic data.

Sample ID	03HSF-1	03HSF-2	03HSF-3	03HSF-4	03HSF-5	03HSF-6	03HSF-7
$^{87}\text{Sr}/^{86}\text{Sr}$	0.703070	0.703240	0.703200	0.703163	0.704265	0.703204	0.703188
\pm	0.000006	0.000008	0.000004	0.000008	0.000007	0.000005	0.000008
$^{143}\text{Nd}/^{144}\text{Nd}$	0.512075	0.512632	0.512628	0.512554	0.512457	0.512583	0.512578
\pm	0.000004	0.000006	0.000007	0.000006	0.000002	0.000008	0.000001
ϵ_{Nd}	-10.97	-0.13	-0.19	-1.64	-3.53	-1.08	-1.18
\pm	0.08	0.12	0.13	0.12	0.04	0.15	0.01
$^{206}\text{Pb}/^{204}\text{Pb}$	17.4078		18.0256			17.5297	
\pm	0.0040		0.0013			0.0010	
$^{207}\text{Pb}/^{204}\text{Pb}$	15.4935		15.4935			15.4551	
\pm	0.0011		0.0013			0.0009	
$^{208}\text{Pb}/^{204}\text{Pb}$	37.1930		37.7462			37.0077	
\pm	0.0048		0.0029			0.0019	

Sample ID	03HSF-8	03HSF-9	03HSF-10	03HSF-11	03HSF-12	03HSF-13	03HSF-14
$^{87}\text{Sr}/^{86}\text{Sr}$	0.703237	0.702936	0.703242	0.703151	0.703569	0.703264	0.703296
\pm	0.000007	0.000008	0.000006	0.000008	0.000008	0.000008	0.000006
$^{143}\text{Nd}/^{144}\text{Nd}$	0.512553	0.512704	0.512630	0.512627	0.512757	0.512568	0.512597
\pm	0.000012	0.000020	0.000006	0.000023	0.000006	0.000010	0.000006
ϵ_{Nd}	-1.65	1.30	-0.16	-0.21	2.32	-1.36	-0.79
\pm	0.23	0.40	0.12	0.45	0.12	0.19	0.11
$^{206}\text{Pb}/^{204}\text{Pb}$		17.9659	17.6099		18.5593		17.8125
\pm		0.0015	0.0013		0.0013		0.0011
$^{207}\text{Pb}/^{204}\text{Pb}$		15.4881	15.4550		15.5503		15.4695
\pm		0.0011	0.0014		0.0011		0.0011
$^{208}\text{Pb}/^{204}\text{Pb}$		37.4994	37.0053		38.3665		37.2936
\pm		0.0027	0.0029		0.0028		0.0025

Sample ID	03HSF-15	03HSF-16	03HSF-17	03HSF-18	03HSF-19	03HSF-20	03HSF-21
$^{87}\text{Sr}/^{86}\text{Sr}$	0.703619	0.703053	0.704259	0.703249	0.703684	0.703246	0.703589
\pm	0.000006	0.000008	0.000007	0.000005	0.000007	0.000007	0.000005
$^{143}\text{Nd}/^{144}\text{Nd}$	0.512577	0.512664	0.512666	0.512673	0.512635	0.512609	0.512511
\pm	0.000011	0.000012	0.000006	0.000011	0.000022	0.000004	0.000006
ϵ_{Nd}	-1.20	0.51	0.56	0.69	-0.05	-0.57	-2.48
\pm	0.22	0.24	0.11	0.22	0.42	0.08	0.13
$^{206}\text{Pb}/^{204}\text{Pb}$		18.1274					17.6252
\pm		0.0008					0.0009
$^{207}\text{Pb}/^{204}\text{Pb}$		15.5020					15.4716
\pm		0.0009					0.0008
$^{208}\text{Pb}/^{204}\text{Pb}$		37.7802					36.9778
\pm		0.0020					0.0021

Table 1.2: Continued

Sample ID	12PSF-43	12PSF-45	12PSF-47	12PSF-49	12PSF-51	12PSF-52	12PSF-56
$^{87}\text{Sr}/^{86}\text{Sr}$	0.703690	0.703843	0.703620	0.703368	0.704251	0.703606	0.703319
\pm	0.000008	0.000007	0.000008	0.000006	0.000006	0.000005	0.000005
$^{143}\text{Nd}/^{144}\text{Nd}$	0.512532	0.512802	0.512667	0.512744	0.512662	0.512591	0.512385
\pm	0.000005	0.000018	0.000006	0.000006	0.000005	0.000012	0.000004
ϵ_{Nd}	-2.08	3.21	0.56	2.06	0.46	-0.91	-4.93
\pm	0.10	0.35	0.11	0.11	0.10	0.23	0.08
$^{206}\text{Pb}/^{204}\text{Pb}$	18.3291	18.6828	18.0871	18.3297	18.5849	17.9220	17.4529
\pm	0.0026	0.0007	0.0008	0.0008	0.0011	0.0010	0.0015
$^{207}\text{Pb}/^{204}\text{Pb}$	15.5382	15.5666	15.5131	15.5235	15.5699	15.4954	15.4481
\pm	0.0010	0.0005	0.0006	0.0008	0.0008	0.0007	0.0013
$^{208}\text{Pb}/^{204}\text{Pb}$	38.1728	38.3611	37.6310	37.9915	38.2858	37.2957	37.1983
\pm	0.0023	0.0015	0.0016	0.0019	0.0019	0.0018	0.0031

Sample ID	12PSF-57	12PSF-59	12PSF-62	12PSF-65	12PSF-66	12PSF-68	12PSF-70
$^{87}\text{Sr}/^{86}\text{Sr}$	0.704198	0.703218	0.703677	0.703346		0.703793	0.703374
\pm	0.000006	0.000008	0.000005	0.000008		0.000008	0.000006
$^{143}\text{Nd}/^{144}\text{Nd}$	0.512670	0.512445	0.512469	0.512636	0.512596	0.512697	0.512568
\pm	0.000003	0.000003	0.000015	0.000006	0.000007	0.000003	0.000003
ϵ_{Nd}	0.63	-3.77	-3.29	-0.05	-0.81	1.16	-1.36
\pm	0.07	0.05	0.30	0.11	0.14	0.06	0.06
$^{206}\text{Pb}/^{204}\text{Pb}$	18.7025	17.5860	17.9658	18.5777	17.9230	18.3350	17.8101
\pm	0.0012	0.0009	0.0011	0.0015	0.0010	0.0011	0.0013
$^{207}\text{Pb}/^{204}\text{Pb}$	15.5716	15.4537	15.4976	15.5565	15.4970	15.5299	15.4795
\pm	0.0011	0.0008	0.0010	0.0011	0.0008	0.0009	0.0014
$^{208}\text{Pb}/^{204}\text{Pb}$	38.4832	37.0682	37.5848	38.3442	37.5003	37.7417	37.3067
\pm	0.0026	0.0019	0.0020	0.0027	0.0018	0.0022	0.0031

Table 1.3: Major and trace element inputs for AFC modeling

	^a Primitive	^b Granulite assimilant			
		Parent	F = 0.2	F = 0.4	F = 0.6
SiO ₂	47.89	50.86	52.37	52.21	52.51
TiO ₂	1.34	0.72	1.58	1.37	1.07
Al ₂ O ₃	13.17	17.62	14.82	15.42	16.28
Fe ₂ O ₃	4.28	2.92	4.93	4.6	3.68
FeO	5.56	5.03	10.13	8.72	7.06
MgO	11.79	5.42	3.34	4.34	4.96
CaO	11.48	11.93	5.5	7.17	9.02
Na ₂ O	2.34	3.57	5.41	4.95	4.53
K ₂ O	0.81	0.44	1.36	0.94	0.7
H ₂ O	0.55	0.1	0.51	0.25	0.17
CO ₂	0.14	0.01	0.05	0.03	0.02
Ni	195.32	123.33	36.12	42.94	54.66
Cr	602.98	266	56	220.57	233.37
V	257.47	177.67	274.19	238.62	213.85
Ga	15.14	25	48.88	42.04	34.23
Cu	103.48	18	55.71	36.39	27.13
Zn	78.19	51.67	258.36	129.17	86.12
La	43.3	20.2	59.57	39.98	30.15
Ce	85.65	46.05	142.62	93.37	69.56
Pr	10.4	6.6	20.17	13.29	9.93
Nd	40.61	27.04	80.86	53.82	40.46
Sm	7.52	5.74	16.98	11.36	8.56
Eu	2.15	1.94	3.07	2.67	2.37
Gd	5.75	4.69	14.12	9.36	7.02
Tb	0.81	0.59	1.77	1.18	0.88
Dy	4.37	3.07	9.1	6.08	4.58
Ho	0.81	0.56	1.71	1.13	0.84
Er	2	1.44	4.49	2.92	2.18
Tm	0.27	0.2	0.63	0.41	0.3
Yb	1.61	1.27	4.1	2.62	1.94
Lu	0.24	0.19	0.62	0.39	0.29
Ba	840.85	370.67	1066.79	724.91	550.02
Th	5.44	1.03	4.62	2.47	1.68
Nb	37.26	7.66	36.25	18.75	12.65
Y	20.07	15.67	55.61	33.86	24.41
Hf	2.96	1.03	3.68	2.23	1.61
Ta	2	1.79	8.65	4.42	2.97
U	1.46	0.57	2.29	1.3	0.91
Pb	4.52	5.39	14.8	10.29	7.9
Rb	9.17	2.39	11.18	5.82	3.94
Cs	0.32	0.03	0.14	0.07	0.05
Sr	704.11	1166	1025.88	1052.65	1089.52
Sc	35.73	27.33	71.3	50.53	39.36
Zr	123.73	34.67	145.27	80.69	55.93

Table 1.3: Continued

	^c Upper crust assimilant			
	Parent	F = 0.6	F = 0.8	F = 1.0
SiO ₂	66.23	73.22	68.79	66.23
TiO ₂	0.64	0.78	0.76	0.64
Al ₂ O ₃	15.32	13.11	14.77	15.32
Fe ₂ O ₃	0.84	0.37	0.81	0.84
FeO	4.26	1.63	3.13	4.26
MgO	2.47	0.51	1	2.47
CaO	3.57	2.28	3.01	3.57
Na ₂ O	3.25	2.24	3.09	3.25
K ₂ O	2.78	4.18	3.37	2.78
H ₂ O	1	1.66	1.25	1
CO ₂	0.01	0.02	0.01	0.01
Ni	47	29.01	31.07	47
Cr	92	20.17	58.1	92
V	97	139.04	111.72	97
Ga	17.5	25.56	21.18	17.5
Cu	28	46.67	35	28
Zn	67	111.67	83.75	67
La	31	45.88	37.21	31
Ce	63	96	76.4	63
Pr	7.1	10.96	8.65	7.1
Nd	27	42.19	33.02	27
Sm	4.7	7.44	5.77	4.7
Eu	1	1.24	1.12	1
Gd	4	6.45	4.94	4
Tb	0.7	1.13	0.87	0.7
Dy	3.9	6.31	4.82	3.9
Ho	0.83	1.35	1.03	0.83
Er	2.3	3.74	2.85	2.3
Tm	0.3	0.49	0.37	0.3
Yb	1.96	3.19	2.43	1.96
Lu	0.31	0.51	0.38	0.31
Ba	628	907.46	747.4	628
Th	10.5	17.1	13.03	10.5
Nb	12	19.89	14.97	12
Y	21	34.49	26.12	21
Hf	5.3	8.78	6.61	5.3
Ta	0.9	1.5	1.12	0.9
U	2.7	4.28	3.32	2.7
Pb	17	24.27	20.14	17
Rb	82	134.77	102.03	82
Cs	4.9	8.07	6.1	4.9
^c Sr	320, 65	276, 56	306, 62	320, 65
Sc	14	21.83	16.92	14
Zr	193	318.46	240.2	193

Table 1.4: Isotopic inputs for AFC modeling

	^b Granulite assimilant				
	^a Primitive	Parent	F = 0.2	F = 0.4	F = 0.6
⁸⁷ Sr/ ⁸⁶ Sr	0.703842	0.7027	0.7027	0.7027	0.7027
^d ϵ_{Nd}	3.21	-10, -20	-10, -20	-10, -20	-10, -20
²⁰⁶ Pb/ ²⁰⁴ Pb	18.7099	17	17	17	17
²⁰⁷ Pb/ ²⁰⁴ Pb	15.5752	15.4	15.4	15.4	15.4
²⁰⁸ Pb/ ²⁰⁴ Pb	38.5002	36.3	36.3	36.3	36.3

	^c Upper crust assimilant			
	Parent	F = 0.6	F = 0.8	F = 1.0
^e ⁸⁷ Sr/ ⁸⁶ Sr	0.73, 0.79	0.73, 0.79	0.73, 0.79	0.73, 0.79
ϵ_{Nd}	-10	-10	-10	-10
²⁰⁶ Pb/ ²⁰⁴ Pb	19.3	19.3	19.3	19.3
²⁰⁷ Pb/ ²⁰⁴ Pb	15.76	15.76	15.76	15.76
²⁰⁸ Pb/ ²⁰⁴ Pb	39.8	39.8	39.8	39.8

^aThe primitive magma major element composition is the mean of a subset of USGS data that satisfies: age <1 Ma and 68<Mg#<73. Trace elements, ⁸⁷Sr/⁸⁶Sr, and ϵ_{Nd} , are from sample 12PSF-57; Pb isotopes are from 12PSF-45; both these samples have Mg#>67 and combined ⁸⁷Sr/⁸⁶Sr, ϵ_{Nd} values suggesting near-equilibrium with mantle. I assume an initial temperature of 1370° C (calculated from SFVF geothermometry, geobarometry estimates of 1440° C at 2.55 GPa for primitive SFVF magmas, assuming an adiabatic temperature decrease of ~1.1° C/km to phase 1 pressures).

^bThe phase 1 assimilant is a mafic granulite. Major and trace element abundances were derived by averaging mafic granulite xenolith compositions of W. Chen and Arculus (1995). See main text, section 1.5.4, for discussion of the inferred isotopic values.

^cThe phase 2 assimilant major and trace element composition is the mean upper crust composition of Rudnick and Gao (2003); see main text, section 1.5.4, for discussion of the inferred isotopic values.

^dTwo ϵ_{Nd} compositions were specified for the phase 1 assimilant (models I and II).

^eTwo different ⁸⁷Sr/⁸⁶Sr isotopic compositions and Sr abundances were explored for the phase 2 assimilant (models III and IV).

Chapter 2

U–Th/He dating and $^3\text{He}/^4\text{He}$ of Late Pleistocene submarine tholeiitic basalt from the Hawaii Scientific Drilling Project core (HSDP–2)

2.1 Introduction

There is a growing need for improved geochronology in studies of Quaternary geology, the time period that is most relevant for understanding future environmental change. However, determining the timing of Quaternary events remains a technical challenge. Despite considerable advances in ^{14}C , $^{40}\text{Ar}/^{39}\text{Ar}$, cosmogenic nuclide, and U-series disequilibrium chronologies, no simple method with wide applicability has emerged. Deep submarine mafic volcanics are particularly difficult samples for argon methods due to the deficiency of K-rich phases and the incomplete degassing of mantle Ar with high $^{40}\text{Ar}/^{36}\text{Ar}$.

This chapter focuses on measuring the age of low-K submarine basalts by applying the U–Th/He method to olivine phenocrysts. Although Quaternary chronology has benefited from a recent resurgence in the U–Th/He method as applied to U, Th-rich minerals (see Aciego, Kennedy, DePaolo, Christensen, and Hutcheon, 2003; and reviews by Farley, Kohn, and Pillans, 2002; Reiners and Ehlers, 2005), olivine phenocrysts introduce unique technical issues that must be addressed:

1. The volcanic phenocrysts are U, Th-poor, with concentrations on the order of a few to tens of ppbs.
2. The U, Th-poor phenocrysts are embedded in a U, Th-rich (\sim ppms) glass matrix.
3. Magmatic helium trapped in fluid and melt inclusions dominates the helium inventory in the phenocrysts.

Despite the problems listed above, previous work has shown that the method can theoretically be used to date basalt as young as a few thousand years and as old as several million years, and hence could span the gaps often encountered with existing methods. U–Th/He and cosmogenic ^3He exposure geochronologies have been successfully applied simultaneously to olivine phenocrysts from late Quaternary basalts with crystallization ages ranging from 86 to 3400 ka and surface exposure ages of 19 to 48 ka (Aciego, DePaolo, et al., 2007). The U–Th/He technique was also applied in conjunction with $^{40}\text{Ar}/^{39}\text{Ar}$ on 100–400 ka, sub-aerial, post-shield Mauna Kea and Kohala lavas of Hawaii (Aciego, Jourdan, et al., 2010). In the latter study, the two techniques produced similar ages for four analyzed samples but discrepant ages for three (only one of which showed evidence of disturbed Ar systematics), highlighting the need for further refinement of methods.

In order to expand the utility of the U–Th/He method to include partially degassed, submarine lavas, provide geochronological constraints on the growth history of Hawaiian volcanoes, and further characterize the He isotope geochemistry of the Hawaiian hot spot, I applied the method to olivine separates from the Hawaii Scientific Drilling Project, phase-2 (HSDP–2) core basalts. Hawaiian lavas have been used to investigate the thermal and geochemical structures in the deep-rooted Hawaiian plume and its source region (Bryce, DePaolo, & Lassiter, 2005); in particular, magmatic $^3\text{He}/^4\text{He}$ ratios from the upper 3100 m of the HSDP–2 core have provided unique constraints on the length-scales of heterogeneities within the Hawaiian source (Kurz, Curtice, Lott, & Solow, 2004). The HSDP–2 core has proven invaluable in refinement of models of Hawaiian volcano and magma genesis, but accurate age dating of lavas is critical to linking geochemical observations to temporal scales and volcano growth models (e.g. DePaolo, Bryce, et al., 2001). Combined analyses of magmatic $^3\text{He}/^4\text{He}$ ratios and radiogenically-produced ^4He can constrain both the temporal evolution and the geochemistry of the Hawaiian source. Ubiquitous olivine–phyric units throughout the core, abundant geochemical data, and limited $^{40}\text{Ar}/^{39}\text{Ar}$ ages (Sharp & Renne, 2004) make HSDP–2 samples excellent candidates for study. With the goals of extending both the U–Th/He method and the magmatic $^3\text{He}/^4\text{He}$ isotopic record of the Mauna Kea volcano, I selected 14 units from the HSDP–2 core for analysis, including 5 units from the deepest (3100–3500 m) core which had not been previously analyzed.

2.2 Procedure

2.2.1 Overview

Figure 2.1 shows a schematic overview of the U–Th/He procedure. Whole rock samples were coarse-crushed with a steel jaw crusher, ground by disc-mill, and sieved to extract 0.8–1.0 mm grain sizes. An olivine-rich fraction was separated magnetically, then hand-picked to yield ~ 2 g olivine phenocrysts that were free of matrix. The phenocrysts – many of which were shards as a result of the treatment – were subsequently physically air-abraded until ~ 1 g material remained (sufficient to remove at least ~ 30 – 50 μm from the surface of the

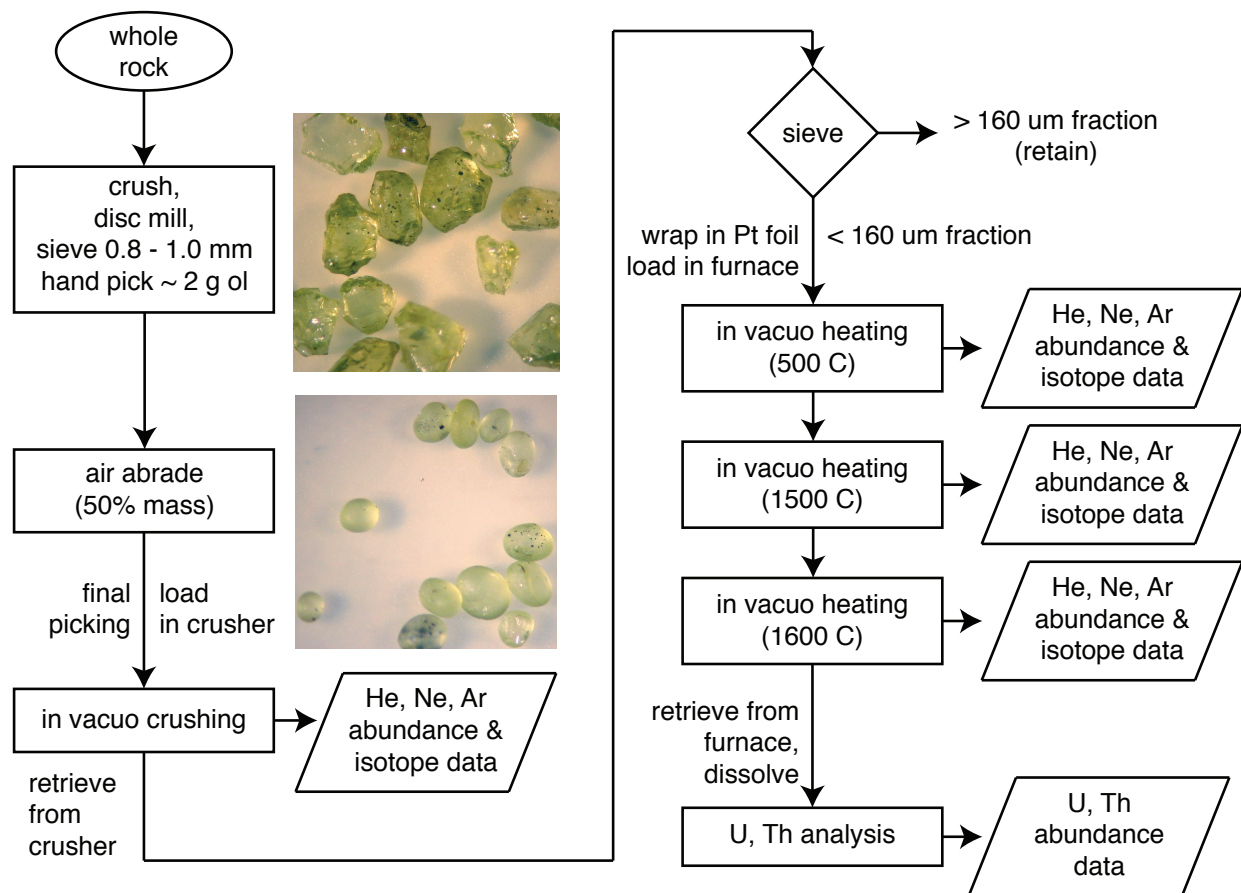


Figure 2.1: Schematic overview of the U-Th/He procedure; see also Aciego, Kennedy, et al. (2003), Aciego (2006).

mineral grains, and thereby eliminate implanted ^4He due to α -recoil from the U, Th-rich basalt matrix). The abraded shards were rinsed sequentially in deionized H_2O , trace grade isopropyl alcohol, and acetone, then subjected to a final scan via binocular microscope to ensure no matrix adhered to the abraded olivine grains.

The prepared olivine sample was loaded into magnetically-operated crushers and magmatic gas was extracted and analyzed by crushing *in vacuo*. Following the crushing step, the samples were recovered from the crushers, sieved, and the $<160 \mu\text{m}$ fraction (~ 0.20 – 0.40 g) was wrapped in platinum foil and loaded into a resistance furnace that allows for blank data collection and sample recovery. Most of any remaining trapped magmatic gas was removed by a single low-temperature heating step ($\sim 500^\circ\text{C}$). Lattice-bound gas, including radiogenic ^4He , was extracted by high-temperature heating to $\sim 1500^\circ\text{C}$, and total extraction was checked by a secondary $\sim 1600^\circ\text{C}$ heating step. Following heating, samples were recovered from the furnaces and digested in acid following the procedures described in

Aciego, Jourdan, et al. (2010) for U, Th analysis.

2.2.2 U, Th measurements of low U, Th content samples

Olivines from relatively low-K tholeiitic basalts are challenging minerals to date by U–Th/He. They have low U, Th contents (generally orders of magnitude less than in zircon, apatite, or volcanic garnet; e.g. Aciego, Kennedy, et al., 2003), and, because U and Th are incompatible in olivine, the elements are preferentially housed in inclusions or crystal defects. Thus U and Th concentrations are highly variable, even between separate olivine splits from the same whole rock (hence the need to recover samples after each analytical step).

The HSDP olivines we studied from tholeiitic lavas have even lower U, Th concentrations than those found in post-shield alkalic Hawaiian lavas or Snake River Plain basalts. Due to low U, Th concentrations, isotopic measurements could not always be made to the same precision obtained by Aciego, Jourdan, et al. (2010) or Aciego, DePaolo, et al. (2007). Elemental concentrations of U and Th were measured either by isotope dilution or ICP-MS at the Center for Isotope Geochemistry at the Lawrence Berkeley National Laboratory.

2.2.3 He isotope analytical challenges

2.2.3.1 Analyzing samples with near-blank abundances of ^4He

The low U, Th contents and young ages of the studied basalts produce small amounts of radiogenic ^4He , which makes accurate determination of ^4He abundances challenging. Gases were measured by single-collection on a dual-collector spectrometer, where the central collector could be switched between a Faraday cup and an electron multiplier operated in ion-counting mode. All ^3He was measured on the multiplier, and typically, ^4He for most samples was as well (exceptions include standards and some crushed runs with sufficiently large amounts of gas). In many cases, $^3\text{He}/^4\text{He}$ ratios have large uncertainties because the ^4He abundances are barely above background (this is a particular problem for heating steps). Application of the technique is limited by the ^4He blank (Figure 2.2).

The uncertainties of blank-subtracted ^4He abundances and $^3\text{He}/^4\text{He}$ ratios could be reduced or better quantified by more stringent blank analyses. During the course of this study, following sample loading, extraction line bake, and cooling, single blanks were run (one for each crusher and one for each furnace) prior to analyzing the sample. Because the vacuum extraction line continued to desorb gas following bake for up to several days, a single, early measurement could result in an anomalously high blank (compare the ^4He blank for sample 02AMK12B with others in Figure 2.2a). In future work it would be worthwhile to modify this procedure so that blanks are run following bake until the blank abundances plateau; then several replicate plateau measurements should be averaged. At the cost of time, this will provide both the lowest realistic blank and an error for the blank, which can be propagated through the ^4He abundance calculation. This approach may be necessary to extend the technique to low- ^4He abundance samples.

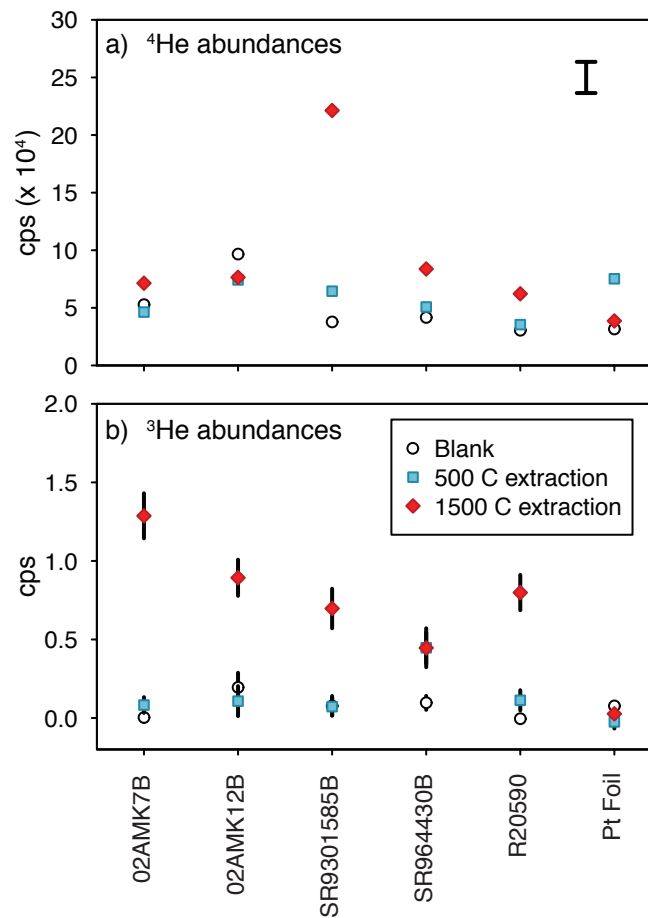


Figure 2.2: Comparison between hot (1500° C) furnace blanks (open circles), 500° C extractions (blue squares), and 1500° C extractions (red diamonds). In (a), individual errors calculated from regression to $t=0$ are smaller than the symbols. A better indicator of uncertainty is given by the black error bar, which shows $\pm 1\sigma$ for $n=12$ air pipette standards. In (b), errors from the regressions ($\pm 1\sigma$) are shown for each assay. The ^4He signal from extractions is typically close to blank, while ^3He is clearly resolvable and significantly higher than blank.

2.2.3.2 Spectrometry at low He abundances

In addition to challenges associated with measuring near-blank ^4He abundances, there are spectrometric issues related to low-He-abundance samples that required procedure refinement. When purified He gas (desorbed from a cold head) is analyzed, ^3He and ^4He are measured by alternating between one 5-second integration on ^4He and five 15-second integrations on ^3He (with bracketing half-mass zeroes measured each cycle). This cycle is repeated 10 times, resulting in 20 ^4He and 50 ^3He measurements, and the overall measurement requires ~ 60 minutes to complete. There is gradual pump-out over the course of the measurement, which ideally produces monotonically decreasing count rates throughout the data collection time. For large ^4He abundances (measureable on a Faraday cup), this pump-out is linear, and ^4He abundances can be calculated by linear regression through all the ^4He data to time $t=0$ (when the gas was let into the spectrometer source). At low abundances, however, the ^4He concentration changes non-linearly with time: there is initial ingrowth followed by linear pump-out for the remainder of the run (Figure 2.3a). This behavior was ubiquitous in HSDP-2 samples.

The exact cause of the initial ingrowth is not understood at present, but the behavior is time-dependent and difficult to quantify or model, given the low sampling frequency of the ^4He data. However, a refined procedure yields reproducible behavior: the He split is admitted to the spectrometer, and after 3 minutes, the mass spec inlet valve is closed. The sample is then allowed to continue to equilibrate with the mass spec volume for an additional 4 minutes before the run is started. This results in a reproducible characteristic curve of growth (for 2 blocks) followed by pump out for the remainder of the analysis. The 8 block remainder can be fit linearly, and regression is used to determine the initial ^4He cps and concentration (Figure 2.3a). As the pump-out trends are absent in the ^3He measurements (or not resolvable in the noise), all ^3He data are used (Figure 2.3b).

2.3 He data

He data for both the *in vacuo* crushing step and the heating steps are presented in Table 2.1 and Figure 2.4. Previously reported $^3\text{He}/^4\text{He}$ ratios of magmatic gas from samples of the HSDP core, extracted by *in vacuo* crushing of HSDP olivines, clinopyroxenes, and glass, range from 6 to 24.7 R/R_A (Kurz et al., 2004). In cases where duplicate data are available, results from crush extractions in this study match those of previous studies. The new crush data have $^3\text{He}/^4\text{He}$ ratios that extend the range for the HSDP-2 core down to $\text{R}/\text{R}_A = 4.40$, but otherwise largely overlap with the range expected for Hawaiian lavas.

In all cases, gas released in heating steps is isotopically enriched in ^3He relative to the results from the crushing step (compare red diamonds with other HSDP-2 data in Figure 2.4). These results are similar to those observed for cosmogenically-enriched samples (e.g. Kurz, 1986a; Gayler, Mukhopadhyay, & Meade, 2008; Aciego, DePaolo, et al., 2007; Aciego, Jourdan, et al., 2010), but contrary to $^3\text{He}/^4\text{He}$ results from heating HSDP-2 glasses (Kurz et al.,

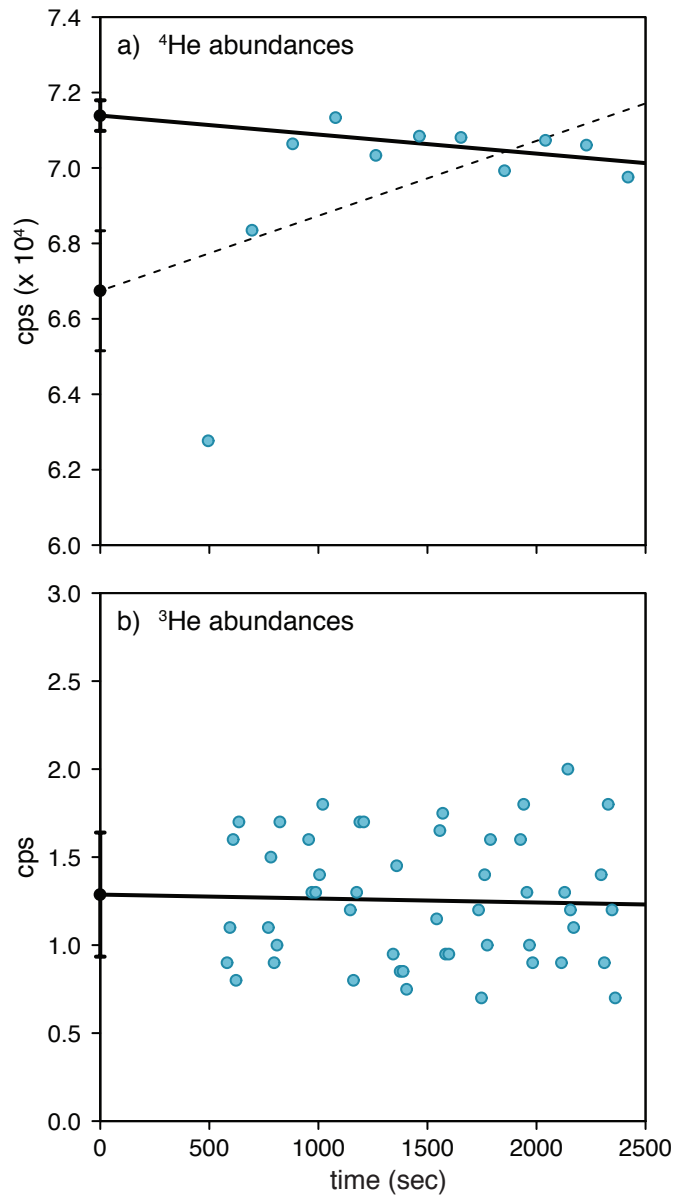


Figure 2.3: An example of the spectrometry data (sample 02AMK7B, 1500° C extraction). (a) 4He data shows regression for blocks 2-8, excluding the first two data points in the sequence (our preferred method; solid line) and regression through full data (dashed line). (b) 3He data do not exhibit the same pattern, and all data are used in the regression.

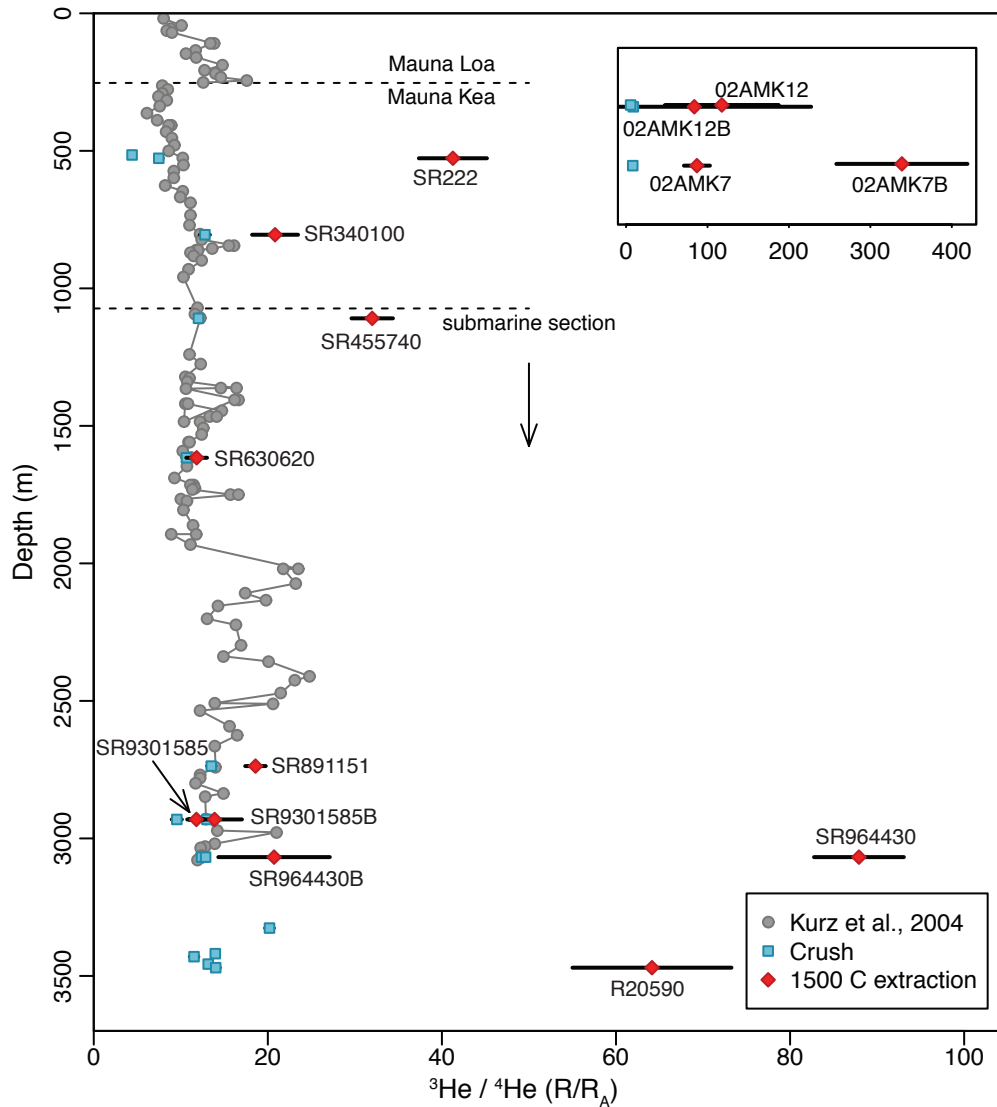


Figure 2.4: $^3He/^4He$ (as R/R_A) for Hawaiian lavas; blue squares are crushing results, labeled red diamonds are $1500^\circ C$ extraction results (2σ errors are plotted, and are generally smaller than symbols for the crushed extractions). Gray data for the HSDP-2 core are from Kurz et al. (2004). No previously published data exist for sample SR18059A2 at depth 515 m ($R/R_A = 4.4$) or for any samples at depths >3100 m. Inset plot shows R/R_A for replicates of two post-shield lavas (data are from this study and Aciego, Jourdan, et al., 2010).

2004). I refer to this excess ^3He as “orphaned ^3He ” (discussed further in section 2.6).

The complexities described in section 2.2.3.2 were first recognized during the initial analytical campaign conducted prior to 2009. At the time it was not known whether the orphaned ^3He was a related procedural artifact, and a second campaign was carried out to re-analyze two post-shield Hawaiian lavas (02AMK7B and 02AMK12B, which were expected to have abundant lattice ^3He due to cosmogenic ingrowth), two deep HSDP-2 samples (SR964430B and SR9301585B, which were not expected to have excess ^3He), and one new sample from the lowermost, phase-2 core (R20590, which has especially high olivine content, also not expected to have ^3He). Between the two campaigns, extraction line components (including a number of getters) were replaced, and the new analyses were conducted using refined procedures. Over a 5-year time period with 3 different analysts (Aciego, Kennedy, Peterson) on different olivine splits separated from common whole rocks, all replicate analyses have shown excess ^3He in high-temperature heating steps. In two cases, the $^3\text{He}/^4\text{He}$ ratios of the replicated 1500° C extractions are drastically different from one another (compare the SR964430 and 02AMK7 replicates).

2.4 Magmatic $^3\text{He}/^4\text{He}$ of the deep core

I analyzed 5 samples from the lowermost HSDP-2 core for which no data had previously been collected. The *in vacuo* crushing of these samples extends the magmatic $^3\text{He}/^4\text{He}$ record from 3098 m to 3470 m in the HSDP-2 core. The $^3\text{He}/^4\text{He}$ ratios in four of these samples range from 11.52 to 14.01 R/R_A, while one sample (R13010) has much higher $^3\text{He}/^4\text{He} = 20.19$ R/R_A. The new results suggest that the core from ~3100–3500 m is similar to that from ~2500–3100 m: it is likely characterized by a baseline $^3\text{He}/^4\text{He}$ value of 12–14 R/R_A, with occasional deviations from this baseline, such as that observed in sample R13010.

Kurz et al. (2004) noted that excursions of high $^3\text{He}/^4\text{He}$ ratios correlate with other isotopic and trace element geochemical indicators, and attributed them to pulses of magma derived from the center of the upwelling Hawaiian hotspot, possibly as a consequence of melting spatially limited heterogeneities in the plume core. The highest $^3\text{He}/^4\text{He}$ ratios are observed in the 2000–2500 m section of the HSDP core, suggesting that these lavas were generated when Mauna Kea was closest to the center of the Hawaiian plume. Although the new data from the lowermost core lack the higher spatial sampling frequency of the shallower core, their modest $^3\text{He}/^4\text{He}$ ratios and potentially infrequent excursions suggest that the deepest lithologies in the HSDP-2 core may be old enough that Mauna Kea had not yet drifted to where it was closest to the plume center.

2.5 Provisional U–Th/He Ages

2.5.1 Age calculations and analytical concerns

U–Th/He provisional ages were computed using:

$$^4\text{He} = (8^{238}\text{U}\lambda_{238} + 7^{235}\text{U}\lambda_{235} + 6^{232}\text{Th}\lambda_{232})t \quad (2.1)$$

(Equation 1 of Farley et al., 2002), where ^{238}U , ^{235}U , and ^{232}Th are calculated from the U and Th elemental abundances assuming secular equilibrium in the decay chain, and the ^4He refers to only radiogenic gas. Farley et al. (2002) have suggested that in young samples, U–Th/He zircon ages computed assuming secular equilibrium may be underestimated by up to several tens of % due to preferential partitioning of U relative to Th. However, U and Th are not as heavily fractionated during olivine growth; in post-shield alkalic basalts, the effects were shown to be smaller, 10% at most (Aciego, Jourdan, et al., 2010), and Hawaiian tholeiitic basalts generally show only small departures (<5%) from secular equilibrium (e.g. Sims et al., 1999). Errors due to approximation of secular equilibrium in the computed ages of HSDP–2 lavas are likely to be of similar magnitudes (and will approach zero as samples age to greater than several hundreds of ka); thus any errors due to the assumption of secular equilibrium are likely to be negligible in comparison to analytical uncertainties.

More difficult to satisfy is the requirement in Equation 2.1 that ^4He is entirely radiogenic. In the “perfect” case, all magmatic gas would be released by crushing and 500° C heating, leaving only lattice-bound, radiogenic ^4He for extraction during high-temperature heating; such a case would have a $^3\text{He}/^4\text{He}$ ratio of 0 R/R_A measured on gas extracted during 1500° C heating (in the absence of cosmogenic ^3He). In practice, if crushing and 500° C heating does not release all magmatic gas, the heating step will have a $^3\text{He}/^4\text{He}$ ratio >0 R/R_A, but theoretically less than that released in the crushing step. Assuming mass balance, the $^3\text{He}/^4\text{He}$ ratio from the crushing step can be used to correct for any remaining magmatic ^4He in the ~1500° C extraction, yielding accurate determination of radiogenic ^4He concentration, and hence age. In all cases, however, gas released in heating steps is isotopically enriched in orphaned ^3He relative to crush; thus a correction is not possible.

Absent our ability to correct for residual magmatic gas, and assuming all the ^4He released by ~1500° C extraction is radiogenic, ages computed using Equation 2.1 are effectively maxima (hence we term them “provisional”). These ages are generally similar to, or in excess of, respective modeled ages for their depths in the HSDP–2 core. The shallowest sample is younger, while those deeper are older (Figure 2.5; Table 2.2).

The correction for residual magmatic ^4He could be small, potentially negligible; Ar systematics and re-crushing experiments suggest that crushing can effectively remove magmatic gas (Figure 2.6). However, we note that in two cases there are large, systematic discrepancies in calculated ages between the HSDP–2 sets of replicates (SR964430 and SR9301585); if such discrepancies are due to variations in magmatic ^4He removal efficiencies, then a correction must be applied for precision dating. In both cases, the replicate ages are closer to the

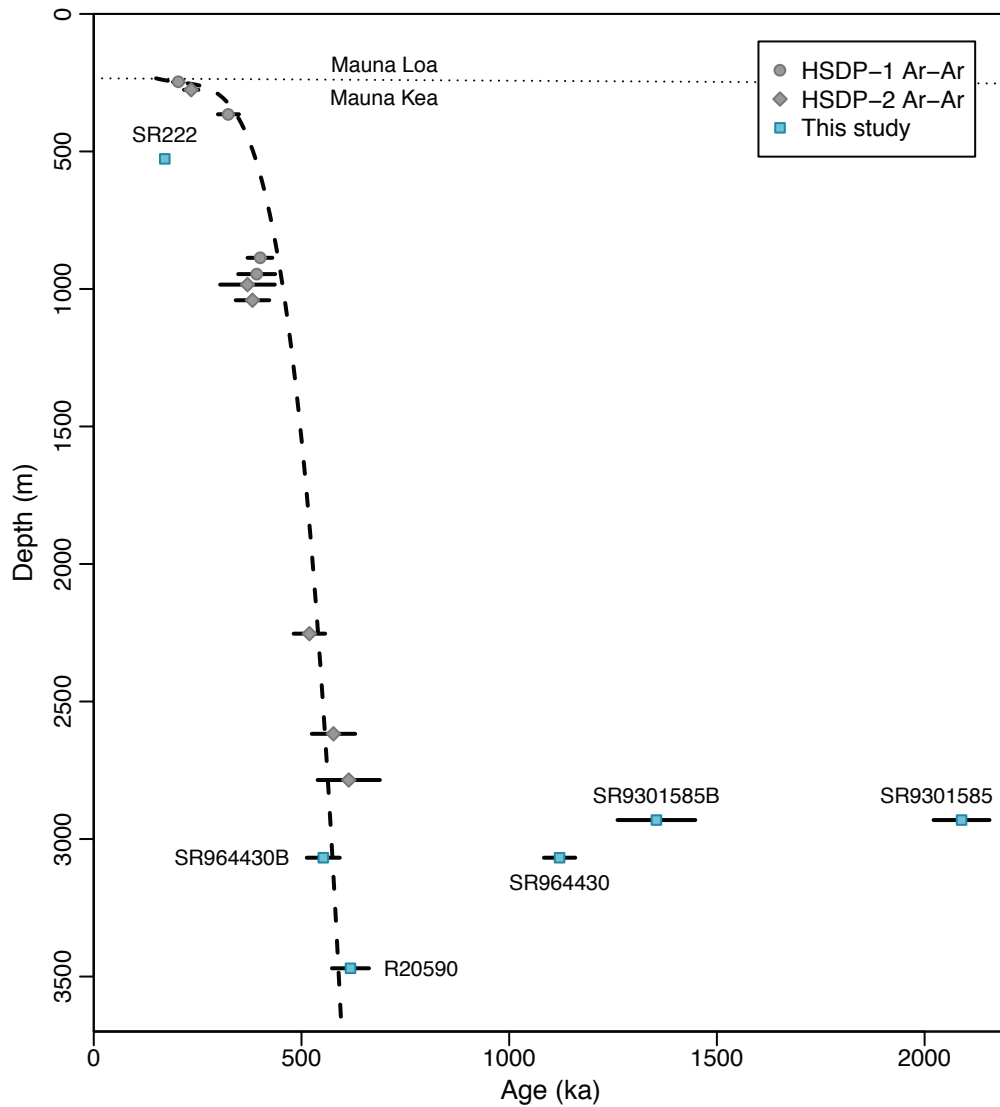


Figure 2.5: HSDP-2 core U-Th/He ages from this study (in blue). Heavy dashed line is the growth model of Bryce et al. (2005), DePaolo and Stolper (1996). $^{40}\text{Ar}/^{39}\text{Ar}$ ages (in gray) are from Sharp and Renne (2004).

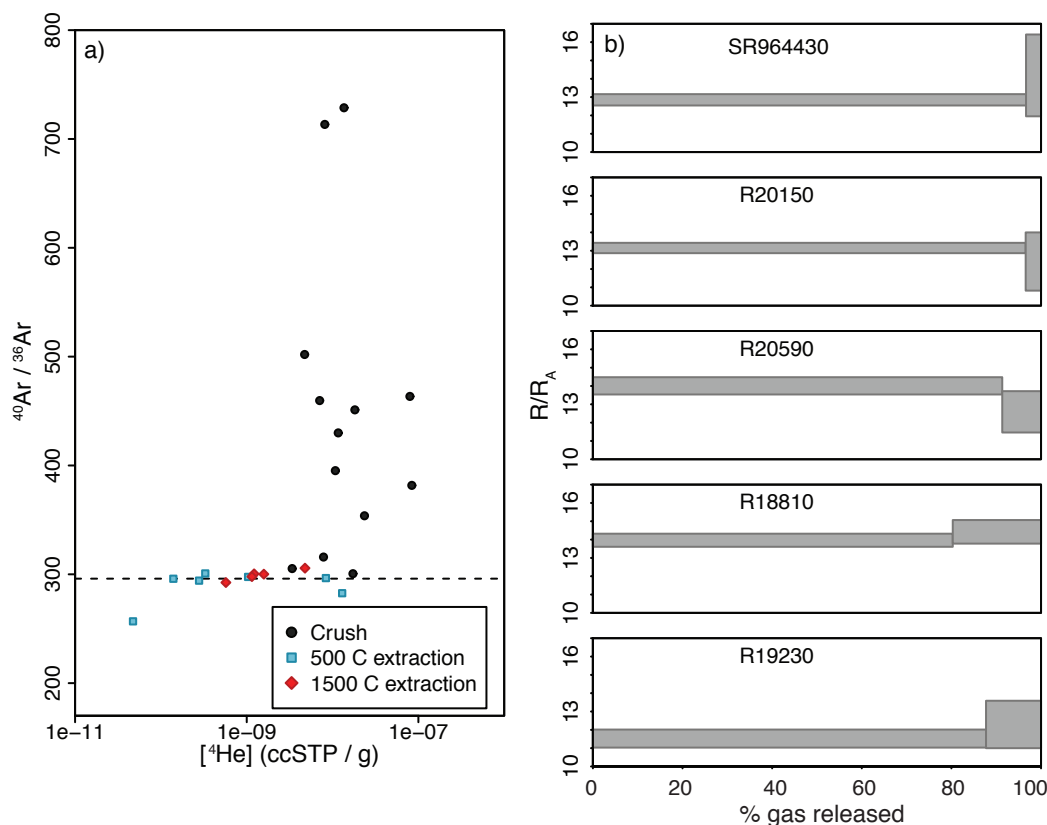


Figure 2.6: Evaluations of crushing efficiency. (a) Excess mantle Ar (high $^{40}\text{Ar}/^{36}\text{Ar} > 295.5$), is present in crush extractions, but absent in subsequent heating steps, indicating efficient removal of mantle-derived magmatic gases by crushing. Ar isotopes are measured on the same splits as He isotopes for each sample. (b) Results of re-crushing in plateau-style diagrams. For these analyses, the samples are crushed twice before retrieval from the crushers; in all cases, the first crush (left boxes) releases the majority of gas from the samples (80-95%).

$^{40}\text{Ar}/^{39}\text{Ar}$ ages and the expected modeled ages; thus sufficiently refined procedures may be able to generate acceptable ages, even for low U, Th, He samples.

2.5.2 Age of the deep section of the HSDP core

Ages were obtained for samples SR222, SR9301585, SR964430, and R20590 (Figure 2.5); sample SR222 is from the shallow core (527 m) and the remainder are from the deeper core, 2931 m or greater. Temporal constraints on the deep core are particularly crucial, as $^{40}\text{Ar}/^{39}\text{Ar}$ ages are lacking at these depths. For two samples (SR9301585, SR9301585B and SR964430, SR964430B), replicates were measured in the second analytical campaign, and in both cases, the replicate ages were significantly younger than the initial measurements. As mentioned, the differences between replicate ages may be due to differences in the amount

of residual magmatic ^4He gas remaining in the samples; however, as the second analytical campaign was conducted specifically to address the analytical and procedural issues described above, the second set of measurements (SR9301585B and SR964430B) are likely closer to the true ages of the units.

Of the deep core samples measured in the second analytical campaign, two (SR964430B and R20590) are consistent with the ages predicted by the lava accumulation rate models (dashed line in Figure 2.5) of Bryce et al. (2005), DePaolo and Stolper (1996). These ages also continue the trend suggested by $^{40}\text{Ar}/^{39}\text{Ar}$ dates in the shallower core. The replicate SR9301585B, at 1354 ka, is significantly older.

Ages for intrusive units could be out of stratigraphic sequence (they can be younger). The unit from which R20590 was subsampled was not mapped as intrusive, but the sample is characterized by a crystalline groundmass, large (up to several mm diameter) olivine phenocrysts, and an absence of glass. It is possible that the older age of SR9301585B is correct, and the younger R20590 is out of sequence. This would also imply that the SR964430B would have to be similarly out of sequence and anomalously young, and would require magma accumulation rates during genesis of the deeper portion of core (>2900 m) to be drastically lower than those for the remainder of the Mauna Kea volcano's life. This is unlikely, as the magmatic $^3\text{He}/^4\text{He}$ ratios in the >2900 m core are a continuation of the isotopic signature from about 2500 m down, suggesting roughly similar proximity to the center of the Hawaiian plume (e.g. the volcano was near – but not yet closest to – the center of the plume). If the accumulation model is correct, 500 m of core (from 2000 to 2500 m depth) corresponds to about a 25 kyr span; assuming a 10 cm/yr Pacific plate velocity with respect to the plume, the Mauna Kea volcano would have moved only 2.5 km during this time, a small distance in comparison to the dimensions of the plume.

Therefore, it seems unlikely that R20590 and SR964430B are out of stratigraphic sequence. Rather, both appear to give consistent ages for the deep section of the HSDP-2 core, while SR9301585B is anomalously old. I note that both SR9301585 and the replicate SR9301585B have the highest ^4He abundances of all the 1500° C extractions (and correspondingly low $^3\text{He}/^4\text{He}$ ratios in the same extractions); it may be that excess magmatic ^4He remains in these samples following crushing for which correction is not possible, yielding anomalously old ages.

The ages of R20590 and SR964430B (552 and 618 ka) for the lowermost core are consistent with both the existing $^{40}\text{Ar}/^{39}\text{Ar}$ ages in the shallower core and the accumulation model. The parameterization suggested by Bryce et al. (2005) requires accumulation rates of 15-21 mm/yr in the submarine section of the volcano, slightly lower than the rates of 28-40 mm/yr suggested originally by DePaolo and Stolper (1996) for an off-axis volcano such as Mauna Kea. My new dates support these slightly lower accumulation rates extending an additional 500 - 700 m down into the lowermost, submarine core.

2.6 Sources of orphaned ^3He

2.6.1 Procedurally-induced He fractionation

Significant analytical work was done to attempt to discover the source of the orphaned ^3He . Excess ^3He was not measured during crush and blank analyses. Because the noble gas separation and measurement procedures were identical for blanks, crushing, and heating steps beyond the initial gas extraction mechanism (e.g. crushing versus heating), the ^3He enrichment cannot be caused by common steps of the procedure (such as gas desorption from the cold head, or measurement by the spectrometer). In all cases, crushing blanks, platinum foil blanks, and furnace blanks (which are run hot, at $\sim 1500^\circ\text{C}$) exhibit $^3\text{He}/^4\text{He}$ ratios lower than those from the olivine measurements; blanks have $^3\text{He}/^4\text{He}$ ratios of $R/R_A = \sim 2$ and blank contamination is incapable of inducing the ^3He enrichment. Additionally, no excess ^3He was observed while heating Pt foil (Figure 2.2b), which means the signal could not be due to Pt-foil contamination, leaks, or preferential ^3He diffusion into the furnace during extraction.

2.6.1.1 Preferential liberation of radiogenic ^4He during crushing

The crushing / heating procedure was originally developed to separate inclusion-bound magmatic gas from lattice-bound cosmogenic ^3He ; (e.g. Kurz, 1986b, 1986a; and see discussion in Aciego, Jourdan, et al., 2010, and references therein). But radiogenic ^4He , in contrast, should also be associated with α -recoil-damaged regions surrounding melt inclusions in the olivines, and thus might be preferentially released during crushing. Isotopic fractionations due to variations in the extent of crushing have been observed. Kurz et al. (2004) noted correlations between $^3\text{He}/^4\text{He}$ ratios in gases extracted by crushing and the effective extents of crushing. However, the fractionations observed in that study were orders of magnitude less than those I measured between crushing and heating steps.

Extreme amounts of ^4He would have to be lost to explain the high $^3\text{He}/^4\text{He}$ ratios in the HSDP-2 samples: in the end-member case of R20590, 4.1×10^{-9} ccSTP/g of ^4He must be added back to the 1500°C split to reach a $^3\text{He}/^4\text{He}$ ratio equivalent to that in the crushed fraction (14 R/R_A). As only 5.1×10^{-10} ccSTP/g ^4He was released during heating, this would effectively require preferential loss of $\sim 90\%$ of the radiogenic ^4He during crushing. To reach 7 R/R_A requires the addition of 8.7×10^{-9} ccSTP/g ^4He , an amount comparable to that released in the crushing itself. In other words, essentially all the ^4He extracted by crushing would have to be radiogenic, which is unreasonable (and inconsistent with the low U, Th contents in the olivines). I consider it unlikely that significant radiogenic ^4He is preferentially liberated during crushing. The orphaned ^3He phenomenon does not appear to be caused by a dearth of ^4He , but rather by enrichment in ^3He .

2.6.1.2 Heating induced kinetic fractionation of He isotopes

A second possibility is that fractionation is induced during heating steps (most previous studies have used a single heating step only; e.g. Gayer et al., 2008; Kurz et al., 2004). At magmatic temperatures of $\sim 1350^\circ\text{C}$, He diffusivities range from 5.3×10^{-9} to 8.8×10^{-4} cm^2/sec (the latter appropriate for grains affected by internal fractures; Trull and Kurz, 1993). Using these diffusivity values and the scaling relationship length $L^2 = D_{\text{He}} t$, for $t = 1800$ sec in my heating extractions (which is a lower bound, as it does not include ramp-up and significant cooling time), $L = 31$ and 12600 μm , respectively. This suggests that He can be completely removed by diffusion from 160 μm olivine shards during high temperature extraction, and that there should be no isotopic fractionation, regardless of the value of $D_{^3\text{He}}/D_{^4\text{He}}$, the diffusivity ratio of ^3He to ^4He , (which may be somewhat variable: compare Trull and Kurz, 1993 and Shuster, Farley, Sisterson, and Burnett, 2003). Assuming solid state $D_{\text{He}} = \sim 5 \times 10^{-12}$ at lower temperature 500°C (Shuster et al., 2003), then $L = \sim 1$ μm , and variable diffusivities could fractionate He isotopes. However, given $D_{^3\text{He}}/D_{^4\text{He}}$ is generally close to unity (1.09; Trull and Kurz, 1993), it is unlikely that significant ^3He enrichment is caused by variable diffusivities unless the isotopes are diffusing via entirely separate mechanisms. Experiments designed to explore the effect of diffusive kinetic fractionation of He isotopes should constitute future work.

2.6.2 Naturally produced ^3He

There are two natural processes that generate ^3He : cosmogenic production by spallation, and nucleogenic production from (n,α) reactions involving Li in the basalt matrix.

2.6.2.1 Cosmogenic ^3He

To explore the viability of orphaned ^3He production by spallation, I calculated hypothetical exposure ages for the HSDP-2 samples (including both those from the subaerial and submarine sections); post-shield samples 02AMK7B and 02AMK12B, which are known to have cosmogenic ^3He , were not included in these calculations. Ages are based on the ^3He abundances in the 1500°C extractions, assuming that all ^3He is cosmogenic, and a production rate of 140 atoms/g/yr (for an unshielded Hawaiian basalt at sea level; Kurz, 1986a; and references therein). This yields exposure ages of 3–6 kyr for the subaerial samples and 5–22 kyr for the submarine samples (Figure 2.7). These calculations are for unshielded conditions, likely only applicable to subaerial samples; any submarine samples would have been shielded by overlying water. Shielding reduces the production rate, and 1 m of 3 g/cc shielding (300 g/cm^2 ; a meter of rock or equivalent three meters of ocean) stretches the submarine ages to 31–142 kyr. A shielding depth of 600 g/cm^2 pushes the submarine ages to 204–929 kyr, within or exceeding the probable ages of the magmas. Thus even small amounts of shielding (as little as 6 m of water) require exposure times approaching the likely age of the Mauna Kea volcano. In contrast, the subaerial samples may have originally been erupted

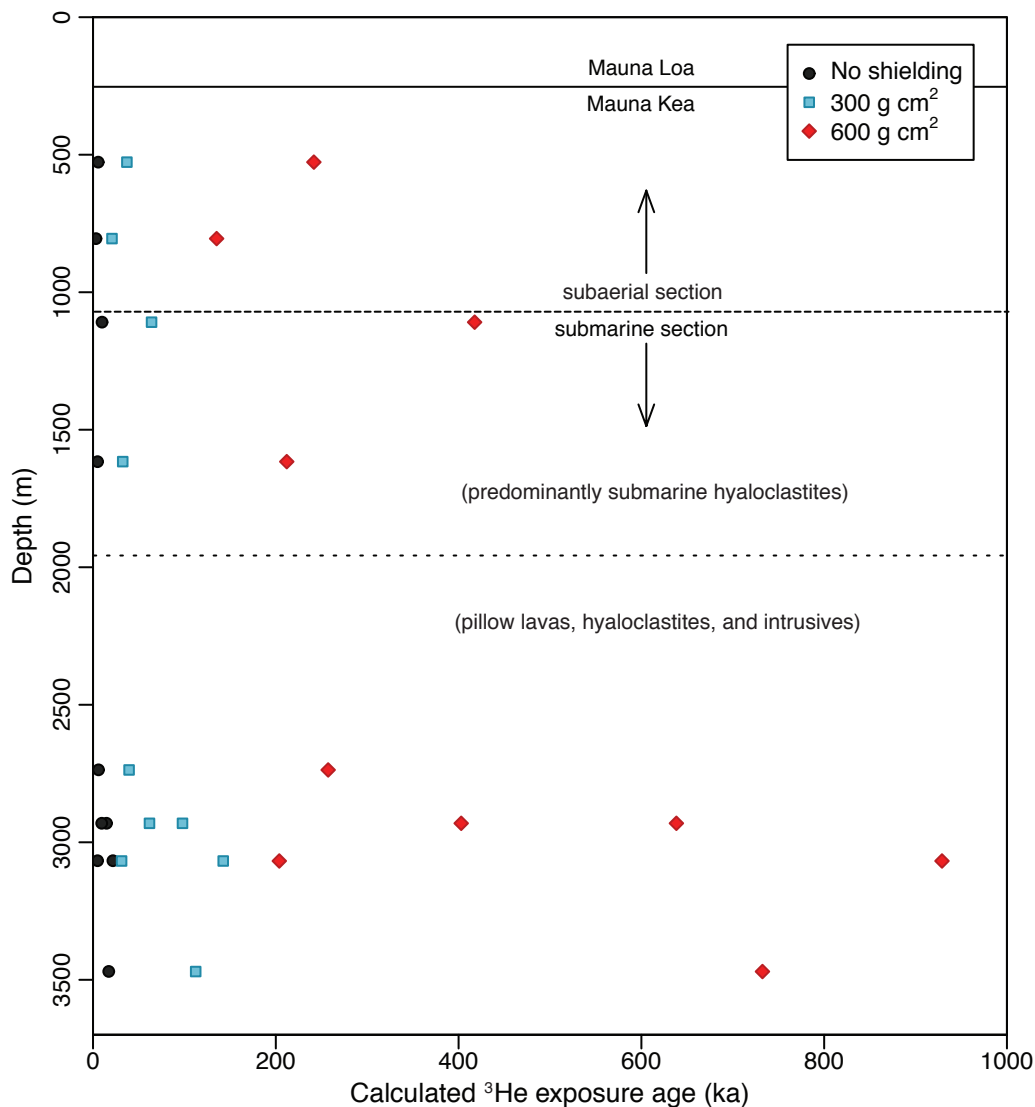


Figure 2.7: Calculated cosmogenic “exposure ages” for HSDP-2 samples based on total 3He content in the $1500^\circ C$ extraction steps; colors indicate different amounts of shielding. These calculations do not take into account greater muon stopping distances (see Kurz, 1986b for discussion), thus calculated ages for the $600 g/cm^2$ shielding case may be slightly over-estimates.

at significant elevation above sea level prior to burial and subsidence as the volcano grew, where cosmogenic production rates would have been even higher. The largest abundances of “anomalous” 3He are in subaerial samples, and are probably cosmogenic. There are smaller effects in the deep samples that are unlikely to be cosmogenic and for which we have no good explanation.

2.6.2.2 Nucleogenic ^3He

Nucleogenic ^3He is produced via neutron capture via $^6\text{Li}(n,\alpha)^3\text{He}$. Since the range for neutrons produced in the U, Th-rich glass matrix is significantly greater than the alpha stopping distance, ^3He production from Li in the matrix-embedded olivines may result in an anomalous ^3He concentration. Using an average bulk composition typical of Hawaii basalts, the calculated ^3He production rate is $\sim 6.7 \times 10^{-3}$ ^3He atoms/g/yr (for 10 ppm Li) and $\sim 6.7 \times 10^{-4}$ (for 1 ppm Li). For the ^3He concentration in sample SR96443B (which contains the minimum ^3He content in our sample set) the Li– ^3He “age” is ~ 110 Ma. These calculations show that nucleogenic ^3He production is hundreds of times too slow to account for the observed effects.

2.7 Conclusions

I analyzed $^3\text{He}/^4\text{He}$ isotope ratios in gas released from *in vacuo* crushing, and subsequent heating, of olivine separates from 14 samples from the HSDP–2 core. For the upper core (<3100 m depth), the magmatic He (released by crushing) has isotopic ratios that overlap with the previously-measured data of Kurz et al. (2004). In the lowermost section of the HSDP–2 core (3100–3500 m), no previous measurements have been made. Magmatic He isotope systematics in the lowermost core are characterized by a relatively narrow range of $^3\text{He}/^4\text{He} = 11.52$ to 14.01 R/R_A with one excursion to 20.19 R/R_A, and most resemble systematics from the 2500–3100 m section. Although the lower core data are spatially limited, the generally modest $^3\text{He}/^4\text{He}$ ratios (as compared with the 2000–2500 m section) suggest that these magmas are of sufficient age that Mauna Kea volcano at that time was still distant from the core of the Hawaiian plume. This is consistent with both growth models for volcano genesis and with the U–Th/He age of sample R20590 (at 3470 m depth).

Initial application of the U–Th/He chronometer to Vesuvius garnets and olivines from post-shield Hawaiian and Snake River Plain basalts has shown promising results in dating Quaternary eruptions. Olivines with low U, Th, He contents from the largely submarine, partially degassed HSDP–2 core introduce several technical challenges, but these types of rocks are key targets for the U–Th/He method because they are extremely difficult to date by other methods as well. Some of the analytical challenges can be addressed by modifications to existing mass spectrometric and data analysis methods, and by careful and repetitive blank analyses.

One major unanticipated difficulty is the presence of excess, or “orphaned” ^3He observed in 1500°C extractions, which does not appear to be an analytical artifact, nor can it be explained by neutron capture effects from Li in the basalt matrix. This excess ^3He makes it impossible to use the 1500°C extraction $^3\text{He}/^4\text{He}$ ratios to correct for residual magmatic gas, and hence leads to significant additional uncertainty in calculated U–Th/He ages. The amount of excess ^3He is the right order of magnitude to be cosmogenic, and this could be the explanation for the subaerial samples, although most were selected from the HSDP–2

core to minimize such possible effects. Although I have considered other possible origins for the ³He, none appear to be a likely explanation.

Despite the orphaned ³He issue, the ages I calculate with this technique are promising, and generally compare well with the scant ⁴⁰Ar/³⁹Ar ages available for the HSDP-2 core. New ages for the lowermost core (from 2900–3500 m) are consistent with accumulation rates similar to the previously-analyzed submarine section, in the range of 15-21 mm/yr predicted by growth models for hotspot-traversing volcanoes. Replicate ages may be highly variable, suggesting that in some cases, corrections for residual gas may be significant. More work must be done to understand the source of the orphaned ³He.

Table 2.1: Hawaiian He data.

Sample ID	Analysis	Weight (g)	Depth (m)	Lith.	$[^4He]$ ccSTP/g	\pm	R/ R_A	\pm
Subaerial post-shield samples:								
02AMK7	Crush		subaerial	a	8.42E-10 ¹	6.27E-11	8.2 ¹	
	300° C		subaerial				-17.95 ²	168.45
	1550° C		subaerial		4.05E-10 ¹	4.26E-11	87.02 ²	15.96
02AMK12	Crush		subaerial	a	2.91E-10 ¹	6.72E-11	10.4 ¹	
	300° C		subaerial				10.77 ²	269.27
	1550° C		subaerial		1.99E-10 ¹	4.26E-11	83.79 ²	143.46
Subaerial HSDP-2 samples:								
SR18059A2	Crush	0.8788	515	b	3.38E-09	1.79E-11	4.4	0.32
	550° C	0.2487	515		4.73E-11	4.49E-12	332.15	45.68
	1550° C		515		-1.47E-11	5.51E-12	-42517.57	956.59
SR222-BMK	Crush	1.311	527	b	4.78E-09	1.45E-11	7.47	0.45
	300° C	0.47245	527		-4.72E-12	2.31E-12	-1194.63	215.49
	1500° C		527		5.16E-10	2.31E-12	41.26	3.91
SR340100	Crush	0.8506	805	b	1.08E-08	1.28E-10	12.77	0.57
	500° C	0.4059	805		2.78E-10	3.2E-12	22.52	4.06
	1550° C		805		5.72E-10	6.14E-12	20.83	2.64
Submarine HSDP-2 samples:								
SR455740	Crush	0.8013	1109	c	7.79E-09	4.21E-11	12.03	0.42
	500° C	0.4114	1109		8.36E-09	8.59E-11	65.28	1.23
	1550° C		1109		1.15E-09	2.42E-11	31.99	2.38
SR630620	Crush	0.7437	1616	c	1.72E-08	1.36E-10	10.65	0.47
	500° C	0.3787	1616		1.29E-08	1.23E-10	25.14	0.72
	1500° C		1616		1.58E-09	2.69E-11	11.82	1.19
SR891151	Crush	0.7787	2737	d	1.82E-08	1.94E-10	13.5	0.48
	500° C	0.3437	2737		1.4E-10	2.81E-12	14.19	5.54
	1570° C		2737		1.22E-09	1.7E-11	18.58	1.18
	1600° C		2737		2.37E-10	1.02E-11	22.8	6.51
SR9301585	Crush	0.9546	2931	e	2.35E-08	9.58E-11	13	0.23
	530° C	0.4071	2931		3.29E-10	1.26E-11	118.62	12.68
	1550° C		2931		4.77E-09	5.42E-11	11.79	0.83
	1620° C		2931					
SR964430	Crush	0.8629	3068	e	8.37E-08	6.26E-11	12.38	0.15
	530° C	0.255	3068		1.04E-09	9.44E-12	1152.5	20.59
	1550° C		3068		9.31E-10	1.47E-11	87.91	5.16
	1635° C		3068		2.68E-10	1.59E-11	8.61	4.28
SR964430-A	Crush	0.9138	3068	e	1.17E-08	3E-10	12.85	0.31
	Re-Crush	0.9138	3068		4.04E-10	1.15E-11	14.18	2.23
R13010	Crush	0.7632	3326	f	7.92E-08	6.42E-10	20.19	0.5
	Re-Crush		3326		-1.33E-09	8.77E-11	-10.48	1.83

Table 2.1: Continued

Sample ID	Analysis	Weight (g)	Depth (m)	Lith.	$[^4He]$ ccSTP/g	\pm	R/R _A	\pm
Submarine HSDP-2 samples:								
R18810	Crush	1.1086	3419	d	8.07E-09	6.56E-11	13.96	0.36
	Re-Crush		3419		1.98E-09	2.84E-11	14.42	0.64
R19230	Crush	0.8487	3430	c	4.73E-09	4.82E-11	11.52	0.49
	Re-Crush		3430		6.62E-10	7.45E-12	12.29	1.29
R201-5.0	Crush	1.1586	3457	d	1.35E-08	5.64E-11	13.15	0.28
	Re-Crush	1.1586	3457		4.8E-10	1.42E-11	12.41	1.59
R205-9.0	Crush	1.0875	3470	d	7.03E-09	9.18E-11	14.01	0.47
	Re-Crush	1.0875	3470		6.66E-10	7.27E-12	12.59	1.13
Campaign 2 analyses:								
02AMK7B	Crush		subaerial					
	530° C	0.265	subaerial	a	-6.84E-11	1.2E-11	-63.27	92.23
	1530° C		subaerial		2.06E-10	1.93E-11	338.69	80.49
02AMK12B	Crush		subaerial	a	4.18E-09	2.72E-10	5.56	1.27
	530° C	0.293	subaerial		-5.17E-11 ³	-1.82E-10	-66.50 ³	312.09
	1530° C		subaerial		3.55E-10 ³	1.83E-10	117.62 ³	69.75
SR9301585B	Crush		2931					
	530° C	0.2509	2931	e	3.09E-10	2.15E-11	-0.98	31.17
	1550° C		2931		2.12E-09	1.4E-10	16.73	7.59
SR964430B	Crush		3068					
	530° C	0.2801	3068	e	9.39E-11	1.32E-11	191.61	145.85
	1550° C		3068		4.35E-10	3.01E-11	41.24	25.51
R20590	530° C	0.1792	3470	d	7.81E-11	1.4E-11	122	140.83
	1550° C		3470		5.11E-10	3.55E-11	126.22	36.08

Lithologies: (a) subaerial post-shield basalt; (b) subaerial HSDP-2 massive basalt; (c) submarine HSDP-2 massive basalt; (d) submarine HSDP-2 pillow basalt; (e) submarine HSDP-2 pillow breccia; (f) intrusive HSDP-2 massive basalt.

¹ Data are from Aciego, Jourdan, et al. (2010).

² Original analyst: Aciego. Re-corrected from raw data for this study.

³ He data for 02AMK12B are blank-corrected using a mean furnace blank.

Table 2.2: U–Th/He ages

Sample ID	[^4He] (ccSTP/g)	\pm	[U] (ng/g OL)	\pm	[Th] (ng/g OL)	\pm	age (ky)	\pm
02AMK7B ²	2.06E-10	1.93E-11	4.87	0.24	18.31	0.92	185	18
02AMK12B ³	3.55E-10 ¹	1.83E-10	4.27	0.21	5.39	0.27	529	274
SR222	5.16E-10	2.31E-12	2.67	0.11	4.71	0.19	171	5
SR9301585	4.77E-09	5.42E-11	5.23	0.21	7.98	0.32	2089	67
SR9301585B	2.12E-09	1.40E-10	10.93	0.55	8.64	0.43	1354	94
SR964430	9.31E-10	1.47E-11	2.6	0.1	4.45	0.18	1121	38
SR964430B	4.35E-10	3.01E-11	5.3	0.27	5.18	0.26	552	40
R20590	5.11E-10	3.55E-11	5.37	0.27	6.27	0.31	618	45

¹ Data are from Aciego, Jourdan, et al. (2010).

² Compare with previously measured ages: 123 \pm 5 ka (Ar plateau); 119 \pm 26 (U–Th/He); Aciego, Jourdan, et al. (2010).

³ Compare with previously measured ages: 450 \pm 100 (Ar integrated); 393 \pm 25 (Ar plateau); 87 \pm 40 (U–Th/He), 91 \pm 36 (U–Th/He); Aciego, Jourdan, et al. (2010).

Chapter 3

Ca–Mg isotopic probe of granite petrogenesis: Lhasa region, Tibet

3.1 Introduction

Granitic rocks constitute a major fraction of the continental crust, and continue to be a subject of great interest in geochemistry. Despite their common occurrence, many aspects of their formation are still debated. The isotopic composition of granitic rocks, for elements such as Sr, Nd, Pb, Hf, and O, can be particularly informative regarding the processes that generate granitic rocks (e.g. Depaolo, 1981; Condie, Belousova, Griffin, & Sircombe, 2009; Kemp, Hawkesworth, Collins, Gray, & Blevin, 2009; Nelson & DePaolo, 1985; O’Neil & Chappell, 1977; Dhuime, Hawkesworth, Cawood, & Storey, 2012; Hawkesworth et al., 2010, and others). Less commonly used isotopic systems, like radiogenic ^{40}Ca (produced by beta decay of ^{40}K) have also been used to advantage (Kreissig & Elliott, 2005; Marshall & DePaolo, 1982, 1989). Relatively recent advances in mass spectrometry have expanded the range of elements that can be useful as tools for investigating granite petrogenesis. Initial studies of Mg (Shen, Jacobsen, Lee, Yin, & Morton, 2009), Fe (Beard, C. M. Johnson, et al., 2003; Poitrasson & Freydier, 2005), and Ca (S. Huang, Farkaš, & Jacobsen, 2011; Simon, DePaolo, & Moynier, 2009; Simon & DePaolo, 2010) appear promising. This study focuses on Ca and Mg isotopes in granitic rocks using a suite of samples from southern Tibet that are part of the relatively young and well-exposed Gangdese batholith. I use Sr and Nd isotopes as indicators of the relative roles of crustal- and mantle-derived magma, and interpret the Ca and Mg isotopic data in that context.

3.2 Background

3.2.1 Geologic History

The Tibetan block (Figure 3.1) was assembled during the Paleozoic and Mesozoic as a series of terrains and arcs (the last of which was the Lhasa block) that were sequentially accreted to the southern margin of Asia (P. Kapp et al., 2007; Yin & Harrison, 2000; Chung et al., 2005). Prior to the most recent collision, the southern margin of Tibet was a northward-dipping continental subduction zone, likened to the American Cordillera, that produced the Gangdese batholith during Cretaceous and early Cenozoic time, and resulted in convergent thickening prior to the closing of the Tethys and the collision with India. The timing of the Indo-Asian collision is still debated; 50 Ma is commonly quoted (e.g. Royden, Burchfiel, & van der Hilst, 2008), but older (as early as ~ 70 Ma; Yin and Harrison, 2000) and younger (~ 30 Ma; Aitchison, Davis, and Luo, 2002) ages have been suggested. I follow T.-Y. Lee and Lawver (1995) in assuming an early “soft” collision followed by a “hard” collision where Indian basement contacted Asian basement at ~ 50 -55 Ma. At the time of hard collision, following quiescence that has been attributed to flat-slab subduction, there was a trenchward flare-up of Gangdese plutonism and corresponding Linzizong volcanism. The flare-up has been linked to the end of oceanic subduction, either due to slab foundering as continental India collided (e.g. Wen et al., 2008) or, alternatively, to roll-back and delamination (P. Kapp et al., 2007; Chung et al., 2005). Ophiolite sequences were emplaced along the Indus-Tsangpo Suture (ITS) during the closing of the Tethyan Sea. Subsequent post-collisional widespread but low volume high-K and ultra-K volcanism, as well as young plutonism, continued in the southern Lhasa block; possibly due to further delamination of the thickened root. Magmatism in Southern Tibet terminated about 10 Ma (or migrated north to the Qiangtang block) as the Indian continental lithosphere moved northwards beneath Tibet, leading to the current thermal regime of cold, stiff Indian lithosphere supporting warm Tibetan crust (Hung, Chen, & Chiao, 2011). The current Tibetan crust is extending along N-S trending Quaternary normal faults.

3.2.2 Sr and Nd Isotopic Context

Over the past 30 years, numerous Sr and Nd isotopic studies of Himalayan and Tibetan rocks have been carried out. The past decade in particular has seen an increase in geochemical studies of the Lhasa-region plutonic and volcanic rocks (e.g. Guo, Wilson, & Liu, 2007; Hou, Gao, Qu, Rui, & Mo, 2004; J. L. D. Kapp, Harrison, Kapp, Grove, & Lovera, 2005; Zhao, Mo, et al., 2009; Ma et al., 2013). Clear spatial and temporal trends in the “traditional” radiogenic isotopes can be observed, and are exhibited by the data I collected for this study (Figure 3.2). The Sr and Nd isotopes of Lhasa-region granitic rocks form an array that is observed in many other continental magmatic arcs, describing a trend from typical mantle values ($\epsilon_{Nd} \sim +8$, $^{87}\text{Sr}/^{86}\text{Sr} \sim 0.703$) toward increasingly crustal characteristics (negative ϵ_{Nd} and high $^{87}\text{Sr}/^{86}\text{Sr}$). In the Lhasa region this trend also corresponds to increased northward

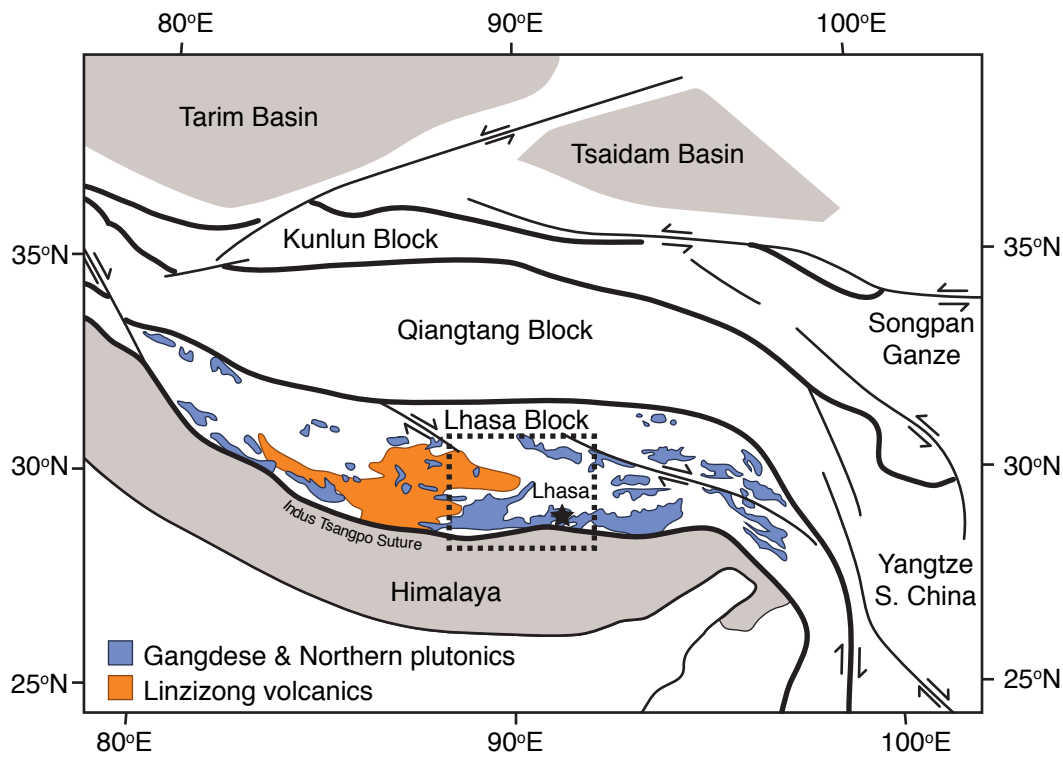


Figure 3.1: Simplified geologic map of the Lhasa block showing terrains and major boundaries and faults, after Chung et al. (2005). Gangdese and Linzizong volcanics of the Lhasa block are shown. Dashed rectangle encloses the region of study in Figure 3.3.

distance from the ITS. The observed spatial trend is analogous to those observed in the Peninsular Ranges batholith (e.g. DePaolo, 1981), where the increasingly negative ϵ_{Nd} and positive $^{87}\text{Sr}/^{86}\text{Sr}$ of the continentward plutonics is thought to be due to increased participation of ancient continental basement in granite petrogenesis. In these and other locations the isotopes have been used to delineate the edges of the ancient cratons (e.g. Kistler & Peterman, 1978; Farmer & DePaolo, 1983; Borg, DePaolo, & Smith, 1990).

In the Lhasa area the continental collision might be expected to have modified the sources of granitic magmas. In pre-collision granites, there is a pronounced isotopic delineation between more “mantle-like” values (ϵ_{Nd} ranging from +2 to +6) emplaced nearest the subduction zone (to the south of 29.8°N), and higher values to the north, which range from $\epsilon_{Nd} = 0$ to -12. Prior to ~ 50 Ma, latitude 29.8°N appears to mark the southern edge of ancient continental basement (DePaolo et al., in prep.). Syn-collisional and in particular, post-collisional granites emplaced south of 29.8°N , however, extend to more crustal isotopic values, and their increasingly radiogenic $^{87}\text{Sr}/^{86}\text{Sr}$ and unradiogenic ϵ_{Nd} indicate changes in the granitic magma source subsequent to ~ 50 Ma.

Initial studies have shown that Mg and Ca isotopes, in addition to Nd, Sr, and O isotopes,

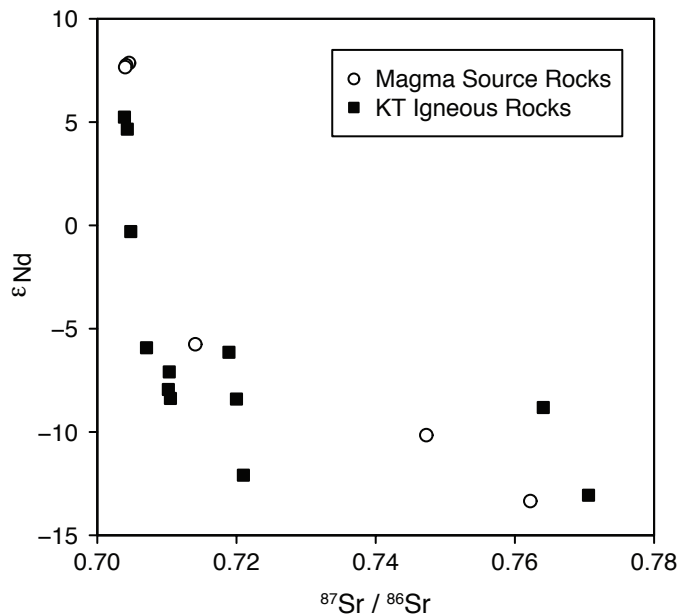


Figure 3.2: Sr and Nd isotopes for Lhasa-region plutonic and volcanic rocks analyzed in this study. The Cretaceous-Tertiary igneous rocks show the common relationship between Nd and Sr isotopes. Samples with ϵ_{Nd} lower than -5 are mostly or entirely formed by crustal melting, whereas those with higher ϵ_{Nd} are generally interpreted to be mantle derived subduction zone magmas that have assimilated some crustal material. Open circles are samples that crudely represent possible magma source materials in the crust and mantle. The samples with $\epsilon_{Nd} \sim +8$ are from the Jiding ophiolite, which represent mantle magma sources, whereas the samples with low ϵ_{Nd} are gneiss and schist from the Tethyan Himalaya (Table 3.1). The igneous rocks also show a correlation of ϵ_{Nd} with distance north from the ITS; those close to the suture have high ϵ_{Nd} , and those farther to the north have decreasing ϵ_{Nd} values.

may show variations in plutonic rocks (e.g. Shen et al., 2009; Marshall & DePaolo, 1989). The goal of this chapter is to explore the potential of “non-traditional” light isotopes (Mg and Ca) as tools to investigate granite magma sources in an area where there are large and systematic variations of Sr and Nd isotopes.

3.2.3 Samples

Most samples in this study (locations shown in Figure 3.3) were collected from a region near the longitude of Lhasa (ca. 90°E), from the ITS (in the south) to the north-central Nyainqentanglha Shan Massif (NQTL Massif). Of primary interest are granitoid and silicic volcanic samples, as these are more likely to have been generated through crustal anatexis or assimilation, and therefore provide information about the changing nature of the continental crust during the onset of Himalayan collision. Additional samples, including rocks from the Jiding Ophiolite and the Kangmar Gneiss dome (south of the ITS) were collected as possible representatives of mantle and crustal magma sources. Thus the sample suite consists of a

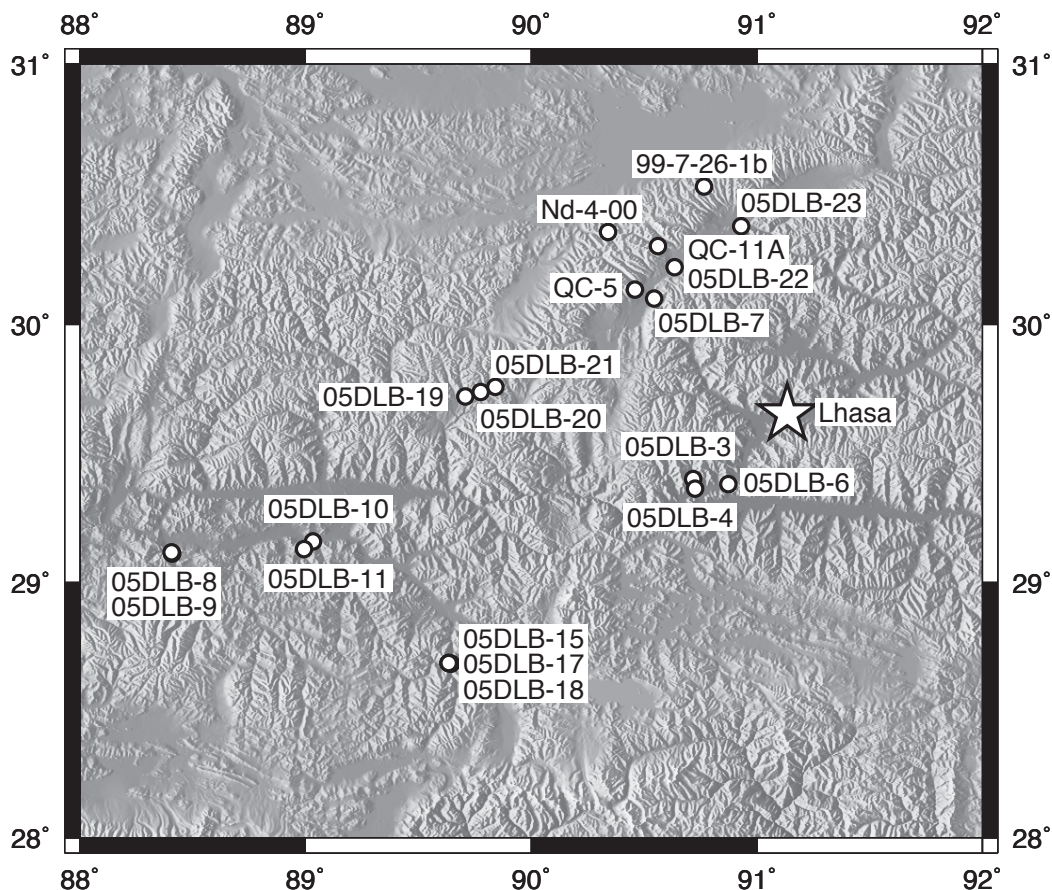


Figure 3.3: Map of the study area surrounding Lhasa, Tibet, showing sample locations. Map is ~ 400 km wide, and corresponds to the dashed rectangle shown in Figure 3.1.

wide variety of rock types that range in age from ~ 500 Ma (Kangmar granitic gneiss) to 10 Ma. Most of the granitic samples are of early Cenozoic age.

The oldest, pre-collisional, Lhasa block samples in our study are Mesozoic in age, and include a 213 Ma 2-mica granite from the NQTL Massif (99-7-26-1b), and a ~ 190 Ma Ningzihong monzogranite (05DLB-23). NQTL samples in this study are described in J. L. D. Kapp et al. (2005) and references therein. The Ningzihong granite is peraluminous and consists largely of quartz, plagioclase with sericitized cores, perthitic k-feldspar, and subordinate tabular phenocrystic white mica; additional information on this granite can be found in Liu et al. (2006).

The suite includes 5 syn-collisional (~ 50 Ma) igneous samples. Three are Gangdese arc plutonic rocks exposed in the southernmost Lhasa block between Quxu and Lhasa: a gabbro (05DLB-3), a lower-silica calc-alkaline diorite (05DLB-4), and a higher silica, alkaline diorite/syenite (05DLB-6); all correspond to the ~ 50 Ma “flare up” of renewed southern

Gangdese arc magmatism. In addition, I analyzed a contemporaneous garnet-bearing 2-mica alkali granite (05DLB-7) and a shoshonite (05DLB-22) from near Yangbaijiang (across the Yangbaijiang-Damxung graben from the NQTL, ~90 km north of Lhasa). The 2-mica granite sample corresponds to XGS-86 of Xu, Schärer, and Allègre (1985). The shoshonite is a porphyritic rock containing abundant large analcite phenocrysts (up to ~1 cm diameter), commonly cut by veins of apatite (these veins are restricted to the analcite phenocrysts and do not cross-cut the section). Rare small euhedral-to-subhedral phenocrysts of apatite or calcite are also present in the matrix.

I have included 3 post-collisional, Miocene (11 to 20 Ma) granites from the NQTL Massif in this study, including a garnet-bearing 2-mica granite (QC-11a), and two alkali granites (QC-5, and ND-4-00). Based on their trace element and isotopic characteristics, young NQTL granites are inferred to be derived largely from reworked or partially melted Gangdese plutonic rocks (J. L. D. Kapp et al., 2005).

Silicic volcanic samples include Miocene (10-15 Ma) alkali-rich rhyolitic tuffs of the Wuyu Volcanics (05DLB-19, 05DLB-20), and Marjiang Pass (05DLB-21). The geochemistry of mafic Wuyu rocks has been previously attributed to a mixed source of Gangdese basement +/- Gangdese plutonic rocks and a more depleted end-member, possibly subducted, partially eclogitized oceanic crust, with a heat-source provided by upwelling asthenosphere following delamination event(s) (Zhao, Xuanxue, et al., 2001; Zhou et al., 2010).

Several samples from the ITS were included, including two microgabbros (05DLB-8 and 05DLB-9) and a pillow basalt (05DLB-10) from the Jiding Ophiolite (Dubois-Cote et al., 2005; R. Wang et al., 2006; Aitchison, Davis, Abrajevitch, et al., 2003; Malpas, Zhou, Robinson, & Reynolds, 2003). The pillow basalt, 05DLB-10, contains visible carbonate in thin section, present as twinned calcite veins and as vesicle-filling crystals. Carbonate contents range from negligible to ~15% in more highly vesicular portions of the sections.

North of the ITS there are very few exposures of pre-Gangdese basement, but south of the suture the basement is exposed in metamorphic core complexes. I analyzed one granitic gneiss and two schist samples from the Kangmar Dome (Z. Chen et al., 1990; J. Lee et al., 2000; Schärer, U. and Xu, R.-H. and Allègre, C. J., 1986; Wagner, Lee, Hacker, & Seward, 2010), one of a series of gneiss-cored domes whose formation has been attributed to gravitational collapse of over-thickened crust (J. Lee et al., 2000) and mid-crustal flow (Wagner et al., 2010). The core of the dome consists of a granitic gneiss that was emplaced 508-560 Ma, unconformably overlain by Carboniferous to Triassic sediments that range from unmetamorphosed to staurolite-kyanite facies. The metasediments have Ar/Ar mica ages of 13-20 Ma (coincident with peak metamorphism of the dome). Sample 05DLB-15 is a strongly lineated granitoid gneiss; samples 05DLB-17 and -18 are 2-mica garnet schists.

3.3 Procedures

3.3.1 Mg and Ca Analytical Techniques

High-K and high-Al samples, such as 2-mica granites, metapelites, and ultrapotassic rocks are uniquely challenging for Ca and Mg isotopic analyses because of the deleterious effects of K and Al during both TIMS and MC-ICP-MS measurements. Excess Al inhibits Ca ionization during TIMS analyses, and typically produces erratic mass fractionation and poor reproducibility. During MC-ICP-MS analyses, matrix (including Ca, Al, and K) has been shown to cause aberrant mass fractionation of Mg isotopes (cf. Wombacher, Eisenhauer, Heuser, & Weyer, 2009). Additionally, because cation exchange chemistry fractionates Mg isotopes (Chang, V. T. C. and Makishima, A. and Belshaw, N. S. and O’Nions, R. K., 2003; F. Huang, Glessner, Ianno, Lundstrom, & Zhang, 2009), recovery must be quantitative while eliminating virtually all of the problematic chemical elements. In pelites, metapelites, and two-mica granites, the molar ratio of Al/Ca can be >100 , requiring careful separation.

The separation procedure for Mg is adapted from Wombacher et al. (2009), scaled for use with preformed BioRad columns. It was found that in samples of high K/Mg, significant K was present in Mg cuts using this single column procedure, and so all samples were first passed through a “pre-treatment” cation exchange column (using AG50 resin). Alkalis were eluted from this first column using 1 N HNO₃, and then the remaining major elements (Mg, Ca, and Fe) were eluted using 4 N HNO₃. A minimum of 10 μg Mg was processed per sample. Mg samples were processed in batches of 4 plus two standards, one a DSM3, and the other one of BCR-1, GSP-1, or GSP-2. CAM-1 was also processed through chemistry once. A comparison of standards is presented in Figure 3.4. Mg isotopes were measured at the University of California, Davis, on a Thermo Finnigan Neptune MC-ICP-MS using wet plasma introduction by an Apex desolvation nebulizer, in concentrations of ~ 500 ppb, which yields 10-12 V total beam intensity with a 10^{11} Ohm feedback resistor in the amplifier. Concentrations were adjusted to match standards. Triplicate measurements of each sample were made using the sample-standard bracketing technique.

Mg isotope ratios are expressed as $\delta^{26}\text{Mg}$, the per mil deviation of $^{26}\text{Mg}/^{24}\text{Mg}$ relative to the DSM3 standard. Fractionation was monitored by replicate analysis of the CAM-1 standard; the average during the study was $\delta^{26}\text{Mg} = -2.59 \pm 0.07$ (2σ), $\delta^{25}\text{Mg} = -1.34 \pm 0.04$ (2σ). The CAM-1 standard that was processed through chemical separation gave $\delta^{26}\text{Mg} = -2.58 \pm 0.05$, $\delta^{25}\text{Mg} = -1.34 \pm 0.02$. Typical triplicate measurements have $2\sigma = 0.03$ to 0.10‰ . A more realistic error can be obtained from the standards and samples that were processed through replicate chemistries; 2σ for $\delta^{26}\text{Mg}$ was 0.11‰ for DSM3 ($n = 9$ column chemistry replicates), 0.06‰ for BCR-1 ($n = 5$), 0.08‰ for GSP-1 ($n = 6$), and 0.10‰ for GSP-2 ($n = 3$). Additionally, full-chemistry (including dissolution) replicates were processed on two low-Mg granitoids and one low-Mg tuff; the averages for these replicates agree to within 0.12‰ ; thus the likely reasonable precision to measurements of low-Mg samples processed in this study is probably within that envelope. BCR-1 replicates are within the range reported for BCR-1 and BCR-2, and agree well with estimates of bulk silicate

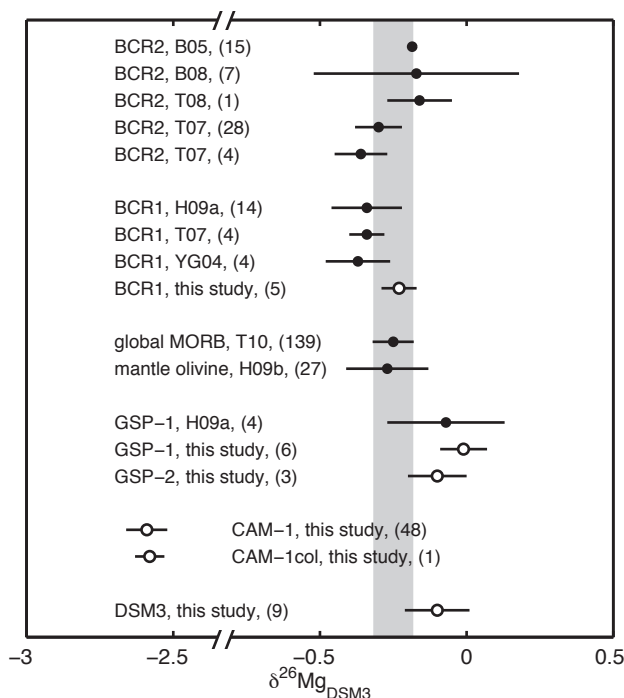


Figure 3.4: Comparison of $\delta^{26}\text{Mg}_{\text{DSM3}}$ standards from this study with values from the literature (this study: open circles; literature: solid). References are B05a: Baker, Bizzarro, Wittig, Connelly, and Haack (2005); B05b: Bizzarro, Baker, and Lundgaard (2005); T08: Tipper, Louvat, Capmas, Galy, and Gaillardet (2008); T07: F. Z. Teng, Wadhwa, and Helz (2007); H09a: F. Huang et al. (2009); YG04: Young and Galy (2004); T10: F.-Z. Teng et al. (2010); H09b: Handler, Baker, Schiller, Bennet, and Yaxley (2009). Numbers in parentheses refer to number of replicates reported by authors. For this study, numbers in parentheses for all except CAM-1 refer to the number of full column chemistry replicates (each of these replicates was analyzed 3 times); for CAM-1, it refers to number of replicates of un-processed CAM-1 standard.

Earth (BSE) composition (which we take to be $\delta^{26}\text{Mg}_{\text{DSM3}} = -0.25\text{‰}$). The inter-laboratory discrepancies in rock standard values reported in the last few years of Mg measurements have shrunk to $\sim 0.10\text{‰}$ (in $\delta^{26}\text{Mg}$), approximately equal to 2σ on replicate measurements, and may be due to difficulties in obtaining clean, quantitative Mg yields for analysis.

Ca was separated and analyzed by TIMS at the Center for Isotope Geochemistry at the University of California, Berkeley. Both spiked (e.g. double spiked) and unspiked samples were separated using similar chemical procedures. Because the double spike isotopic composition is substantially different from Ca in natural samples, it is a potential contaminant (even in trace quantities) to unspiked samples. To mitigate this problem, all unspiked samples were processed in separate lab facilities with separate equipment and reagents, where no Ca spike has been used. The separation procedure for Ca for both spiked and unspiked samples is adapted from cation chemistry of Simon and DePaolo (2010), with the notable addition of a dilute ($\sim 0.15\text{ N}$) HF wash (which removes a significant portion of Al, in addition

to HFSE, including Ti) prior to elution of Ca. Calcium was further purified using a second column and Eichrom Technologies DGA resin (Nielsen, Druhan, Yang, Brown, & DePaolo, 2012). Description of the spectrometric methods for spiked Ca analysis is presented in Simon and DePaolo (2010) and references therein; I follow this procedure with the exception that during spike subtraction, instead of using a specified “normal” for all samples, I use the measured $^{40}\text{Ca}/^{44}\text{Ca}$ from the unspiked measurements (in practice, this results in < 0.04 per mil difference from the calculated $\delta^{44}\text{Ca}$ using the normals of Simon and DePaolo, 2010; or Skulan, DePaolo, and Owens, 1997). Spike subtraction was performed using a MATLAB script; the computation is based on the treatment by Rudge, Reynolds, and Bourdon (2009).

The procedure for mass spectrometric analysis of unspiked Ca is largely based on that in Simon, DePaolo, and Moynier (2009). In brief: the $^{40}\text{Ca}+$, $^{42}\text{Ca}+$, $^{43}\text{Ca}+$ and $^{44}\text{Ca}+$ ion beams were measured simultaneously in a static cup configuration, with the intensity of the $^{40}\text{Ca}+$ beam at a minimum of 25 V. Instrumental mass fractionation was corrected using an exponential law, assuming $^{42}\text{Ca}/^{44}\text{Ca} = 0.31221$. Typical runs exhibited a smooth monotonic decline from $^{42}\text{Ca}/^{44}\text{Ca}$ (uncorrected) = 0.315 to 0.312. Faraday cup collector efficiencies degrade over time, presumably as the carbon lining of the cup is modified due to Ca plating. This effect is readily observed as a loss in efficiency of the ^{40}Ca -specific cup, generally in a lowering of the $^{40}\text{Ca}/^{44}\text{Ca}$ ratio. During the course of the study, Faraday cup liners were replaced as needed, and unspiked data was collected and used only during those periods following replacement of cup liners, when replicate measurements of BCR-1 standards were stable. To monitor cup efficiencies (and to detect possible spike contamination, which also results in anomalously low $^{40}\text{Ca}/^{44}\text{Ca}$ ratios) each unspiked barrel included 16 samples and 6 standards: three of BCR-1 and three of SRM915A (Figure 3.5). The BCR-1 analyses showed sufficiently good agreement between barrels that no further normalization was necessary.

3.3.2 Comment on the $^{40}\text{Ca}/^{44}\text{Ca}$ of Bulk Silicate Earth

The long-term ($n = 26$) unspiked measured value of $^{40}\text{Ca}/^{44}\text{Ca}$ for BCR-1 was 47.1642 (Figure 3.5); slightly higher than the mantle/BSE value of 47.162 recommended by Caro, Papanastassiou, and Wasserburg (2010) and Nielsen et al. (2012). This suggested mantle ratio 47.162 is distinct from the MORB glass (unspiked $^{40}\text{Ca}/^{44}\text{Ca} = 47.1550$) analyzed by Kreissig and Elliott (2005); the reason for this is not readily apparent. However, these authors measured SRM915A and found it to be $\varepsilon_{\text{Ca}} = +1.15$ (relative to their MORB glass). This relative enrichment agrees with the long-term average ($n=24$) of SRM915A in this study (relative to 47.162) of $\varepsilon_{\text{Ca}} = 1.38 \pm 1.34$ (2σ). These values are within error of the values reported by Simon, DePaolo, and Moynier (2009): $\varepsilon_{\text{Ca}} = +0.68$ to $+0.93$ for SRM915A relative to BCR-1. Thus, despite the comparatively low absolute ratios reported by Kreissig and Elliott (2005), they report a small radiogenic enrichment of the SRM915A standard with respect to mantle/BSE. This is in contrast with results of Caro et al. (2010) (where no enrichment of SRM915A was observed). My interpretation of the available data is that the SRM915A standard is radiogenically enriched with respect to mantle/BSE by $\sim 1 \pm 0.3$ ε_{Ca} -unit, and that $^{40}\text{Ca}/^{44}\text{Ca}$ of BSE is 47.162. All ε_{Ca} in this study are reported relative

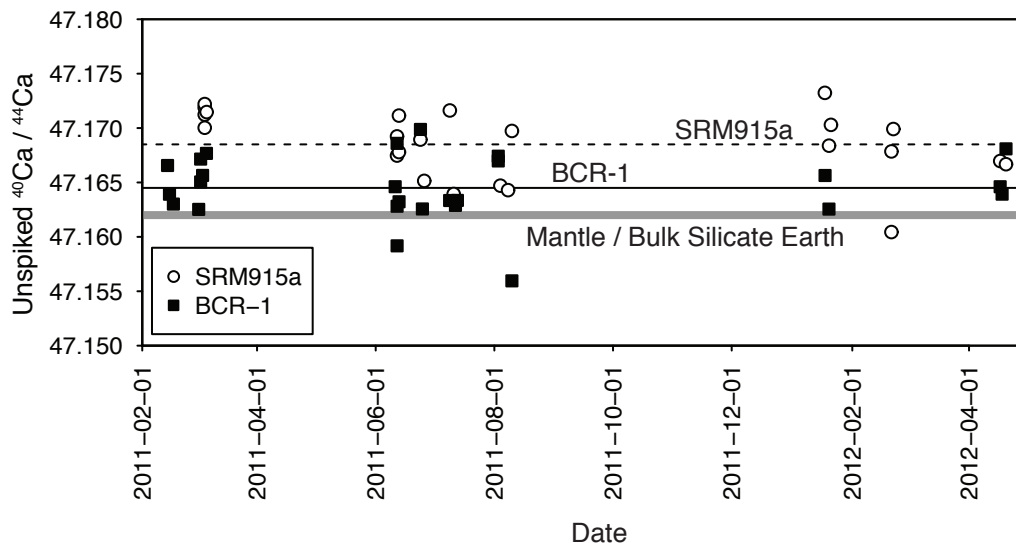


Figure 3.5: Unspiked $^{40}\text{Ca}/^{44}\text{Ca}$ standards by date for the duration of the study. Filled squares are BCR-1, open circles are SRM915A. Solid gray line marks 47.162, the $^{40}\text{Ca}/^{44}\text{Ca}$ of mantle/BSE (assuming $^{42}\text{Ca}/^{44}\text{Ca} = 0.31221$). Black line is long-term BCR-1 average; dashed line is the long-term SRM915A average.

to this BSE ratio. All stable Ca isotopic measurements (e.g. spike-subtracted $\delta^{44}\text{Ca}$) are corrected for radiogenic ingrowth and are also reported relative to $^{40}\text{Ca}/^{44}\text{Ca}_{\text{BSE}}$ of 47.162. The long-term BCR-1 with respect to mantle/BSE is slightly enriched, with $\varepsilon_{\text{Ca}} = 0.53 \pm 1.27$ (2σ). Since BCR-1 does not have primitive values for Nd and Sr isotopes, it is possible that it has elevated ε_{Ca} relative to BSE. Our SRM915A measures $\varepsilon_{\text{Ca}} = 1.38 \pm 1.33$.

3.4 Results

3.4.1 Radiogenic Ca isotopes

Most of the granitic and volcanic samples have ε_{Ca} values within 1 unit of the mantle or bulk Earth value (Figure 3.6). Two of the 2-mica granite samples have clearly elevated ε_{Ca} of almost +3. The samples that are nominally representative of potential magma sources in the mantle and crust have ε_{Ca} values in the range expected. The ophiolite samples are slightly elevated with respect to the accepted mantle values, which could be due to seawater interaction. The gneiss and schist samples have ε_{Ca} between +1 and +5, confirming the availability of radiogenically enriched Ca in relatively silicic crustal magma sources. Most samples are sufficiently young and/or have sufficiently low K/Ca ratios that that age-corrected ε_{Ca} values are only slightly different from the measured values (for Figure 3.6, the gneiss and schist sample values have been calculated for an age of 50 Ma). Exceptions include the Mesozoic granites that have exceptionally high K/Ca ratios. For these samples, the age-

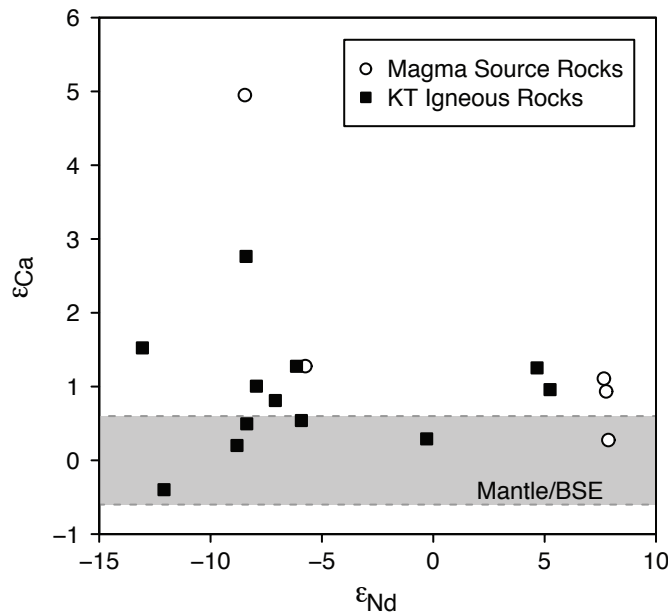


Figure 3.6: ε_{Ca} vs ε_{Nd} for samples in this study. Schists and gneiss are those with negative ε_{Nd} ; Those with mantle-like ε_{Nd} of $\sim +8$ are Jiding Ophiolite samples. In contrast to the Nd isotopic system (where 0 is based on chondrite), 0 in the radiogenic Ca system is anchored by mantle composition; as the K/Ca ratio in the mantle is exceptionally low (with respect to crustal rocks), no terrestrial crustal samples should have ε_{Ca} less than 0.

corrections are as large as 1.8 units for 05DLB-23 and 1.1 units for 99-7-26-1b. Although the initial value of -0.4 for 05DLB-23 is within error of BSE, the negative value suggests over-correction, perhaps due to post-crystallization alteration of the K/Ca ratio (e.g. Kreissig and Elliott, 2005), which might be expected based on the sericitization observed in the plagioclase. The igneous sample with the highest ε_{Ca} ($= +2.7$) is a Miocene granite exposed in the NQTL massif.

3.4.2 Stable Ca, Mg isotopes

Stable $\delta^{26}\text{Mg}$ and $\delta^{44}\text{Ca}$ (radiogenic ingrowth subtracted) for the suite are shown in Figure 3.7. The samples span a considerable range in Ca–Mg isotopic space (Figure 3.7a), with most of the data lying in the quadrant where both $\delta^{26}\text{Mg}$ and $\delta^{44}\text{Ca}$ are lower than the mantle values. Figures 3.7b and c, in which $\delta^{26}\text{Mg}$ and $\delta^{44}\text{Ca}$ are plotted against ε_{Nd} , are instructive because they show that the igneous rocks with mantle-like ε_{Nd} values have a restricted range of both $\delta^{26}\text{Mg}$ and $\delta^{44}\text{Ca}$, whereas the rocks with crustal Nd isotopic values ($\varepsilon_{Nd} < -5$) are much more variable in Mg and Ca isotopes. This pattern indicates that the variability of Mg and Ca isotopes in the plutonic and volcanic samples is traceable to crustal lithologies that are present in the source regions of the magmas. Interestingly, in samples

in this study, most of the deviations in $\delta^{26}\text{Mg}$ are negative relative to mantle values. This contrasts with the findings of W.-Y. Li, F.-Z. Teng, Ke, et al. (2010), that A-type granites tended to have positive or BSE-like values of $\delta^{26}\text{Mg}$ almost exclusively.

Shown in Figure 3.7a are fields representing approximate ranges for rocks where the Mg and Ca isotopic values are variable and in general different from mantle values. There has not been a broad survey of both Mg and Ca isotopic compositions of crustal lithologies, and there is likely more to be learned about the variability present in the crust. Nevertheless, there are enough data for two major sedimentary rock types, and their precursors, that some inferences about the source of crustal Mg and Ca isotopic heterogeneity are possible.

Mg and Ca isotopes undergo kinetic fractionation during carbonate precipitation, with lighter isotopes preferentially concentrated in the precipitated solid. The degree of fractionation is dependent on reaction rate, solution stoichiometry, temperature, mineralogical composition of precipitated material, and - when present - catalytic vital effects (see review in Nielsen et al., 2012, and references therein), leading to the large field shown in Figure 3.7a (see also Fantle & DePaolo, 2007; Hippler, Buhl, Witbaard, Richter, & Immenhauser, 2009; Immenhauser et al., 2010; W. Li, Chakraborty, Beard, Romanek, & Johnson, 2012; Pogge von Strandmann, 2008; Young & Galy, 2004). The isotopic value for seawater is lighter than BSE with respect to $\delta^{26}\text{Mg}$ but heavier with respect to $\delta^{44}\text{Ca}$, leading to carbonate that may have negative $\delta^{26}\text{Mg}_{\text{BSE}}$ but either positive or negative $\delta^{44}\text{Ca}_{\text{BSE}}$.

Soils, shales, loess, sedimentary composites, and some rivers (in addition to A-type granites) are among the natural samples found to contain heavy Mg (see summary in W.-Y. Li, F.-Z. Teng, Ke, et al., 2010 and references therein). It has been suggested that weathering may be a mechanism by which Mg isotopes are fractionated, leading to heavy Mg in residual clays (Shen et al., 2009; Brenot, Cloquet, Vigier, Carignan, & France-Lanord, 2008; Tipper, Gaillardet, et al., 2010; Wimpenny et al., 2010). Preliminary Ca isotopic characterization of shales (Wimpenny, et al., in prep) indicates they may in general be isotopically light with respect to BSE, leading to a reservoir (shown in Figure 3.7) of heavy $\delta^{26}\text{Mg}_{\text{BSE}}$ and light $\delta^{44}\text{Ca}_{\text{BSE}}$.

Higher animals and plants also fractionate both Ca and Mg (Boulou-Bi, Poszwa, Leyval, & Vigier, 2010; DePaolo, 2004; Nielsen et al., 2012). This biotic fractionation almost certainly plays some part in determining the isotopic composition of soils and sedimentary lithologies, although it is not yet clear to what degree it influences the geochemical rock cycle.

Available evidence suggests that Mg isotopes are minimally fractionated during basalt or granite petrogenesis and differentiation (F. Z. Teng, Wadhwa, & Helz, 2007; W.-Y. Li, F.-Z. Teng, Ke, et al., 2010). However, there have been few studies, and recent work suggests that equilibrium fractionation by as much as 1‰ of $\delta^{26}\text{Mg}$ may exist at metamorphic conditions due to difference in Mg-coordination between garnet (2+ cations in 8-fold coordination) and pyroxene and mica (6-fold coordination; W.-Y. Li, F.-Z. Teng, Xiao, and Huang, 2011). It is not known whether anatexis of an eclogite source, for example, would cause isotopic fractionation in terms of Ca and Mg isotopes; it may depend on whether or not residual garnet is produced by incongruent melting (cf reactions b through d of Vielzeuf and Schmidt, 2001).

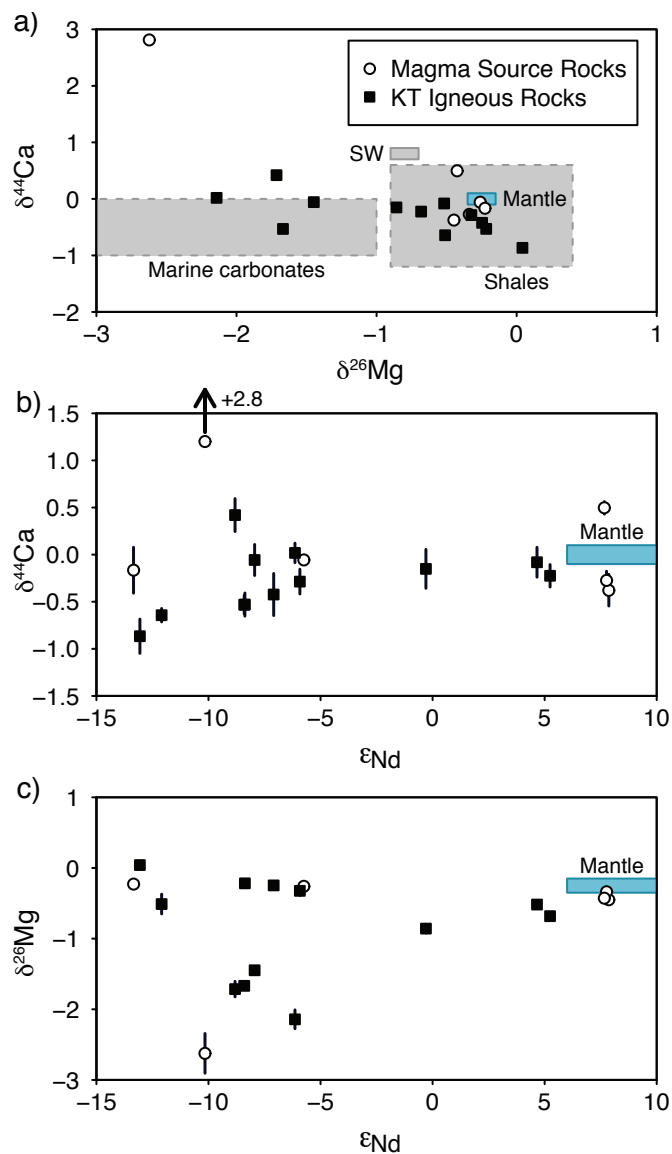


Figure 3.7: $\delta^{26}\text{Mg}$ and $\delta^{44}\text{Ca}$ for Lhasa-region samples. $\delta^{26}\text{Mg}$ is shown with respect to the DSM3 standard, $\delta^{44}\text{Ca}$ is corrected for radiogenic ingrowth and shown with respect to BSE (see text for discussion). In a, fields for marine carbonates, shales, and seawater are also shown in gray; in a through c, blue field indicates mantle composition. In b and c, $\delta^{26}\text{Mg}$ and $\delta^{44}\text{Ca}$ are shown (respectively) against ϵ_{Nd} ; in general, samples with near-mantle ϵ_{Nd} also exhibit near-mantle $\delta^{26}\text{Mg}$ and $\delta^{44}\text{Ca}$, while crustally-derived samples show a wider range.

To date, no studies on garnet-bearing eclogites have been conducted using Ca isotopes, and no experimental studies have been conducted on the isotopic effect of partial melting with residual garnet for either element.

While kinetic fractionation of Ca and Mg can occur at magmatic temperatures (e.g. Richter, Watson, Mendybaev, Teng, & Janney, 2008; Watkins, DePaolo, Huber, & Ryserson, 2009), there is little evidence that kinetic fractionation accompanying crystal growth from magmas or due to temperature and composition gradients in magma chambers plays a major role in determining the Ca or Mg isotopic composition of igneous rocks. Consequently, these compositions must be determined by their magma sources in the upper mantle and deep crust. As noted above, the isotopic variability in crustal rocks is likely to be the source of the observed Mg and Ca isotopic variations in the Tibet igneous rocks, and the crustal isotopic variability in turn is traceable to the weathering cycle, both during the formation of soils and, subsequently, clay-bearing sediments, and in the formation of carbonate (biogenic) precipitates in the oceans (although I revisit the potential effect of garnet in more detail in section 3.5.2, below).

3.5 Discussion

3.5.1 Granitic rock magma source variability

The obvious source of non-BSE, sub-seawater isotopic Ca and Mg in the Lhasa-region granites is from a carbonate assimilant or contaminant. The degree to which a carbonate contaminant could exert widespread changes in chemistry of resulting magmas is a current topic of experimental (Freda et al., 2008; Marziano, Gaillard, & Pichavant, 2007, 2008) and field studies (Chadwick et al., 2007; Barnes, Prestvik, Sundvoll, & Surratt, 2005; Yogodzinski et al., 1996). The result of significant carbonate assimilation is silica undersaturation in the resulting liquid due to the stabilization and crystallization of Ca-rich pyroxene and consumption of olivine (cf Marziano et al., 2007). In granitic systems, this should result in syenitic magmas (Barnes et al., 2005). In mafic magmas that have undergone clinopyroxene fractionation with high Ca-Tshermak (CaTs) content, it will result in silica undersaturation and in deficiencies of Cr and Sc (which are highly compatible in calcic pyroxene; Hill, Wood, and Blundy, 2000).

The Mg and Ca isotopic compositions of the Gangdese arc samples 05DLB-3, 05DLB-4, and 05DLB-6 (which have near-mantle/BSE $\delta^{26}\text{Mg}$ and $\delta^{44}\text{Ca}$) could be explained by small degrees of contamination of mantle-derived magma by a carbonate bearing crustal lithology. 05DLB-6, which is somewhat more alkalic, could have experienced a greater degree of assimilation; however, none of these samples are particularly distinct from “normal” arc granites in terms of their major element, trace element, and isotopic characteristics.

In contrast, syn-collisional samples from farther north (including the mafic shoshonite 05DLB-22 and the granite 05DLB-7), show Mg and Ca isotopic evidence indicative of significant interaction with carbonate; nearby Miocene granites of the NQTL (thought to be

derived from reworked Gangdese plutonics) show similar evidence. Yet in terms of major elements, these syn- and post-collisional granites are not syenitic to the degree observed by Barnes et al. (2005), and show little other evidence of carbonate assimilation (e.g. primary carbonate igneous mineralogy). The only sample showing such evidence is the high-K shoshonite, 05DLB-22, which contains abundant apatite in thin section, low Cr and Sc concentrations at low SiO₂ content, evidence of mineralogical disequilibrium in feldspars, and abundant analcite.

The isotopic effects of the carbonate assimilation (low $\delta^{44}\text{Ca}$ in particular) appear to be constrained in both time and space to a region northwest of Lhasa and to rocks that otherwise appear to be melted from, or contaminated with, a metapelitic component. The rocks that exhibit this evidence are the two samples of older Mesozoic 2-mica granites of the NQTL Massif and two of the samples of the silicic volcanic rocks of the Wuyu Basin and Marjiang Pass. In both cases there is other evidence, for example from the bulk chemical composition and Sr isotopes, that these rocks were formed from melting or assimilation of pelites. Therefore the “carbonate” signature may be due to the fact that many shales contain carbonate. Carbonate-free shales tend to have low Ca concentrations, so the Ca isotopic composition of shales containing carbonate may be dominated by the carbonate even if it is present in small proportion (a few %). Mg is more likely to be dominated by the clay component, but could be more equally distributed between silicate and carbonate components. This rationalization of the apparent carbonate signature is conjectural, as there are few available analyses of shales, and the meta-shales that we have measured (garnet-mica schists from the Kangmar Dome) do not have especially low $\delta^{44}\text{Ca}$.

3.5.2 The potential role of garnet

An as yet unresolved issue is the role that garnet plays in the isotopic systematics of Mg and Ca. Equilibrium garnet in eclogite has been shown to be isotopically light with respect to Mg (W.-Y. Li, F.-Z. Teng, Xiao, & Huang, 2011). The effects on Ca are as of yet unknown. I note that one sample, the Kangmar schist 05DLB-17, has particularly aberrant Ca and Mg isotopic compositions ($\delta^{26}\text{Mg}$ of -2.62‰ , and $\delta^{44}\text{Ca}$ of 05DLB-17 = $+2.81\text{‰}$; the latter is heavier than the range yet observed for any other natural sample). Based on field relations and mineralogy, this schist is thought to be from the same lithologic unit as the other Kangmar schist sample, 05DLB-18, which is isotopically indistinguishable from BSE. The major textural difference between the two samples is porphyroblast size. 05DLB-17 contains abundant large garnets, and it is possible that the sample I processed for analysis was too small and contained a disproportionate amount of garnet.

Mg isotopic analyses of eclogite whole rocks of sufficient size suggests that the isotopic signal of the source is preserved (W.-Y. Li, F.-Z. Teng, Xiao, & Huang, 2011), but such may not be the case during anatexis. If residual garnet has isotopically light (e.g. negative) $\delta^{26}\text{Mg}$, it could drive melts toward high (positive) $\delta^{26}\text{Mg}$. The Miocene tuffs and Mesozoic granites exhibit small positive $\delta^{26}\text{Mg}$. We have previously suggested that the origin of heavy $\delta^{26}\text{Mg}$ in granitoids is from anatexis of pelites or metapelites, which inherit the signature

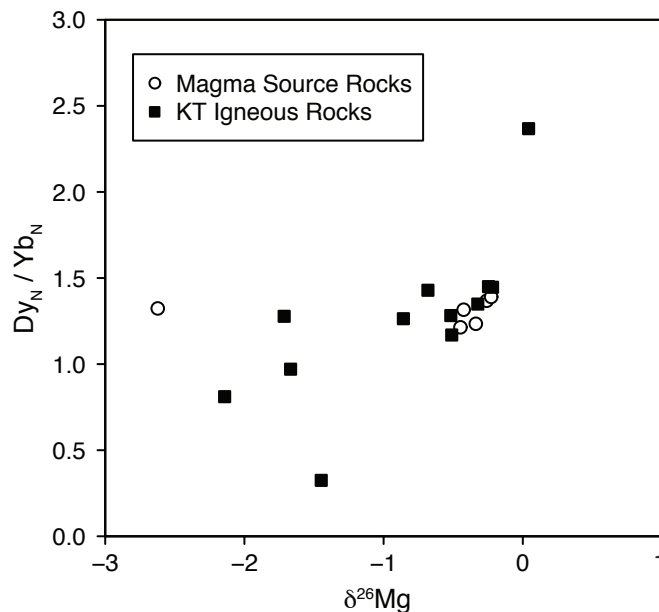


Figure 3.8: Dy_N/Yb_N (chondrite-normalized Dy/Yb; McDonough and Sun, 1995) vs $\delta^{26}\text{Mg}$. Dy/Yb ratios are a proxy for degree of fractionation within the HREE (which can be a result of residual source garnet). Regardless of Dy/Yb, the majority of samples have BSE-equivalent or lighter than BSE Mg (e.g. $\delta^{26}\text{Mg} < -0.25$). Additionally, the majority of igneous rocks (solid squares) are not offset to heavy $\delta^{26}\text{Mg}$ with respect to potential source rocks (open circles) as might be expected of garnet-derived magmas; the one exception is the crustal 2-mica granite 05DLB-23, characterized by both high Dy/Yb and heavy $\delta^{26}\text{Mg}$; this sample therefore could have derived its Mg isotopic characteristics from anatexis with residual garnet (it is possible that other igneous rocks in the suite could have experienced similar petrogenesis, but were overprinted by subsequent assimilation).

from surface weathering. An alternative, but compatible, hypothesis is that granites are isotopically heavy with respect to $\delta^{26}\text{Mg}$ if they are generated with residual garnet. In this regard, I note that there is a relationship between Mg isotopes and Dy/Yb, the latter an indicator of the presence of garnet in a magma source (Figure 3.8). However, as shown in Figure 3.7c and Figure 3.8, most granitic and volcanic samples in this study have low $\delta^{26}\text{Mg}$; the notable exception is the 190 Ma muscovite granite 05DLB-23.

3.5.3 A comment on Jiding Ophiolite Ca, Mg isotopic compositions and implications

The ophiolite samples are representative of depleted arc mantle in terms of their Sr and Nd isotopes, but distinct from the mantle in terms of their Ca and Mg isotopes. One possible explanation for characteristics of the ophiolite samples is growth of secondary, low-Mg, Ca-carbonate (which is present in thin section in the pillow basalt, 05DLB-10). Electron microprobe analyses indicate the composition of both vein and matrix carbonate is relatively

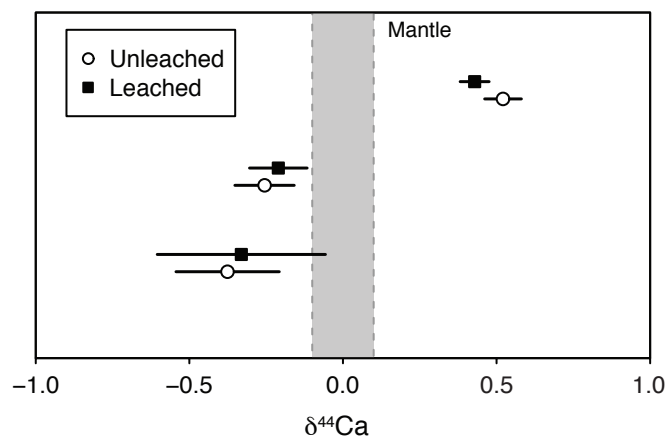


Figure 3.9: Comparison of leached and unleached Jiding Ophiolite samples; gray field indicates $\delta^{44}\text{Ca}$ mantle. Leaching was carried out for 24 hours in room temperature 1 N acetic acid (derived from SEASTAR™ Glacial acetic stock). Liquids were separated from solids by multiple centrifugations; solids were dried down and processed following procedures in section 3.3.1.

homogeneous and almost entirely calcic (total Mg wt % ranges from 0.1 - 0.4, total Ca wt % from 37.0 - 39.8 wt %).

In order to evaluate the effect of Ca-rich veins on the bulk isotopic composition of the ophiolites, fine powders were leached to dissolve carbonate fractions. Results from the leaching experiments are shown in Figure 3.9. In all cases, the shift between leached and unleached values is small; leached and unleached pairs are within error, although the leached samples are all offset towards mantle/BSE relative to the unleached samples. This could suggest that while secondary carbonate veins do modify the bulk-rock values, the majority of the signal is present in the non-leached (presumably silicate) portion of the rock, possibly incorporated during alteration.

The high $\delta^{44}\text{Ca}$ of the pillow basalt could be a result of exchange with seawater ($\delta^{44}\text{Ca} \sim +1$) during sub-seafloor hydrothermal alteration. This possibility is significant because it means that seawater Ca could be returned to the mantle by subduction, or contributed to arc magmas during subduction. This is consistent with observations of non-mantle/BSE Ca in Hawaiian magmas (S. Huang et al., 2011), although - in contrast to the conclusions of S. Huang et al. (2011) - the Ca need not be returned to the mantle wholly as carbonate, but could additionally be returned by subducting altered silicate phases.

3.6 Conclusions

This study investigates the use of Ca and Mg isotopes as tools in exploring the petrogenesis of crustally-derived granitic rocks. I use Sr and Nd isotopic data as a measure of the extent of involvement of older crustal rocks in magma genesis, and use the mass-dependent stable

isotopic variations of Mg ($\delta^{26}\text{Mg}$) and both mass-dependent and radiogenic isotopic variations of Ca ($\delta^{44}\text{Ca}$; ε_{Ca}) to investigate potential source lithologies. The data show that igneous rock samples that have mantle-like Sr and Nd isotopic compositions also typically have mantle-like Ca and Mg isotopic compositions. Rocks with strong crustal signatures of Sr and Nd isotopes (all with $\varepsilon_{\text{Nd}} < -5$) have variable Ca and Mg isotopic compositions that reflect the variability in crustal lithologies with respect to these isotopes, and the fact that the magmas were generated by large scale crustal melting or extensive crustal assimilation by mantle derived magmas.

Knowledge of the full range of Ca and Mg isotopic compositions of crustal rocks is limited, but it is known that marine carbonates have $\delta^{26}\text{Mg}$ and $\delta^{44}\text{Ca}$ values that are lower than mantle, and it is plausibly inferred from available data that shales and their metamorphic equivalents tend to have high $\delta^{26}\text{Mg}$ paired with mantle-like or low $\delta^{44}\text{Ca}$ values. Carbonate and shale signatures are present in the Ca and Mg isotopic compositions of crustally-derived granites and silicic volcanic rocks from southern Tibet. The rock compositions do not show evidence for extensive assimilation of carbonate, so it may be that the “carbonate” Ca isotope signal comes from a small carbonate component mixed with pelitic rocks. Seawater is distinctive in having a high $\delta^{44}\text{Ca}$, and the seawater Ca isotope signature may be present in hydrothermally-altered ophiolitic pillow basalts and in some primary arc magmas. Altered oceanic crust may be a way to introduce fractionated Ca back to the mantle, which is an additional mechanism beyond subduction of sediment.

Although many question about the behavior of Ca and Mg isotopes in geochemical cycles and systems remain (including the effects of garnet during metamorphism and anatexis), Ca and Mg isotopes are sensitive to different mineralogies and processes than “traditional” radiogenic isotopes (e.g. Sr, and Nd). These different sensitivities could make Ca and Mg isotopic analyses valuable complimentary tools in explorations of alteration, petrogenesis, assimilation, crustal evolution, and metamorphism.

Table 3.1: Major and trace elements.

Sample ID	QC-5	QC-11A	Nd-4-00	99-7-26-1b	05DLB-3	05DLB-4	05DLB-6
Lat	30.1358	30.3024	30.3577	30.5309	29.4022	29.3661	29.3843
Long	90.4599	90.5625	90.3414	90.7649	90.7174	90.7256	90.8724
Rock Type	granite	granulite	granite	granite	gabbro	diorite	granodiorite
Age	10.8	20	20	212.7	50	50	50
SiO ₂	73.00	71.36	70.90	76.50	50.95	59.60	64.50
TiO ₂	0.02	0.02	0.32	0.16	0.74	0.70	0.44
Al ₂ O ₃	15.00	13.81	15.20	12.90	17.44	16.89	16.24
FeO _T	0.56	4.12	4.02	2.98	8.91	6.21	3.02
MnO	0.05	0.94	0.06	0.04	0.17	0.12	0.06
MgO	0.02	0.19	0.51	0.27	6.52	2.69	1.16
CaO	0.38	1.22	1.62	0.59	9.82	5.54	2.71
Na ₂ O	2.58	2.78	3.29	2.84	3.19	4.20	3.14
K ₂ O	8.19	4.53	5.66	4.24	0.37	2.35	6.36
P ₂ O ₅	0.04	0.07	0.07	0.17	0.26	0.24	0.12
Sum	99.90	99.04	100.18	100.24	98.36	98.54	97.74
LOI	0.25		0.32	0.94	1.13	0.42	0.62
Mg#	0.06	0.08	0.18	0.14	0.57	0.44	0.41
Ni	4.00	107.47			44.20	7.20	12.80
Cr	0.00	385.25	0.00	0.00	141.70	10.00	11.60
V		11.95	28.88	11.00	242.00	140.60	57.30
Ga	16.00	15.74	18.62	20.00	17.40	17.60	15.20
Cu	1.70	107.17	11.73		21.90	47.20	5.70
Zn	11.00	17.03		41.00	87.30	76.10	41.90
La	10.70	65.33	66.54	16.10	7.51	18.18	24.30
Ce	22.20	134.15	100.75	39.00	16.65	38.01	52.65
Pr	2.40	14.06	10.77	3.90	2.38	4.90	6.41
Nd	9.00	47.70	33.62	14.40	10.78	19.99	23.59
Sm	2.40	9.45	3.60	3.41	2.61	4.24	4.45
Eu	0.56	0.59	0.94	0.26	1.07	1.09	1.03
Gd	2.20	9.40	2.69	3.13	2.57	3.81	3.49
Tb	0.40	2.63	0.39	0.68	0.41	0.59	0.55
Dy	2.90	30.37	2.52	4.07	2.37	3.54	3.14
Ho	0.50	11.28	0.54	0.78	0.48	0.71	0.62
Er	1.70	47.32	1.83	2.24	1.27	1.95	1.70
Tm	0.30	8.74	0.32	0.37	0.18	0.29	0.27
Yb	2.00	62.61	2.08	2.33	1.11	1.85	1.67
Lu	0.29	11.11	0.30	0.31	0.17	0.30	0.26
Ba	361.00	498.62	1200.00	134.00	139.47	486.85	1810.24
Th		68.69	41.58	18.70	0.34	6.71	15.17
Nb	23.00	9.38	22.39	13.50	1.09	4.90	7.27
Y	18.00	268.82	18.76	23.00	11.95	19.13	16.72
Hf		4.14			0.77	4.36	3.49
Ta		0.20			0.05	0.65	0.59
U		8.51	4.41	3.95	0.14	1.49	3.53
Pb		50.56	5.24	87.00	3.29	16.65	18.79
Rb	599.00	220.55	427.52	415.00	3.39	57.20	148.92
Cs		3.27			0.51	4.40	4.70
Sr	115.00	153.94	381.68	62.00	696.27	594.22	581.52
Sc		15.69			28.47	14.46	6.32
Zr	27.00	128.97	256.74	78.00	26.40	165.72	135.50

Table 3.1: Continued

Sample ID	05DLB-7	05DLB-8	05DLB-9	05DLB-10	05DLB-11	05DLB-14
Lat	30.1005	29.1123	29.1163	29.1586	29.1307	28.6852
Long	90.5433	88.4098	88.4062	89.0328	88.9936	89.6327
Rock Type	granite	gabbro	microgabbro	pillow lava	harzburgite	garnet mica schist
Age	53	128	128	128	128	Carboniferous
SiO ₂	75.52	50.50	52.55	48.15	39.24	59.91
TiO ₂	0.01	1.04	0.94	1.10	0.01	0.86
Al ₂ O ₃	13.32	15.48	16.44	15.46	0.88	20.67
FeO _T	0.78	8.81	7.90	8.98	7.52	5.94
MnO	0.05	0.19	0.13	0.14	0.09	0.09
MgO	0.02	7.84	6.68	5.01	37.47	1.32
CaO	0.33	8.37	6.53	10.67	0.17	0.74
Na ₂ O	4.09	3.87	5.35	3.56	0.01	1.14
K ₂ O	4.43	0.30	0.20	0.68	0.00	3.34
P ₂ O ₅	0.02	0.09	0.08	0.15	0.00	0.13
Sum	98.57	96.49	96.81	93.90	85.41	94.14
LOI	0.32	2.97	2.87	5.14	13.24	4.63
Mg#	0.04	0.61	0.60	0.50	0.90	0.28
Ni	3.74	96.80	42.90	66.70	2172.38	18.18
Cr	6.06	282.90	97.20	198.00	2307.90	86.76
V	1.01	241.60	238.40	225.30	45.64	128.37
Ga	19.59	16.70	16.80	17.40	1.68	26.26
Cu	3.03	4.50	72.00	35.60	22.82	16.87
Zn	36.06	42.10	74.80	68.90	41.30	91.81
La	13.89	2.43	2.15	3.31	0.04	48.51
Ce	32.53	7.72	6.43	10.02	0.08	106.71
Pr	4.05	1.39	1.15	1.74	0.01	11.57
Nd	14.55	7.54	6.25	9.30	0.04	43.20
Sm	4.95	2.68	2.25	3.26	0.01	8.96
Eu	0.06	1.01	0.87	1.22	0.00	1.67
Gd	5.37	3.78	3.17	4.40	0.02	7.29
Tb	1.11	0.72	0.60	0.81	0.01	1.18
Dy	7.16	4.81	4.01	5.41	0.05	6.91
Ho	1.47	1.05	0.87	1.14	0.01	1.36
Er	4.11	2.92	2.43	3.15	0.05	3.62
Tm	0.61	0.43	0.35	0.45	0.01	0.51
Yb	3.75	2.65	2.18	2.75	0.06	3.19
Lu	0.56	0.42	0.34	0.42	0.01	0.49
Ba	27.69	3.98	6.86	11.84	0.93	478.77
Th	16.53	0.11	0.12	0.12	0.02	20.82
Nb	14.42	0.67	0.65	1.04	0.02	16.69
Y	42.31	26.46	22.23	29.44	0.35	33.12
Hf	2.92	2.06	1.75	2.43	0.01	5.50
Ta	1.65	0.05	0.20	0.07	0.00	1.13
U	3.68	0.05	0.04	0.05	0.01	3.28
Pb	32.38	0.16	0.38	2.21	-0.07	29.52
Rb	306.81	1.88	1.12	11.34	0.22	179.45
Cs	7.01	0.27	0.16	0.41	0.04	14.24
Sr	7.05	198.17	188.96	124.89	2.12	96.51
Sc	2.37	36.69	29.19	28.39	9.39	17.49
Zr	46.82	72.75	60.73	87.32	0.35	183.00

Table 3.1: Continued

Sample ID	05DLB-15	05DLB-17	05DLB-18	05DLB-19	05DLB-20
Lat	28.6833	28.6852	28.6852	29.7238	29.7414
Long	89.6468	89.6327	89.6327	89.7082	89.7751
Rock Type	granite gneiss	garnet mica schist	garnet mica schist	volcanic tuff	volcanic breccia
Age	508	Carboniferous	Carboniferous	12	12
SiO ₂	73.65	55.84	61.44	70.95	68.43
TiO ₂	0.23	0.54	0.69	0.33	0.32
Al ₂ O ₃	13.52	17.88	18.68	13.30	13.97
FeO _T	1.73	15.09	6.70	1.66	1.86
MnO	0.04	4.95	0.39	0.02	0.02
MgO	0.48	1.71	2.05	0.47	0.55
CaO	1.69	1.74	2.05	0.48	1.61
Na ₂ O	3.13	0.26	1.86	1.90	2.63
K ₂ O	4.48	1.07	3.64	8.57	5.74
P ₂ O ₅	0.06	0.13	0.09	0.13	0.14
Sum	99.01	99.22	97.59	97.82	95.27
LOI	0.46	0.34	1.82	0.61	2.44
Mg#	0.33	0.17	0.35	0.34	0.35
Ni	7.47	15.66	39.90	10.70	9.70
Cr	13.03	50.70	76.15	16.20	15.30
V	23.03	59.79	94.74	26.80	28.40
Ga	15.76	15.05	25.15	18.70	19.30
Cu	3.54	32.83	3.94	7.40	9.30
Zn	14.24	82.72	103.93	34.40	47.20
La	38.35	15.92	44.72	69.80	61.17
Ce	76.13	30.38	94.61	133.99	160.27
Pr	8.15	3.65	9.95	14.54	12.59
Nd	28.09	13.94	36.25	48.94	41.33
Sm	5.88	5.40	7.44	7.71	6.59
Eu	0.71	2.25	1.40	1.15	1.00
Gd	5.02	12.93	6.54	4.56	3.93
Tb	0.85	3.19	1.09	0.59	0.50
Dy	4.93	21.71	6.57	3.03	2.51
Ho	0.97	4.35	1.30	0.54	0.43
Er	2.61	12.06	3.46	1.42	1.11
Tm	0.39	1.80	0.51	0.22	0.18
Yb	2.41	10.98	3.16	1.40	1.16
Lu	0.39	1.58	0.48	0.22	0.18
Ba	481.65	240.26	1134.69	875.50	1105.73
Th	30.33	11.76	23.02	75.87	73.81
Nb	12.24	14.76	14.44	15.56	14.58
Y	26.27	116.54	33.11	15.40	11.33
Hf	4.41	3.70	4.85	6.26	6.11
Ta	1.38	1.28	1.14	1.22	1.13
U	5.48	1.63	2.84	6.75	6.38
Pb	30.23	4.16	19.21	64.34	65.65
Rb	265.08	55.17	194.96	471.86	378.81
Cs	10.12	2.37	13.93	8.77	20.28
Sr	80.81	35.93	73.66	213.54	504.42
Sc	5.39	21.74	17.49	3.47	4.21
Zr	142.39	127.73	163.19	221.99	217.72

Table 3.1: Continued

Sample ID	05DLB-21	05DLB-22	05DLB-23
Lat	29.7590	30.2213	30.3800
Long	89.8420	90.6343	90.9304
Rock Type	volcanic tuff	shoshonite	granite
Age	12	50	190
SiO ₂	67.81	51.75	73.45
TiO ₂	0.33	0.76	0.11
Al ₂ O ₃	14.72	19.33	14.27
FeO _T	2.10	5.97	0.67
MnO	0.04	0.14	0.02
MgO	0.56	1.99	0.15
CaO	2.30	4.53	0.39
Na ₂ O	3.05	5.23	2.84
K ₂ O	4.43	4.95	4.94
P ₂ O ₅	0.11	0.46	0.27
Sum	95.46	95.12	97.10
LOI	3.51	4.21	0.90
Mg#	0.32	0.37	0.28
Ni	10.40	7.98	1.50
Cr	8.28	6.46	5.10
V	30.50	89.89	3.50
Ga	19.09	19.29	21.50
Cu	11.21	48.99	11.00
Zn	60.40	88.27	43.70
La	56.78	86.31	11.84
Ce	111.73	162.68	23.86
Pr	11.52	17.29	3.07
Nd	37.93	61.62	11.02
Sm	6.04	11.70	3.33
Eu	0.89	2.82	0.36
Gd	3.74	9.41	3.33
Tb	0.51	1.37	0.61
Dy	2.70	7.38	3.08
Ho	0.50	1.33	0.46
Er	1.31	3.37	1.06
Tm	0.20	0.46	0.15
Yb	1.34	2.88	0.87
Lu	0.21	0.44	0.12
Ba	603.53	780.66	87.86
Th	63.87	39.31	8.77
Nb	14.36	25.52	30.19
Y	13.92	35.61	13.51
Hf	4.97	7.28	2.11
Ta	1.50	1.17	6.36
U	10.68	7.67	4.36
Pb	62.13	21.16	41.61
Rb	342.85	127.63	642.13
Cs	45.47	16.77	80.36
Sr	439.93	891.62	30.27
Sc	4.46	8.74	4.69
Zr	167.54	371.70	53.72

Table 3.2: Isotopic data.

sample ID	QC-5	QC-11A	Nd-4-00	99-7-26-1b	05DLB-3	05DLB-4
$\varepsilon_{Ca}^{(o)}$	2.93	1.06	1.32	0.73	0.96	1.27
\pm	0.34	0.41	0.91	0.32	0.47	1.02
$\varepsilon_{Ca}^{(t)}$	2.76	1.00	1.27	-0.40	0.96	1.25
\pm	0.34	0.41	0.91	0.32	0.47	1.02
$\delta^{44}Ca_{uncorrected}$	-0.82	-0.16	-0.11	-0.72	-0.32	-0.21
\pm	0.09	0.16	0.05	0.06	0.11	0.12
$\delta^{44}Ca_{BSE}$	-0.53	-0.06	0.02	-0.64	-0.22	-0.08
\pm	0.10	0.16	0.10	0.07	0.12	0.16
$\delta^{26}Mg_{DSM3}$	-1.67	-1.45	-2.14	-0.51	-0.68	-0.52
\pm	0.04	0.04	0.13	0.14	0.02	0.01
$\delta^{25}Mg_{DSM3}$	-0.87	-0.76	-1.09	-0.25	-0.35	-0.26
\pm	0.01	0.04	0.06	0.06	0.01	0.02
Rb (ppm)	133.90	171.40	550.24	395.00	2.09	50.81
Sr (ppm)	143.00	112.75	40.71	44.90	516.16	575.20
Rb/Sr	0.9364	1.5202	13.5151	8.7973	0.0040	0.0883
$^{87}Sr/^{86}Sr^{(o)}$	0.722247	0.711426	0.719809	0.778138	0.703905	0.704501
\pm	0.000006	0.000011	0.000007	0.000008	0.000044	0.000149
$^{87}Sr/^{86}Sr^{(t)}$	0.719992	0.710207	0.718911	0.720990	0.703895	0.704308
Sm (ppm)	4.89	3.99	2.38	2.70	1.90	3.64
Nd (ppm)	25.49	21.90	11.47	10.90	8.12	18.23
Sm/Nd	0.1918	0.1820	0.2075	0.2477	0.2343	0.1997
$^{147}Sm/^{144}Nd$	0.1208	0.1146	0.1307	0.1560	0.1476	0.1258
$f_{Sm/Nd}$	-0.3857	-0.4174	-0.3356	-0.2068	-0.2498	-0.3607
$\varepsilon_{Nd}^{(o)}$	-8.51	-8.15	-6.31	-13.20	4.93	4.20
\pm	1.07	0.09	0.09	0.07	0.10	0.12
$\varepsilon_{Nd}^{(t)}$	-8.41	-7.94	-6.14	-12.09	5.24	4.66

Table 3.2: Continued

sample ID	05DLB-6	05DLB-7	05DLB-8	05DLB-9	05DLB-10	05DLB-11
$\varepsilon_{Ca} (o)$	0.37	0.71	0.28	0.94	1.11	0.71
\pm	0.44	0.85	0.91	0.94	0.24	0.55
$\varepsilon_{Ca} (t)$	0.29	0.20	0.27	0.93	1.11	0.70
\pm	0.44	0.85	0.91	0.94	0.24	0.55
$\delta^{44}Ca_{uncorrected}$	-0.19	0.35	-0.40	-0.37	0.39	-0.25
\pm	0.20	0.15	0.14	0.02	0.06	0.00
$\delta^{44}Ca_{BSE}$	-0.15	0.42	-0.38	-0.27	0.50	-0.18
\pm	0.21	0.17	0.17	0.10	0.07	0.05
$\delta^{26}Mg_{DSM3}$	-0.86	-1.71	-0.45	-0.34	-0.43	-2.82
\pm	0.06	0.11	0.04	0.04	0.04	0.37
$\delta^{25}Mg_{DSM3}$	-0.45	-0.87	-0.23	-0.18	-0.22	-1.45
\pm	0.03	0.08	0.02	0.03	0.00	0.17
Rb (ppm)	128.24	316.86	1.88	1.12	11.34	0.22
Sr (ppm)	494.55	7.26	198.17	188.96	124.89	2.12
Rb/Sr	0.2593	43.6446	0.0095	0.0059	0.0908	0.1033
$^{87}Sr/^{86}Sr (o)$	0.705317	0.856558	0.704617	0.704182	0.704466	0.710742
\pm	0.000007	0.000024	0.000007	0.000007	0.000006	0.000008
$^{87}Sr/^{86}Sr (t)$	0.704804	0.764076	0.704569	0.704151	0.704000	0.710212
Sm (ppm)	12.06	3.61	2.68	2.25	3.26	0.01
Nd (ppm)	27.96	13.45	7.54	6.25	9.30	0.04
Sm/Nd	0.4312	0.2684	0.3561	0.3608	0.3504	0.3939
$^{147}Sm/^{144}Nd$	0.2716	0.1690	0.2141	0.2243	0.2273	0.2207
$f_{Sm/Nd}$	0.3805	-0.1407	0.0885	0.1401	0.1553	0.1220
$\varepsilon_{Nd} (o)$	0.18	-9.00	8.32	8.26	8.06	
\pm	0.10	0.08	0.51	0.15	0.16	
$\varepsilon_{Nd} (t)$	-0.30	-8.82	7.86	7.76	7.66	

Table 3.2: Continued

sample ID	05DLB-15	05DLB-17	05DLB-18	05DLB-19	05DLB-20	05DLB-21
$\varepsilon_{Ca} (0)$	2.35	4.97	1.73	0.96	0.52	0.56
\pm	0.22	0.82	0.97	0.03	1.21	0.39
$\varepsilon_{Ca} (t)$	1.28	4.95	1.67	0.81	0.49	0.54
\pm	0.22	0.82	0.97	0.03	1.21	0.39
$\delta^{44}Ca_{uncorrected}$	-0.29	2.31	-0.34	-0.52	-0.58	-0.34
\pm	0.04	0.31	0.22	0.22	0.02	0.13
$\delta^{44}Ca_{BSE}$	-0.06	2.81	-0.17	-0.42	-0.53	-0.29
\pm	0.05	0.32	0.24	0.22	0.12	0.13
$\delta^{26}Mg_{DSM3}$	-0.26	-2.62	-0.23	-0.25	-0.22	-0.32
\pm	0.01	0.28	0.01	0.04	0.03	0.07
$\delta^{25}Mg_{DSM3}$	-0.13	-1.34	-0.12	-0.12	-0.11	-0.16
\pm	0.02	0.13	0.00	0.02	0.03	0.01
Rb (ppm)	269.00	55.17	194.96	471.86	378.81	371.89
Sr (ppm)	79.63	35.93	73.66	213.54	504.42	418.99
Rb/Sr	3.3781	1.5358	2.6468	2.2097	0.7510	0.8876
$^{87}Sr/^{86}Sr (0)$	0.781114	0.767617	0.797289	0.711398	0.710865	0.707445
\pm	0.000008	0.000006	0.000007	0.000007	0.000008	0.000018
$^{87}Sr/^{86}Sr (t)$	0.714086	0.764538	0.791983	0.710335	0.710504	0.707070
Sm (ppm)	4.13	5.40	7.44	7.71	6.59	5.46
Nd (ppm)	26.38	13.94	36.25	48.94	41.33	46.40
Sm/Nd	0.1566	0.3874	0.2051	0.1575	0.1594	0.1177
$^{147}Sm/^{144}Nd$	0.0986	0.2440	0.1292	0.0992	0.1004	0.0741
$f_{Sm/Nd}$	-0.4986	0.2404	-0.3433	-0.4958	-0.4896	-0.6232
$\varepsilon_{Nd} (0)$	-12.11	-8.16	-16.19	-7.24	-8.52	-6.11
\pm	0.08	0.24	0.08	0.80	0.12	0.12
$\varepsilon_{Nd} (t)$	-5.74	-8.46	-15.76	-7.09	-8.38	-5.92

Table 3.2: Continued

sample ID	05DLB-22	05DLB-23	BCR-1	GSP-1	DSM3
$\varepsilon_{Ca} (0)$	0.67	3.29		5.72	
\pm	0.80	1.75		0.49	
$\varepsilon_{Ca} (t)$	0.63	1.52			
\pm	0.80	1.75			
$\delta^{44}Ca_{uncorrected}$	-0.35	-1.20		-1.02	
\pm	0.20	0.05		0.03	
$\delta^{44}Ca_{BSE}$	-0.29	-0.87		-0.45	
\pm	0.21	0.18		0.06	
$\delta^{26}Mg_{DSM3}$	-1.89	0.04	-0.22	0.02	-0.09
\pm	0.04	0.03	0.13	0.17	0.12
$\delta^{25}Mg_{DSM3}$	-0.98	0.03	-0.12	0.01	-0.05
\pm	0.01	0.01	0.07	0.08	0.06
Rb (ppm)	125.53	729.05			
Sr (ppm)	845.07	28.51			
Rb/Sr	0.1485	25.5694			
$^{87}Sr/^{86}Sr (0)$	0.706613	0.932350			
\pm	0.000010	0.000010			
$^{87}Sr/^{86}Sr (t)$	0.706326	0.770575			
Sm (ppm)	21.72	2.99			
Nd (ppm)	81.46	10.40			
Sm/Nd	0.2666	0.2877			
$^{147}Sm/^{144}Nd$	0.1679	0.1812			
$f_{Sm/Nd}$	-0.1463	-0.0788			
$\varepsilon_{Nd} (0)$	-0.74	-13.44			
\pm	0.12	0.12			
$\varepsilon_{Nd} (t)$	-0.55	-13.06			

Major elements in wt%; trace elements in ppm. Major and trace elements were analysed at the GeoAnalytical Lab at Washington State University. Sr and Nd isotopic analyses for this study were performed at the Center for Isotope Geochemistry at the University of California, Berkeley, following separation procedures in DePaolo and Daley (2000). Isotopic analyses were made over a period transitioning from one instrument to another; measurements on granites were made on a VG354 mass spectrometer while all other measurements were made on a Thermo Scientific Triton. Analytical procedures for measurements made on the VG354 are described in DePaolo and Daley (2000). For analyses performed on the Triton, Sr isotope ratios were normalized to $^{88}Sr/^{86}Sr = 0.1194$. Nd was measured as a metal without oxygen bleed, and Nd isotopes were normalized to $^{146}Nd/^{144}Nd = 0.7219$. Ce, Sm, and Pr interferences were monitored and potential corrections were negligible. Ca and Mg procedures are described in the main text. $\varepsilon_{Nd} (t)$ and $\varepsilon_{Ca} (t)$ age corrections for the Kangmar metasediments were made to 50 Ma.

Appendix A

Isenthalpic AFC modeling with alphaMELTS

AlphaMELTS is a scriptable, command-line executable interface that extends the functionality of the MELTS, pMELTS, and phMELTS thermodynamic calculation subroutines (Ghiorso & Sack, 1995; Asimow & Ghiorso, 1998; Ghiorso, Hirschmann, et al., 2002). Technical information on alphaMELTS can be found in P. M. Smith and Asimow (2005); the appendix of Thompson et al. (2007); Antoshechkina and Asimow (2010), Antoshechkina, Asimow, et al. (2010); and in documentation on the website: <http://magmasource.caltech.edu/alphamelts/>.

Phase 1 and 2 AFC modeling is performed with alphaMELTS in isenthalpic mode. The enthalpy balance is as in Reiners, Nelson, and Ghiorso (1995):

$$M_a \Delta H_f^a + M_a \int C_p^{la} dT^{la} + M_a \int C_p^{sa} dT^{sa} = M_c \Delta H_f^c + M_m \int C_p^m dT^m \quad (\text{A.1})$$

where M_m , M_a , and M_c are the masses of the magma, assimilate, and crystals, ΔH_f^a and ΔH_f^c are the latent heats of fusion of the assimilate and crystals, dT^{la} , dT^{sa} , and dT^m are the temperature changes of the liquid assimilate, solid assimilate, and magma, and C_p^{la} , C_p^{sa} , and C_p^m are the heat capacities of the liquid assimilate, solid assimilate, and magma. The enthalpy required to heat and melt assimilant (the left side of the equation) is balanced by enthalpy produced in cooling and crystallization (right side).

The MELTS family of algorithms, alphaMELTS included, are iterative. In the isenthalpic mode, iterations are performed by adding a fixed amount of assimilant to the existing system. In my modeling, this value is 0.5 g (added to a system of initially 100 g primitive magma). alphaMELTS then solves for the equilibrium phase assemblage, fractionates solids and lowers the temperature, and the remaining liquid evolves; this process is carried out at fixed pressure (e.g. isobaric). This is slightly in contrast to the method of Reiners, Nelson, and Ghiorso (1995), where iterations were performed by descending regular temperature intervals. As an initial test, I successfully reproduced the calculations of Reiners, Nelson, and Ghiorso

(1995) (allowing for slight variations due to differences in the modern version of the MELTS subroutines from those of 1995, and in initial enthalpy calculations).

The enthalpy balance (and its implementation by alphaMELTS) in Equation A.1 has several limitations. It requires a fixed assimilant composition and assumes that all heat goes to assimilated material; no heat is lost by diffusion, and the assimilant is wholly melted. One could envision a more sophisticated model where heat could be lost to thermal diffusion, and the change in enthalpy on the left side of Equation A.1 could be computed by heating and partially melting wall-rock; such models are in development, and have yielded promising initial results (e.g. the magma chamber simulator of Bohrson, Spera, Creamer, and Ghiorso, 2012; Creamer, Spera, Bohrson, and Ghiorso, 2012). However, at present no “packaged” software exists for these models, and they cannot be easily applied to a wide variety of systems.

To overcome these limitations, I ran my model using a range of assimilant compositions corresponding to different degrees of melting of mafic granulite (phase 1) and global average upper crust (phase 2), over a range of geotherms. The effects of varying the pressure of the phase 1 AFC process were also explored. Input parameters were systematically varied to produce an ensemble output. The entire process was run via a series of shell scripts, which, for each single model run, performed the following actions:

1. Partially melt the deep crust assimilant (the “Parent” granulite assimilant composition in Tables 1.3 and 1.4) to the correct F at the correct pressure and output a deep crust assimilant melts file.
2. Calculate the reference state of the deep crust assimilant (using the output from step 1 as input) and output a binary restart file for phase 1 assimilation.
3. Perform the phase 1 AFC calculations using an initial magma composition and the binary restart file created in step 2. Phase 1 AFC was allowed to continue until the liquid composition reached a specific Mg# (25 or 35). Output the liquid composition as a melts file.
4. Using the output from step 3 as input, isenthalpically decompress the liquid composition to 0.13 GPa. Output a liquid composition melts file.
5. Partially melt the shallow crust assimilant (the “Parent” upper crust assimilant composition in Tables 1.3 and 1.4) to the correct F and the correct pressure (always 0.13 GPa) and output a shallow crust assimilant melts file.
6. Calculate the reference state of the shallow crust assimilant (using the output from step 5 as input) and output a binary restart file for phase 2 assimilation.
7. Perform the phase 2 AFC calculations using the output from step 4 as the liquid composition and the binary restart file created in step 6. Phase 2 AFC data were truncated at 74 wt% SiO₂ and the model is complete.

Step 1 was carried out one of two ways. If possible, a single isobaric batch calculation was performed at the specified F value by alphaMELTS in phase-diagram mode. Alternatively, if that failed to converge, the system was walked down from superliquidus temperatures in batch mode (isobarically) until the correct F value was reached.

To perform the isenthalpic balance, an initial, reference state of the assimilant must be calculated in step 2. The reference enthalpy of the assimilant depends on the initial temperature of the assimilant and the phase assemblage (and is therefore dependent on pressure and the assumed geotherm). Ideally, I would have alphaMELTS calculate the enthalpy and/or stable phase assemblage at the desired temperature and pressure (250, 350, or 450° C for phase 1 assimilation), but in practice, subsolidus computations of non-mantle composition didn't generally converge. As when step (1) failed to converge with a batch calculation, to approximate the initial enthalpy, I started with a superliquidus assimilant composition and decreased its temperature isobarically toward its solidus in batch mode (in some cases, a combination approach could produce the best results). alphaMELTS was usually capable of reaching near-solidus compositions (liquid mass is <0.5 wt% of initial mass) at temperatures above those desired (600–900° C, depending on pressure and volatile content), and at this point the assimilant temperature was simply set to its desired value, and a binary restart file output for use in the assimilation calculations. Implicit in this method is the assumption that the near-solidus phase assemblage is representative of the subsolidus assemblage at temperatures several hundred degrees lower; any changes between the two will introduce a small error in the enthalpy calculation. However, the models were run over a range of temperatures, and the differences in enthalpy associated with a change in initial temperature from 250 to 450° C, for instance, are larger than any error introduced by approximation of the initial phase assemblage. Moreover, this treatment of enthalpy balance is an approximation in that it does not compute the enthalpy associated with partially melting an assimilant. It does, however, correctly simulate fundamental first order behavior: lower temperature assimilants result in more rapid cooling of the intruding magma, and less assimilation (the temperature sensitivity of model output is shown in Figure 1.12).

Phase 1 assimilation was performed in step 3 in the isenthalpic mode. The initial temperature of the parent magma was taken to be 1370° C (calculated from SFVF geothermometry and geobarometry estimates of 1440° C at 2.55 GPa for primitive SFVF magmas, assuming an adiabatic temperature decrease of $\sim 1.1^\circ$ C/km to phase 1 pressures; section 1.6.1). At this temperature, the parent magma was above its liquidus, and the model liquid initially gained mass as it assimilated and cooled. Assimilation proceeded until the liquid had evolved to Mg# = 25 or 35 where the $^{87}\text{Sr}/^{86}\text{Sr}$ was sufficiently low to explain the most unradiogenic samples in our suite (discussed in more detail below).

In between the phase 1 and phase 2 AFC processes, the liquid was lifted from deep to shallow pressure (step 4). This was accomplished using alphaMELTS in the isentropic mode by iterating in steps of –10 bar. No assimilation occurred during this decompression. The temperature decreased, but at 0.13 GPa, the liquid was slightly above its solidus; thus when the AFC calculations resumed, there were usually a few aberrant iterations while the liquid composition cooled and equilibrated.

Steps 5 through 7 are similar to steps 1 through 3, but for the upper crust assimilant and shallow assimilation. In practice, convergence in Steps 5 and 6 was more difficult, as the assimilant composition was often SiO_2 and H_2O -rich, and the MELTS subroutines are not well calibrated for these compositions.

Each time alphaMELTS was run (once in each of the 7 steps), output at each iteration was generated, including: pressure, temperature, element and isotope abundances for the residual liquid, element and isotope abundances for each solid phase, chemical formulae and partition coefficients for each solid phase, and masses and densities of the liquid and the solid phases. Output files were parsed by shell scripts.

Input variables were systematically varied over geologically reasonable ranges to produce a series of runs that constitute an ensemble; the input variables are detailed in Table A.1. Using the batch-file capability of alphaMELTS, an entire ensemble could be executed automatically, although the first time each ensemble was run, output was checked to ensure that alphaMELTS was correctly converging.

Major element output from the model is shown in Figure 1.6 (for an ensemble including runs with phase 1 pressures of 0.40 and 0.55 GPa only). The output is shown in simplified form (as two lines showing the range expressed in the model) so as to better display the actual data. Full major element results are shown in Figure A.1 for an ensemble including phase 1 pressures of 0.20, 0.40, 0.55, and 0.70 GPa. In terms of major elements, varied input constraints generally made little differences in the shapes of the differentiation trends; exceptions are for those elements compatible in pressure-sensitive phases, such as Al_2O_3 in plagioclase.

Although I modeled phase 1 AFC up to 0.70 GPa (shown in blue lines in Figure A.1) as a possible limiting case, it predicted Al_2O_3 contents that were higher than those observed in the SFVF; thus it is not included in my analysis in the main text. Model runs at phase 1 pressures at 0.20 GPa (green lines in Figure A.1) were consistent with the lowest Al_2O_3 contents in SFVF magmas; however, they produced prominent Eu depletions not observed in SFVF magmas. This depth (~ 7.5 km) is also shallower than the storage depth inferred for Colorado Plateau granulite xenoliths (Wendlandt, Depaolo, & Baldrige, 1996), and I exclude these runs from my analysis in the main text.

Model parameters such as pressures and temperatures are constrained by xenoliths and geophysical data (discussed in Section 1.5). One important parameter for which constraints are less apparent is the number of model iterations the system should be allowed to experience in phase 1 AFC before isentropic lifting. Isotopes provide some chemical constraints on the extent of AFC: Pb and Sr isotopes suggest that the most unradiogenic compositions are not reached until the magma has evolved to around 1.5–2.5 wt% MgO (Mg# of 25–35; Figure 1.10). Therefore, models were run to either Mg# = 25 or 35 before liquids were isentropically lifted. At 0.40–0.55 GPa, this equates to a change in liquid density from an initial 2700–2750 kg/m^3 to 2500 or 2600 kg/m^3 (for Mg# = 25, and 35, respectively). Although density contrast is only one aspect of a magma's ability to ascend to shallower levels (e.g. Jellinek & DePaolo, 2003), these evolved values are consistently lower than the surrounding crust (2750 kg/m^3 ; Bashir et al., 2011), suggesting they will be buoyant.

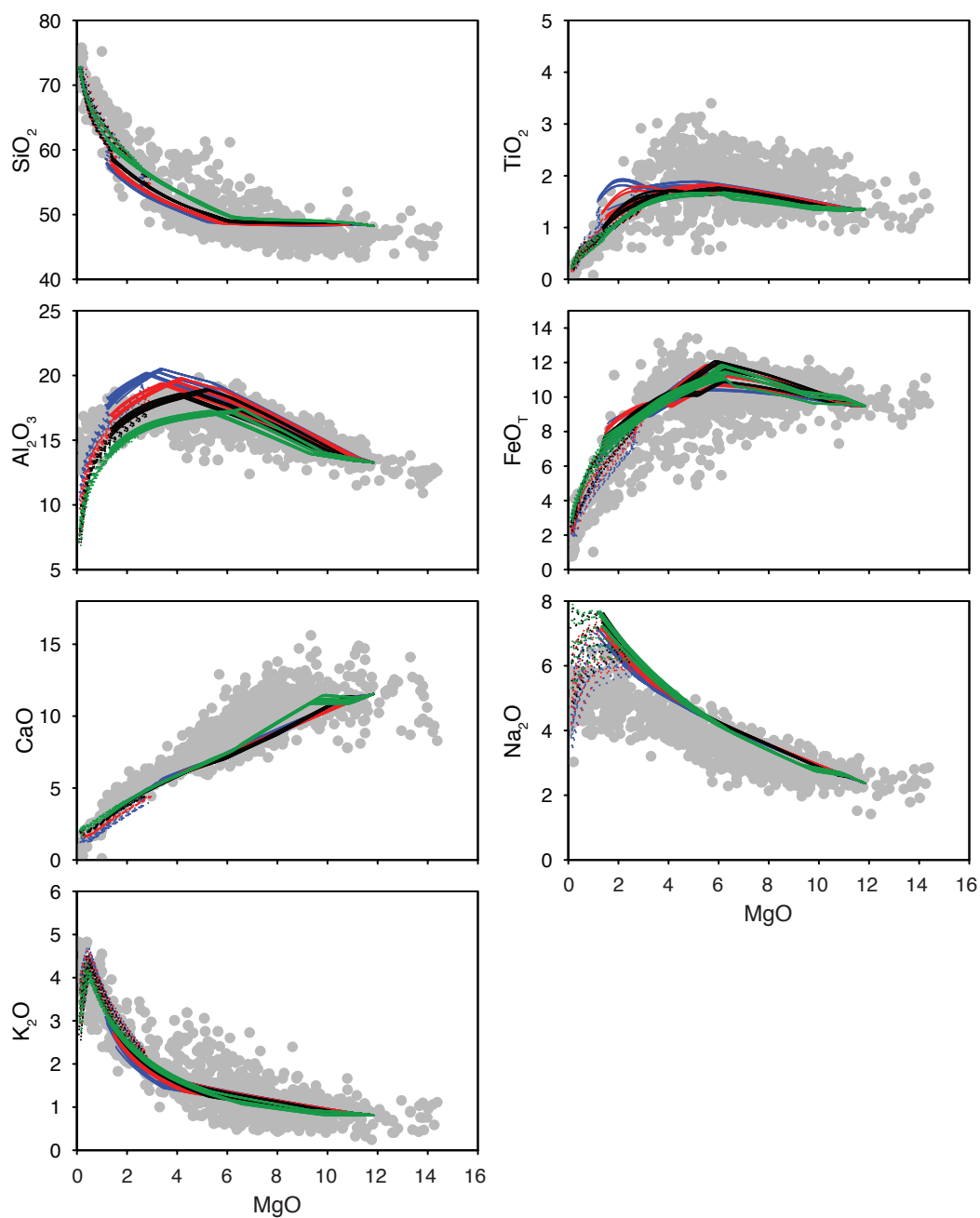


Figure A.1: Major element covariation diagrams for full AFC ensemble results. The SFVF data (corresponding to data in Figure 1.6) are shown in grey. Line colors indicate phase 1 pressure: green = 0.20 GPa; black = 0.40 GPa; red = 0.55 GPa; blue = 0.70 GPa. Solid lines are phase 1 trajectories, dotted lines are phase 2 trajectories. Prominent kinks in Al_2O_3 are when plagioclase becomes a crystallizing phase.

Table A.1: Input parameters for SFVF AFC modeling

^a P (Gpa)	^b F	^c T (° C)	^d extent (Mg#)
0.20 / 0.13	0.2 / 0.6	250 / 60	25
0.40 / 0.13	0.4 / 0.8	350 / 100	35
0.55 / 0.13	0.6 / 1.0	450 / 140	
0.70 / 0.13			

^aVariables for phase 1 and 2 processes are varied in tandem; for example, 0.20 / 0.13 indicates a model run wherein the phase 1 assimilation occurs at 0.20 GPa and the phase 2 at 0.13 GPa.

^bF refers to degrees of melting of the granulite / upper crust assimilants.

^cTemperature at which the phase 1 / phase 2 assimilations are carried out.

^dEach combination of parameters is allowed to assimilate to two different extents during phase 1, which are tracked by Mg#.

Each set of input parameters in the above table is combined with every other set, resulting in an ensemble of 72 possible runs total.

Bibliography

- Aciego, S. M. (2006). *New approaches to quaternary geochronology: U-Th/He dating of basalt and stable isotope mapping of polar glaciers* (Doctoral dissertation, University of California, Berkeley).
- Aciego, S. M., DePaolo, D. J., Kennedy, B. M., Lamb, M. P., Sims, K. W. W., & Dietrich, W. E. (2007). Combining [He-3] cosmogenic dating with U-Th/He eruption ages using olivine in basalt. *Earth and Planetary Science Letters*, *254*(3-4), 288–302. doi:10.1016/j.epsl.2006.11.039
- Aciego, S. M., Jourdan, F., DePaolo, D. J., Kennedy, B. M., Renne, P. R., & Sims, K. W. W. (2010). Combined U-Th/He and $^{40}\text{Ar}/^{39}\text{Ar}$ geochronology of post-shield lavas from the Mauna Kea and Kohala volcanoes, Hawaii. *Geochimica et Cosmochimica Acta*, *74*(5), 1620–1635. doi:10.1016/j.gca.2009.11.020
- Aciego, S. M., Kennedy, B. M., DePaolo, D. J., Christensen, J. N., & Hutcheon, I. (2003). U-Th/He age of phenocrystic garnet from the 79 AD eruption of Mt. Vesuvius. *Earth and Planetary Science Letters*, *216*(1-2), 209–219.
- Aitchison, J. C., Davis, A. M., Abrajevitch, A. V., Ali, J. R., Liu, J., Luo, H., . . . Ziabrev, S. V. (2003). Stratigraphic and sedimentological constraints on the age and tectonic evolution of the Neotethyan ophiolites along the Yarlung Tsangpo suture zone, Tibet. In Y. Dilek & P. T. Robinsonm (Eds.), *Ophiolites in earth history* (Geological Society of London Special Publication, Vol. 218, pp. 147–164). Geological Society of London. doi:10.1144/GSL.SP.2003.218.01.09
- Aitchison, J. C., Davis, A. M., & Luo, H. (2002). New constraints on the India–Asia collision: the Lower Miocene Gangrinboche conglomerates, Yarlung Tsangpo suture zone, SE Tibet. *Journal of Asian Earth Sciences*, *21*(3), 251–263. doi:10.1016/S1367-9120(02)00037-8
- Alibert, C., Michard, A., & Albarede, F. (1986). Isotope and trace element geochemistry of Colorado Plateau volcanics. *Geochimica Et Cosmochimica Acta*, *50*(656), 2735–2750.
- Antoshechkina, P. M. & Asimow, P. D. (2010). Adibat_1ph 3.0 and the MAGMA website: educational and research tools for studying the petrology and geochemistry of plate margins. Abstract ED41B-0644 presented at 2010 Fall Meeting, American Geophysical Union (AGU), San Francisco, California, USA.
- Antoshechkina, P. M., Asimow, P. D., Hauri, E. H., & Luffi, P. I. (2010). Effect of water on mantle melting and magma differentiation, as modeled using Adibat_1ph 3.0. Abstract

- V53C-2264 presented at 2010 Fall Meeting, American Geophysical Union (AGU), San Francisco, California, USA.
- Asimow, P. D. & Ghiorso, M. S. (1998). Algorithmic modifications extending MELTS to calculate subsolidus phase relations. *American Mineralogist*, *83*(1), 1127–1132.
- Asmerom, Y. & Jacobsen, S. B. (1993). The Pb isotopic evolution of the Earth: inferences from river water suspended loads. *Earth and Planetary Science Letters*, *115*(1-4), 245–256. doi:10.1016/0012-821X(93)90225-X
- Baker, J., Bizzarro, M., Wittig, N., Connelly, J., & Haack, H. (2005). Early planetesimal melting from an age of 4.5662 Gyr for differentiated meteorites. *Nature*, *436*(7054), 1127–31. doi:10.1038/nature03882
- Barnes, C. G., Prestvik, T., Sundvoll, B., & Surratt, D. (2005). Pervasive assimilation of carbonate and silicate rocks in the Hortavær igneous complex, north-central Norway. *Lithos*, *80*(1–4), 179–199. doi:10.1016/j.lithos.2003.11.002
- Bashir, L., Gao, S. S., Liu, K. H., & Mickus, K. (2011). Crustal structure and evolution beneath the Colorado Plateau and the southern Basin and Range Province: Results from receiver function and gravity studies. *Geochemistry, Geophysics, Geosystems*, *12*(6), Q06008. doi:10.1029/2011GC003563
- Beard, B. L. & Johnson, C. M. (1997). Hafnium isotope evidence for the origin of Cenozoic basaltic lavas from the southwestern United States. *Journal of Geophysical Research-Solid Earth*, *102*(B9), 20149–20178.
- Beard, B. L., Johnson, C. M., Skulan, J. L., Nealson, K. H., Cox, L., & Sun, H. (2003). Application of Fe isotopes to tracing the geochemical and biological cycling of Fe. *Chemical Geology*, *195*(1-4), 87–117. doi:10.1016/S0009-2541(02)00390-X
- Bennett, V. C. & DePaolo, D. J. (1987). Proterozoic crustal history of the western United States as determined by neodymium isotopic mapping. *Geological Society of America Bulletin*, *99*, 674–685. doi:10.1130/0016-7606(1987)99<674
- Bird, P. (1979). Continental delamination and the colorado plateau. *Journal of Geophysical Research*, *84*(Nb13), 7561–7571.
- Bizzarro, M., Baker, H., J.and Haack, & Lundgaard, K. L. (2005). Rapid timescale for accretion and melting of differentiated planetesimals inferred from ^{26}Al - ^{26}Mg chronometry. *The Astrophysical Journal Letters*, *632*(1), L41–L44. doi:10.1086/497638
- Bloomfield, A. L. & Arculus, R. J. (1989). Magma Mixing in the San-Francisco Volcanic Field, Az - Petrogenesis of the Oleary Peak and Strawberry Crater Volcanics. *Contributions to Mineralogy and Petrology*, *102*(4), 429–453.
- Bohrson, W. A., Spera, F. J., Creamer, J. B., & Ghiorso, M. S. (2012). The magma chamber simulator: modeling compositional, temperature and mass variations in a composite magma-wallrock system. Abstract V11A-2729 presented at 2012 Fall Meeting, American Geophysical Union (AGU), San Francisco, California, USA.
- Borg, S. G., DePaolo, D. J., & Smith, B. M. (1990). Isotopic structure and tectonics of the central Transantarctic mountains. *Journal of Geophysical Research*, *95*(B5), 6647–6667. doi:10.1029/JB095iB05p06647

- Boulou-Bi, E. B., Poszwa, A., Leyval, C., & Vigier, N. (2010). Experimental determination of magnesium isotope fractionation during higher plant growth. *Geochimica Et Cosmochimica Acta*, *74*, 2523–2537. doi:10.1016/j.gca.2010.02.010
- Bowring, S. A. & Karlstrom, K. E. (1990). Growth, Stabilization, and Reactivation of Proterozoic Lithosphere in the Southwestern United-States. *Geology*, *18*(12), 1203–1206.
- Bradshaw, T. K., Hawkesworth, C. J., & Gallagher, K. (1993). Basaltic Volcanism in the Southern Basin and Range - No Role for a Mantle Plume. *Earth and Planetary Science Letters*, *116*(1-4), 45–62.
- Brenot, A., Cloquet, C., Vigier, N., Carignan, J., & France-Lanord, C. (2008). Magnesium isotope systematics of the lithologically varied Moselle river basin, France. *Geochimica Et Cosmochimica Acta*. doi:doi:10.1016/j.gca.2008.07.027
- Brookins, D. G. & Moore, R. B. (1975). Sr isotope initial ratios from the San Francisco volcanic field, Arizona. *Isochron/West*, *12*, 1–2.
- Bryant, B., Wooden, J. L., & Nealey, L. D. (2001). Geology, geochronology, geochemistry, and Pb-isotopic compositions of Proterozoic rocks, Poachie region, west-central Arizona - a study of the east boundary of the Proterozoic Mojave Crustal Province. U.S. Geological Survey Professional Paper 1639.
- Bryce, J. G., DePaolo, D. J., & Lassiter, J. C. (2005). Geochemical structure of the Hawaiian plume: Sr, Nd, and Os isotopes in the 2.8 km HSDP–2 section of Mauna Kea volcano. *Geochemistry Geophysics Geosystems*, *6*(9), Q09G18. doi:10.1029/2004GC000809
- Caro, G., Papanastassiou, D. A., & Wasserburg, G. J. (2010). ^{40}K – ^{40}Ca isotopic constraints on the oceanic calcium cycle. *Earth and Planetary Science Letters*, *296*(1-2), 124–132. doi:10.1016/j.epsl.2010.05.001
- Chadwick, J. P., Troll, V. R., Ginibre, C., Morgan, D., Gertisser, R., Waight, T. E., & Davidson, J. P. (2007). Carbonate Assimilation at Merapi Volcano, Java, Indonesia: Insights from Crystal Isotope Stratigraphy. *Journal of Petrology*, *48*(9), 1793–1812. doi:10.1093/petrology/egm038
- Chang, V. T. C. and Makishima, A. and Belshaw, N. S. and O’Nions, R. K. (2003). Purification of Mg from low-Mg biogenic carbonates for isotope ratio determination using multiple collector ICP-MS. *Journal of Analytical Atomic Spectrometry*, *18*(4), 296–301.
- Chen, W. & Arculus, R. J. (1995). Geochemical and isotopic characteristics of lower crustal xenoliths, San Francisco Volcanic Field, Arizona, USA. *Lithos*, *36*(3-4), 203–225.
- Chen, Z., Liu, Y., Hodges, K. V., Burchfiel, B. C., Royden, L. H., & Deng, C. (1990). The Kangmar Dome: A Metamorphic Core Complex in Southern Xizang (Tibet). *Science*, *250*(4987), 1552–1556.
- Chung, S.-L., Chu, M.-F., Zhang, Y., Xie, Y., Lo, C.-H., Lee, T.-Y., . . . Wang, Y. (2005). Tibetan tectonic evolution inferred from spatial and temporal variations in post-collisional magmatism. *Earth-Science Reviews*, *68*(3-4), 173–196. doi:10.1016/j.earscirev.2004.05.001
- Condie, K. C., Belousova, E., Griffin, W. L., & Sircombe, K. N. (2009). Granitoid events in space and time: Constraints from igneous and detrital zircon age spectra. *Gondwana Research*, *15*(3-4), 228–242. doi:10.1016/j.gr.2008.06.001

- Conway, F. M., Connor, C. B., Hill, B. E., Condit, C. D., Mullaney, K., & Hall, C. M. (1998). Recurrence rates of basaltic volcanism in SP cluster, San Francisco volcanic field, Arizona. *Geology*, *26*(7), 655–658.
- Conway, F. M., Ferrill, D. A., Hall, C. M., Morris, A. P., Stamatakos, J. A., Connor, C. B., . . . Condit, C. (1997). Timing of basaltic volcanism along the Mesa Butte Fault in the San Francisco Volcanic Field, Arizona, from Ar-40/Ar-39 dates: Implications for longevity of cinder cone alignments. *Journal of Geophysical Research-Solid Earth*, *102*(B1), 815–824.
- Cooper, J. L. & Hart, W. K. (1990). Mantle sources in the Arizona transition zone and global mantle heterogeneity. *Geology*, *18*, 1146–1149.
- Cousens, L. (1996). Magmatic evolution of Quaternary mafic magmas at Long Valley Caldera and the Devils Postpile, California: Effects of crustal contamination on lithospheric mantle-derived magmas. *Journal of Geophysical Research*, *101*(B12), 27, 673–27, 689.
- Creamer, J. B., Spera, F. J., Bohron, W. A., & Ghiorso, M. S. (2012). The magma chamber simulator: modeling the impact of wall rock composition on mafic magmas during Assimilation-Fractional Crystallization. Abstract V11C-2771 presented at 2012 Fall Meeting, American Geophysical Union (AGU), San Francisco, California, USA.
- Crisp, J. A. (1984). Rates of magma emplacement and volcanic output. *Journal of Volcanology and Geothermal Research*, *20*, 177–211.
- Dasgupta, R., Hirschmann, M. M., & Smith, N. D. (2007). Partial Melting Experiments of Peridotite + CO₂ at 3 GPa and Genesis of Alkalic Ocean Island Basalts. *Journal of Petrology*, *48*(11), 2093–2124. doi:10.1093/petrology/egm053
- Demidjuk, Z., Turner, S., Sandiford, M., George, R., Foden, J., & Etheridge, M. (2007). U-series isotope and geodynamic constraints on mantle melting processes beneath the Newer Volcanic Province in South Australia. *Earth and Planetary Science Letters*, *261*(3-4), 517–533. doi:10.1016/j.epsl.2007.07.006
- DePaolo, D. J. (1981). Trace-element and isotopic effects of combined wallrock assimilation and fractional crystallization. *Earth and Planetary Science Letters*, *53*(2), 189–202.
- DePaolo, D. J. (2004). Calcium Isotopic Variations Produced by Biological, Kinetic, Radiogenic and Nucleosynthetic Processes. In C. M. Johnson, B. L. Beard, & F. Albarede (Eds.), *Geochemistry of non-traditional stable isotopes* (Chap. 8, Vol. 55, pp. 255–288). Mineralogical Society of America.
- DePaolo, D. J. (1981). A Neodymium and Strontium Isotopic Study of the Mesozoic Calc-Alkaline Granitic Batholiths of the Sierra Nevada and Peninsular Ranges, California. *Journal of Geophysical Research*, *86*(B11), 10470–10488.
- DePaolo, D. J., Bryce, J. G., Dodson, A., Shuster, D. L., & Kennedy, B. M. (2001). Isotopic evolution of mauna loa and the chemical structure of the hawaiian plume. *Geochemistry Geophysics Geosystems*, *2*, 1044. doi:10.1029/2000GC000139
- DePaolo, D. J. & Daley, E. E. (2000). Neodymium isotopes in basalts of the southwest basin and range and lithospheric thinning during continental extension. *Chemical Geology*, *169*(1-2), 157–185. doi:10.1016/S0009-2541(00)00261-8

- DePaolo, D. J., Linn, A. M., & Schubert, G. (1991). The Continental Crustal Age Distribution - Methods of Determining Mantle Separation Ages from Sm-Nd Isotopic Data and Application to the Southwestern United-States. *Journal of Geophysical Research-Solid Earth and Planets*, 96(B2), 2071–2088.
- DePaolo, D. J. & Stolper, E. M. (1996). Models of hawaiian volcano growth and plume structure: implications of results from the hawaii scientific drilling project. *Journal of Geophysical Research-Solid Earth*, 101(B5), 11643–11654.
- Dhuime, B., Hawkesworth, C. J., Cawood, P. A., & Storey, C. D. (2012). A change in the geodynamics of continental growth 3 billion years ago. *Science*, 335(6074), 1334–6. doi:10.1126/science.1216066
- Dubois-Cote, V., Hebert, R., Dupuis, C., Wang, C., Li, Y., & Dostal, J. (2005). Petrological and geochemical evidence for the origin of the Yarlung Zangbo ophiolites, southern Tibet. *Chemical Geology*, 214(3-4), 265–286. doi:10.1016/j.chemgeo.2004.10.004
- Durrani, B. A., Doser, D. I., Keller, G. R., & Hearn, T. M. (1999). Velocity structure of the upper crust under the San Francisco volcanic field, Arizona. *Bulletin of the Seismological Society of America*, 89(1), 239–249.
- Elkins-Tanton, L. T. (2005). Continental magmatism caused by lithospheric delamination. In G. R. Foulger, J. H. Natland, D. C. Presnall, & A. D. L. L. (Eds.), *Plates, plumes, and paradigms* (Geological Society of America Special Volume, Vol. 388, pp. 449–461). Geological Society of America. doi:10.1130/2005.2388(27)
- Everson, J. E. (1979). *Regional variations in the lead isotopic characteristics of late cenozoic basalts from the southwestern United States* (Doctoral dissertation, California Institute of Technology).
- Fantle, M. S. & DePaolo, D. J. (2007). Ca isotopes in carbonate sediment and pore fluid from ODP Site 807A: The Ca²⁺(aq)–calcite equilibrium fractionation factor and calcite recrystallization rates in Pleistocene sediments. *Geochimica Et Cosmochimica Acta*, 71, 2524–2546. doi:10.1016/j.gca.2007.03.006
- Farley, K. A., Kohn, B. P., & Pillans, B. (2002). The effects of secular disequilibrium on (U-Th)/He systematics and dating of Quaternary volcanic zircon and apatite. *Earth and Planetary Science Letters*, 201(1), 117–125.
- Farmer, G. L. & DePaolo, D. J. (1983). Origin of Mesozoic and Tertiary granite in the western United States and implications for pre-Mesozoic crustal structure 1. Nd and Sr isotopic studies in the geocline of the northern Great Basin. *Journal of Geophysical Research*, 88(B4), 3379–3401.
- Freda, C., Gaeta, M., Misiti, V., Mollo, S., Dolfi, D., & Scarlato, P. (2008). Magma–carbonate interaction: An experimental study on ultrapotassic rocks from Alban Hills (Central Italy). *Lithos*, 101(3–4), 397–415. doi:10.1016/j.lithos.2007.08.008
- Gaetani, G. A., Grove, T. L., & Bryan, W. B. (1993). The influence of water on the petrogenesis of subduction-related igneous rocks. *Nature*, 365, 332–334. doi:10.1038/365332a0
- Gayer, E., Mukhopadhyay, S., & Meade, B. J. (2008). Spatial variability of erosion rates inferred from the frequency distribution of cosmogenic He-3 in olivines from Hawaiian river sediments. *Earth and Planetary Science Letters*, 266(3-4), 303–315.

- Geldmacher, J., Hoernle, K., Bogaard, P., Duggen, S., & Werner, R. (2005). New $^{40}\text{Ar}/^{39}\text{Ar}$ age and geochemical data from seamounts in the Canary and Madeira volcanic provinces: Support for the mantle plume hypothesis. *Earth and Planetary Science Letters*, *237*(1-2), 85–101. doi:10.1016/j.epsl.2005.04.037
- Ghiorso, M. S., Hirschmann, M. M., Reiners, P. W., & Kress, V. C. (2002). The pMELTS: A revision of MELTS for improved calculation of phase relations and major element partitioning related to partial melting of the mantle to 3 GPa. *Geochemistry, Geophysics, Geosystems*, *3*(5), 1–35. doi:10.1029/2001GC000217
- Ghiorso, M. S. & Sack, R. O. (1995). Chemical mass transfer in magmatic processes IV. A revised and internally consistent thermodynamic model for the interpolation and extrapolation of liquid-solid equilibria in magmatic systems at elevated temperatures and pressures. *Contributions to Mineralogy and Petrology*, *119*(2-3), 197–212. doi:10.1007/BF00307281
- Granet, M., Wilson, M., & Achauer, U. (1995). Imaging a mantle plume beneath the French Massif Central. *Earth and Planetary Science Letters*, *136*(3-4), 281–296. doi:10.1016/0012-821X(95)00174-B
- Green, T. H., Blundy, J. D., Adam, J., & Yaxley, G. M. (2000). SIMS determination of trace element partition coefficients between garnet, clinopyroxene and hydrous basaltic liquids at 2–7.5 GPa and 1080–1200 °C. *Lithos*, *53*(3-4), 165–187. doi:10.1016/S0024-4937(00)00023-2
- Grove, T. L., Holbig, E. S., Barr, J. A., Till, C. B., & Krawczynski, M. J. (2013). Melts of garnet lherzolite: experiments, models and comparison to melts of pyroxenite and carbonated lherzolite. *Contributions to Mineralogy and Petrology*, *in press*.
- Guo, Z., Wilson, M., & Liu, J. (2007). Post-collisional adakites in south Tibet: Products of partial melting of subduction-modified lower crust. *Lithos*, *96*(1-2), 205–224. doi:10.1016/j.lithos.2006.09.011
- Gupta, S., Zhao, D., & Rai, S. S. (2009). Seismic imaging of the upper mantle under the Erebus hotspot in Antarctica. *Gondwana Research*, *16*(1), 109–118. doi:10.1016/j.gr.2009.01.004
- Halliday, A. N., Lee, D.-C., Tommasini, S., Davies, G. R., Paslick, C. R., Fitton, J. G., & James, D. E. (1995). Incompatible trace elements in OIB and MORB and source enrichments in the sub-oceanic mantle. *Earth and Planetary Science Letters*, *133*, 379–395.
- Hammersley, L. & DePaolo, D. J. (2006). Isotopic and geophysical constraints on the structure and evolution of the Clear Lake volcanic system. *Journal of Volcanology and Geothermal Research*, *153*(3-4), 331–356. doi:10.1016/j.jvolgeores.2005.12.003
- Handler, M. R., Baker, J., Schiller, M., Bennet, V. C., & Yaxley, G. M. (2009). Magnesium stable isotope composition of Earth's upper mantle. *Earth and Planetary Science Letters*. doi:10.1016/j.epsl.2009.03.031
- Hart, S. R. (1984). A large-scale isotope anomaly in the Southern Hemisphere mantle. *Nature*, *309*, 753–757. doi:10.1038/309753a0

- Hawkesworth, C. J., Dhuime, B., Pietranik, A. B., Cawood, P. A., Kemp, A. I. S., & Storey, C. D. (2010). The generation and evolution of the continental crust. *Journal of the Geological Society*, *167*(2), 229–248. doi:10.1144/0016-76492009-072
- Higuchi, H. & Nagasawa, H. (1969). Partition of trace elements between rock-forming minerals and the host volcanic rocks. *Earth and Planetary Science Letters*, *7*, 281–287.
- Hildreth, W., Halliday, A. N., & Christiansen, R. L. (1991). Isotopic and chemical evidence concerning the genesis and contamination of basaltic and rhyolitic magma beneath the Yellowstone Plateau Volcanic Field. *Journal of Petrology*, *32*, 63–138. doi:10.1093/petrology/32.1.63
- Hill, E., Wood, B. J., & Blundy, J. D. (2000). The effect of Ca-Tschemaks component on trace element partitioning between clinopyroxene and silicate melt. *Lithos*, *53*(3–4), 203–215. doi:10.1016/S0024-4937(00)00025-6
- Hippler, D., Buhl, D., Witbaard, R., Richter, D. K., & Immenhauser, A. (2009). Towards a better understanding of magnesium-isotope ratios from marine skeletal carbonates. *Geochimica Et Cosmochimica Acta*, *73*, 6134–6146. doi:10.1016/j.gca.2009.07.031
- Hirose, K. & Kushiro, I. (1993). Partial melting of dry peridotites at high pressures: Determination of compositions of melts segregated from peridotite using aggregates of diamond. *Earth and Planetary Science Letters*, *114*(4), 477–489. doi:10.1016/0012-821X(93)90077-M
- Hirschmann, M. M., Kogiso, T., Baker, M. B., & Stolper, E. M. (2003). Alkalic magmas generated by partial melting of garnet pyroxenite. *Geology*, *31*(6), 481–484. doi:10.1130/0091-7613(2003)031<0481
- Hofmann, A. W. (1988). Chemical differentiation of the Earth: the relationship between mantle, continental crust, and oceanic crust. *Earth and Planetary Science Letters*, *90*(3), 297–314. doi:10.1016/0012-821X(88)90132-X
- Hou, Z.-Q., Gao, Y.-F., Qu, X.-M., Rui, Z.-Y., & Mo, X.-X. (2004). Origin of adakitic intrusives generated during mid-Miocene east–west extension in southern Tibet. *Earth and Planetary Science Letters*, *220*(1–2), 139–155. doi:10.1016/S0012-821X(04)00007-X
- Huang, F., Glessner, J., Ianno, I., Lundstrom, C., & Zhang, Z. (2009). Magnesium isotopic composition of igneous rock standards measured by MC-ICP-MS. *Chemical Geology*, *268*, 15–23. doi:10.1016/j.chemgeo.2009.07.003
- Huang, S., Farkaš, J., & Jacobsen, S. B. (2011). Stable calcium isotopic compositions of Hawaiian shield lavas: Evidence for recycling of ancient marine carbonates into the mantle. *Geochimica et Cosmochimica Acta*, *75*(17), 4987–4997. doi:10.1016/j.gca.2011.06.010
- Humphreys, E., Hessler, E., Dueker, K., Farmer, G. L., Erslev, E., & Atwater, T. (2003). How Laramide-age hydration of North American lithosphere by the Farallon slab controlled subsequent activity in the western United States. *International Geology Review*, (March 2013), 37–41.
- Hung, S.-H., Chen, W.-P., & Chiao, L.-Y. (2011). A data-adaptive, multiscale approach of finite-frequency, travelttime tomography with special reference to P and S wave data

- from central Tibet. *Journal of Geophysical Research*, 116(B6), 1–26. doi:10.1029/2010JB008190
- Immenhauser, A., Buhl, D., Richter, D. K., Niedermayr, A., Riechelmann, D., Dietzel, M., & Schulte, U. (2010). Magnesium-isotope fractionation during low-Mg calcite precipitation in a limestone cave – Field study and experiments. *Geochimica et Cosmochimica Acta*, 74(15), 4346–4364. doi:10.1016/j.gca.2010.05.006
- Irvine, T. N. & Baragar, W. R. A. (1971). A guide to the chemical classification of the common volcanic rocks. *Canadian Journal of Earth Sciences*, 8(5), 523–548. doi:10.1139/e71-055
- Jellinek, A. M. & DePaolo, D. J. (2003). A model for the origin of large silicic magma chambers: precursors of caldera-forming eruptions. *Bulletin of Volcanology*, 65(5), 363–381. doi:10.1007/s00445-003-0277-y
- Johnson, D. M., Hooper, P. R., & Conrey, R. M. (1999). XRF analysis of rocks and minerals for major and trace elements on a single low dilution Li-tetraborate fused bead. *Advances in X-ray Analysis*, 41, 843–867.
- Jourdan, F., Bertrand, H., Scharer, U., Blichert-Toft, J., Feraud, G., & Kampunzu, a. B. (2007). Major and trace element and Sr, Nd, Hf, and Pb isotope compositions of the Karoo Large Igneous Province, Botswana-Zimbabwe: lithosphere vs mantle plume contribution. *Journal of Petrology*, 48(6), 1043–1077. doi:10.1093/petrology/egm010
- Kapp, J. L. D., Harrison, T. M., Kapp, P., Grove, M., & Lovera, O. M. (2005). Nyainqentanglha Shan: A window into the tectonic, thermal, and geochemical evolution of the Lhasa block, southern Tibet. *Journal of Geophysical Research*, 110(B8), 1–23. doi:10.1029/2004JB003330
- Kapp, P., DeCelles, P. G., Leier, A. L., Fabijanic, J. M., He, S., Pullen, A., & Gehrels, G. E. (2007). The Gangdese retroarc thrust belt revealed. *GSA Today*, 17(7), 4. doi:10.1130/GSAT01707A.1
- Kay, R. W. & Kay, S. M. (1993). Delamination and delamination magmatism. *Tectonophysics*, 219(1-3), 177–189.
- Kemp, A. I. S., Hawkesworth, C. J., Collins, W. J., Gray, C. M., & Blevin, P. L. (2009). Isotopic evidence for rapid continental growth in an extensional accretionary orogen: The Tasmanides, eastern Australia. *Earth and Planetary Science Letters*, 284(3-4), 455–466. doi:10.1016/j.epsl.2009.05.011
- Kempton, P. D., Fitton, J. G., Hawkesworth, C. J., & Ormerod, D. S. (1991). Isotopic and Trace-Element Constraints on the Composition and Evolution of the Lithosphere beneath the Southwestern United-States. *Journal of Geophysical Research-Solid Earth and Planets*, 96(B8), 13713–13735.
- Keshav, S., Gudfinnsson, G. H., Sen, G., & Fei, Y. (2004). High-pressure melting experiments on garnet clinopyroxenite and the alkalic to tholeiitic transition in ocean-island basalts. *Earth and Planetary Science Letters*, 223(3-4), 365–379. doi:10.1016/j.epsl.2004.04.029
- King, S. D. (2007). Hotspots and edge-driven convection. *Geology*, 35(3), 223. doi:10.1130/G23291A.1

- King, S. D. & Anderson, D. L. (1998). Edge-driven convection. *Earth and Planetary Science Letters*, 160(3-4), 289–296.
- King, S. D. & Ritsema, J. (2000). African Hot Spot Volcanism: Small-Scale Convection in the Upper Mantle Beneath Cratons. *Science*, 290(5494), 1137–1140. doi:10.1126/science.290.5494.1137
- Kistler, R. W. & Peterman, Z. E. (1978). Reconstruction of crustal blocks Of California on the basis of initial strontium isotopic compositions Of Mesozoic granitic rocks. U.S. Geological Survey Professional Paper 1071.
- Kogiso, T. & Hirschmann, M. M. (2006). Partial melting experiments of bimineralec eclogite and the role of recycled mafic oceanic crust in the genesis of ocean island basalts. *Earth and Planetary Science Letters*, 249(3-4), 188–199. doi:10.1016/j.epsl.2006.07.016
- Kogiso, T., Hirschmann, M. M., & Frost, D. J. (2003). High-pressure partial melting of garnet pyroxenite: possible mafic lithologies in the source of ocean island basalts. *Earth and Planetary Science Letters*, 216(4), 603–617. doi:10.1016/S0012-821X(03)00538-7
- Kreissig, K. & Elliott, T. (2005). Ca isotope fingerprints of early crust-mantle evolution. *Geochimica et Cosmochimica Acta*, 69(1), 165–176. doi:10.1016/j.gca.2004.06.026
- Krystopowicz, N. J. & Currie, C. A. (2013). Crustal eclogitization and lithosphere delamination in orogens. *Earth and Planetary Science Letters*, 361, 195–207. doi:10.1016/j.epsl.2012.09.056
- Kurz, M. D. (1986a). Cosmogenic helium in a terrestrial igneous rock. *Nature*, 320(6061), 435–439.
- Kurz, M. D. (1986b). In situ Production of Terrestrial Cosmogenic Helium and Some Applications to Geochronology. *Geochimica Et Cosmochimica Acta*, 50(12), 2855–2862.
- Kurz, M. D., Curtice, J., Lott, D. E., & Solow, A. (2004). Rapid helium isotopic variability in Mauna Kea shield lavas from the Hawaiian Scientific Drilling Project. *Geochemistry Geophysics Geosystems*, 5(4), Q04G14. doi:10.1029/2002GC000439
- Kushiro, I. (1996). Partial melting of a fertile mantle peridotite at high pressures: an experimental study using aggregates of diamond. In A. Basu & S. R. Hart (Eds.), *Earth processes: reading the isotopic code* (Geophysical Monograph, Vol. 95, pp. 109–122). American Geophysical Union. doi:10.1029/GM095p0109
- Lambart, S., Laporte, D., Provost, A., & Schiano, P. (2012). Fate of Pyroxenite-derived melts in the peridotitic mantle: thermodynamic and experimental constraints. *Journal of Petrology*, 53(3), 451–476. doi:10.1093/petrology/egr068
- Lambart, S., Laporte, D., & Schiano, P. (2013). Markers of the pyroxenite contribution in the major-element compositions of oceanic basalts: Review of the experimental constraints. *Lithos*, 160-161, 14–36. doi:10.1016/j.lithos.2012.11.018
- Lastowka, L. A., Sheehan, A. F., & Schneider, J. M. (2001). Seismic evidence for partial lithospheric delamination model of colorado plateau uplift. *Geophysical Research Letters*, 28(7), 1319–1322.
- Laughlin, A. W., Perry, F. V., Damon, P. E., Shafiqullah, M., WoldeGabriel, G., McIntosh, W., ... Drake, P. G. (1993). Geochronology of Mount Taylor, Cebollita Mesa, and

- Zuni-Bandera volcanic fields, Cibola County, New Mexico. *New Mexico Geology*, 15(4), 81–92.
- Le Bas, M. J. & Streckeisen, A. L. (1991). The IUGS systematics of igneous rocks. *Journal of the Geological Society*, 148(5), 825–833. doi:10.1144/gsjgs.148.5.0825
- Le Roux, V., Lee, C.-T. A., & Turner, S. (2010). Zn/Fe systematics in mafic and ultramafic systems: Implications for detecting major element heterogeneities in the Earth's mantle. *Geochimica et Cosmochimica Acta*, 74(9), 2779–2796. doi:10.1016/j.gca.2010.02.004
- Lee, C.-T. A., Luffi, P., Plank, T., Dalton, H., & Leeman, W. P. (2009). Constraints on the depths and temperatures of basaltic magma generation on Earth and other terrestrial planets using new thermobarometers for mafic magmas. *Earth and Planetary Science Letters*, 279(1-2), 20–33. doi:10.1016/j.epsl.2008.12.020
- Lee, J., Hacker, B. R., Dinklage, W. S., Wang, Y., Gans, P., Calvert, A., ... McClelland, W. (2000). Evolution of the Kangmar Dome, southern Tibet: Structural, petrologic, and thermochronologic constraints. *Tectonics*, 19(5), 872–895.
- Lee, T.-Y. & Lawver, L. A. (1995). Cenozoic plate reconstruction of Southeast Asia. *Tectonophysics*, 251(1-4), 85–138.
- Levander, A. & Miller, M. S. (2012). Evolutionary aspects of lithosphere discontinuity structure in the western U.S. *Geochemistry, Geophysics, Geosystems*, 13(7), n/a–n/a. doi:10.1029/2012GC004056
- Levander, A., Schmandt, B., Miller, M. S., Liu, K., Karlstrom, K. E., Crow, R. S., ... Humphreys, E. (2011). Continuing Colorado plateau uplift by delamination-style convective lithospheric downwelling. *Nature*, 472(7344), 461–5. doi:10.1038/nature10001
- Li, W., Chakraborty, S., Beard, B. L., Romanek, C. S., & Johnson, C. M. (2012). Magnesium isotope fractionation during precipitation of inorganic calcite under laboratory conditions. *Earth and Planetary Science Letters*, 333–334, 304–316. doi:10.1016/j.epsl.2012.04.010
- Li, W.-Y., Teng, F.-Z., Ke, S., Rudnick, R. L., Gao, S., Wu, F.-Y., & Chappell, B. W. (2010). Heterogeneous magnesium isotopic composition of the upper continental crust. *Geochimica et Cosmochimica Acta*, 74(23), 6867–6884. doi:10.1016/j.gca.2010.08.030
- Li, W.-Y., Teng, F.-Z., Xiao, Y., & Huang, J. (2011). High-temperature inter-mineral magnesium isotope fractionation in eclogite from the Dabie orogen, China. *Earth and Planetary Science Letters*, 304(1–2), 224–230. doi:10.1016/j.epsl.2011.01.035
- Li, Z.-X. A., Lee, C.-T. A., Peslier, A. H., Lenardic, A., & Mackwell, S. J. (2008). Water contents in mantle xenoliths from the Colorado Plateau and vicinity: Implications for the mantle rheology and hydration-induced thinning of continental lithosphere. *Journal of Geophysical Research*, 113, B09210. doi:10.1029/2007JB005540
- Liu, Q. S., Jiang, W., Jian, P., Ye, P. S., Wu, Z. H., & Hu, D. G. (2006). The zircon SHRIMP U–Pb age and petrochemical and geochemical features of Mesozoic muscovite monzogranite at Ningzhong, Tibet. *Acta Petrologica Sinica*, 22, 643–652.

- Lustrino, M. (2005). How the delamination and detachment of lower crust can influence basaltic magmatism. *Earth-Science Reviews*, 72(1-2), 21–38. doi:10.1016/j.earscirev.2005.03.004
- Ma, L., Wang, Q., Wyman, D. A., Jiang, Z.-Q., Yang, J. H., Li, Q.-L., . . . Guo, H.-F. (2013). Late Cretaceous crustal growth in the Gangdese area, southern Tibet: Petrological and Sr–Nd–Hf–O isotopic evidence from Zhengga diorite-gabbro. *Chemical Geology*, 349–350, 54–70. doi:10.1016/j.chemgeo.2013.04.005
- Mallik, A. & Dasgupta, R. (2012). Reaction between MORB-eclogite derived melts and fertile peridotite and generation of ocean island basalts. *Earth and Planetary Science Letters*, 329–330, 97–108. doi:10.1016/j.epsl.2012.02.007
- Malpas, J., Zhou, M.-F., Robinson, P. T., & Reynolds, P. H. (2003). Geochemical and geochronological constraints on the origin and emplacement of the Yarlung Zangbo ophiolites, Southern Tibet. In Y. Dilek & P. T. Robinson (Eds.), *Ophiolites in earth history* (Geological Society of London Special Publication, Vol. 218, pp. 191–206). Geological Society of London. doi:10.1144/GSL.SP.2003.218.01.11
- Marshall, B. D. & DePaolo, D. J. (1982). Precise age determinations and petrogenetic studies using the K-Ca method. *Geochimica Et Cosmochimica Acta*, 46, 2537–2545.
- Marshall, B. D. & DePaolo, D. J. (1989). Calcium isotopes in igneous rocks and the origin of granite. *Geochimica Et Cosmochimica Acta*, 53, 917–922.
- Marziano, G. I., Gaillard, F., & Pichavant, M. (2007). Limestone assimilation and the origin of CO₂ emissions at the Alban Hills (Central Italy): Constraints from experimental petrology. *Journal of Volcanology and Geothermal Research*, 166, 91–105.
- Marziano, G. I., Gaillard, F., & Pichavant, M. (2008). Limestone assimilation by basaltic magmas: an experimental re-assessment and application to Italian volcanoes. *Contributions to Mineralogy and Petrology*, 155, 719–738. doi:10.1007/s00410-007-0267-8
- McDonough, W. F. & Sun, S.-S. (1995). The Composition of the Earth. *Chemical Geology*, 120(3-4), 223–253.
- Moore, R. B. & Wolfe, E. W. (1987). Geologic map of the east part of the San Francisco volcanic field, north-central Arizona. USGS Miscellaneous Field Studies Map MF-1960.
- Morgan, P., Sass, J. H., Duffield, W., Fleger, T., Fry, B. N., & Peters, L. (2004). *Geothermal Resource Evaluation Program of the eastern San Francisco Volcanic Field, Arizona* (tech. rep. No. 928). Department of Energy.
- Mullaney, K. (1996). *Petrology and geochemistry of lavas from cinder cones along alignments in the SP region of the San Francisco Volcanic Field, Flagstaff, Arizona* (Master's thesis, University of Massachusetts at Amherst).
- Nelson, B. K. & DePaolo, D. J. (1985). Rapid Production of Continental Crust 1.7 to 1.9 B.Y. Ago – Nd Isotopic Evidence from the Basement of the North-American Mid-Continent. *Geological Society of America Bulletin*, 96(6), 746–754.
- Newhall, C. G., Ulrich, G. E., & Wolfe, E. W. (1987). Geologic map of the southwest part of the San Francisco volcanic field, north-central Arizona. Miscellaneous Field Studies Map MF-1958.

- Nielsen, L. C., Druhan, J. L., Yang, W., Brown, S. T., & DePaolo, D. J. (2012). Calcium Isotopes as Tracers of Biogeochemical Processes. In M. Baskaran (Ed.), *Handbook of environmental isotope geochemistry* (Vol. 1, pp. 105–124). Springer Berlin Heidelberg. doi:10.1007/978-3-642-10637-8_7
- O’Neil, J. R. & Chappell, B. W. (1977). Oxygen and hydrogen isotope relations in the Berridale batholith. *Journal of the Geological Society*, *133*(6), 559–571. doi:10.1144/gsjgs.133.6.0559
- Ort, M. H., Elson, M. D., & Champion, D. E. (2002). *A paleomagnetic dating study of Sunset Crater Volcano* (tech. rep. No. 2002-16). Center for Desert Archaeology.
- Perry, F. V., Baldrige, W. S., & DePaolo, D. J. (1987). Role of asthenosphere and lithosphere in the genesis of Late Cenozoic basaltic rocks from the Rio Grande Rift and adjacent regions of the southwestern United States. *Journal of Geophysical Research*, *92*(B9), 9193. doi:10.1029/JB092iB09p09193
- Perry, F. V., Baldrige, W. S., DePaolo, D. J., & Shafiqullah, M. (1990). Evolution of a magmatic system during continental extension: the Mount Taylor Volcanic Field, New Mexico. *Journal of Geophysical Research*, *95*(B12), 19327–19348.
- Perry, F. V., Crowe, B. M., Valentine, G. A., & Bowker, L. M. (1998). *Volcanism studies: final report for the Yucca Mountain Project* (tech. rep. No. LA-13478). Los Alamos National Laboratory. Los Alamos. doi:10.2172/12111
- Perry, F. V., Depaolo, D. J., & Baldrige, W. S. (1993). Neodymium isotopic evidence for decreasing crustal contributions to Cenozoic ignimbrites of the western United States: Implications for the thermal evolution of the Cordilleran crust. *Geological Society of America Bulletin*, *105*(7), 872–882. doi:10.1130/0016-7606(1993)105(0872:NIEFDC)2.3.CO;2
- Pertermann, M. & Hirschmann, M. M. (2003). Anhydrous partial melting experiments on MORB-like eclogite: phase relations, phase compositions and mineral-melt partitioning of major elements at 2–3 GPa. *Journal of Petrology*, *44*(12), 2173–2201. doi:10.1093/petrology/egg074
- Plank, T. F., Spiegelman, M., & Langmuir, C. H. (1995). The meaning of “mean F”: clarifying the mean extent of melting at ocean ridges. *Journal of Geophysical Research*, *100*(B8), 15045–15052.
- Pogge von Strandmann, P. A. E. (2008). Precise magnesium isotope measurements in core top planktic and benthic foraminifera. *Geochemistry Geophysics Geosystems*, *9*(12). doi:10.1029/2008GC002209
- Poitrasson, F. & Freydier, R. (2005). Heavy iron isotope composition of granites determined by high resolution MC-ICP-MS. *Chemical Geology*, *222*, 132–147. doi:10.1016/j.chemgeo.2005.07.005
- Raddick, M. J. (2002). Buoyant decompression melting: A possible mechanism for intraplate volcanism. *Journal of Geophysical Research*, *107*(B10), 2228.
- Reid, M. R., Bouchet, R. A., Blichert-Toft, J., Levander, A., Liu, K., Miller, M. S., & Ramos, F. C. (2012). Melting under the Colorado Plateau, USA. *Geology*, *40*(5), 387–390. doi:10.1130/G32619.1

- Reiners, P. W. & Ehlers, T. A. (Eds.). (2005). *Low-Temperature Thermochronology: Techniques, Interpretations, and Applications*. Reviews in Mineralogy and Geochemistry, Vol. 58. Mineralogical Society of America.
- Reiners, P. W., Nelson, B. K., & Ghiorso, M. S. (1995). Assimilation of felsic crust by basaltic magma: Thermal limits and extents of crustal contamination of mantle-derived magmas. *Geology*, *23*(6), 563–566. doi:10.1130/0091-7613(1995)023<0563
- Richter, F. M., Watson, E. B., Mendybaev, R. A., Teng, F.-Z., & Janney, P. E. (2008). Magnesium isotope fractionation in silicate melts by chemical and thermal diffusion. *Geochimica Et Cosmochimica Acta*, *72*(1), 206–220.
- Ritter, J. R. R., Jordan, M., Christensen, U. R., & Achauer, U. (2001). A mantle plume below the Eifel volcanic fields, Germany. *Earth and Planetary Science Letters*, *186*, 7–14. doi:10.1016/S0012-821X(01)00226-6
- Robinson, H. H. (1913). The San Francisco volcanic field, Arizona. U.S. Geological Survey Professional Paper 76.
- Roy, M., Jordan, T. H., & Pederson, J. (2009). Colorado Plateau magmatism and uplift by warming of heterogeneous lithosphere. *Nature*, *459*(7249), 978–82. doi:10.1038/nature08052
- Royden, L. H., Burchfiel, B. C., & van der Hilst, R. D. (2008). The Geological Evolution of the Tibetan Plateau. *Science*, *321*, 1054–1058. doi:10.1126/science.1155371
- Rudge, J. F., Reynolds, B. C., & Bourdon, B. (2009). The double spike toolbox. *Chemical Geology*, *265*, 420–431. doi:10.1016/j.chemgeo.2009.05.010
- Rudnick, R. L. & Gao, S. (2003). Composition of the Continental Crust. In R. L. Rudnick (Ed.), *The Crust* (Treatise on Geochemistry, Vol. 3, pp. 1–64). Elsevier-Pergamon. doi:10.1016/B0-08-043751-6/03016-4
- Salters, V. J. M. & Longhi, J. (1999). Trace element partitioning during the initial stages of melting beneath mid-ocean ridges. *Earth and Planetary Science Letters*, *166*(1-2), 15–30. doi:10.1016/S0012-821X(98)00271-4
- Salters, V. J. M. & Stracke, A. (2004). Composition of the depleted mantle. *Geochemistry Geophysics Geosystems*, *5*, Q05B07.
- Schärer, U. and Xu, R.-H. and Allègre, C. J. (1986). U-(Th)-Pb systematics and ages of Himalayan leucogranites, South Tibet. *Earth and Planetary Science Letters*, *77*, 35–48.
- Schmandt, B. & Humphreys, E. (2010). Complex subduction and small-scale convection revealed by body-wave tomography of the western United States upper mantle. *Earth and Planetary Science Letters*, *297*(3-4), 435–445. doi:10.1016/j.epsl.2010.06.047
- Schmitz, M. D., Vervoort, J. D., Bowring, S. A., & Patchett, P. J. (2004). Decoupling of the Lu-Hf and Sm-Nd isotope systems during the evolution of granulitic lower crust beneath southern Africa. *Geology*, *32*(5), 405. doi:10.1130/G20241.1
- Sharp, W. D. & Renne, P. R. (2004). The $^{40}\text{Ar}/^{39}\text{Ar}$ dating of core recovered by the Hawaii Scientific Drilling Project (phase 2), Hilo, Hawaii. *Geochemistry Geophysics Geosystems*, *6*(4), Q04G17. doi:10.1029/2004GC000846

- Shaw, D. M. (1970). Trace element fractionation during anatexis. *Geochimica Et Cosmochimica Acta*, *34*, 237–243.
- Shen, B., Jacobsen, B., Lee, C.-T. A., Yin, Q.-Z., & Morton, D. M. (2009). The Mg isotopic systematics of granitoids in continental arcs and implications for the role of chemical weathering in crust formation. *Proceedings of the National Academy of Sciences*, *106*(49), 20652–20657. doi:10.1073/pnas.0910663106
- Shuster, D. L., Farley, K. A., Sisterson, J. M., & Burnett, D. S. (2003). Quantifying the diffusion kinetics and spatial distributions of radiogenic He-4 in minerals containing proton-induced He-3. *Earth and Planetary Science Letters*, *217*(1-2), 19–32.
- Simon, J. I. & DePaolo, D. J. (2010). Stable calcium isotopic composition of meteorites and rocky planets. *Earth and Planetary Science Letters*, *289*(3-4), 457–466. doi:10.1016/j.epsl.2009.11.035
- Simon, J. I., DePaolo, D. J., & Moynier, F. (2009). Calcium Isotope Composition of Meteorites, Earth, and Mars. *The Astrophysical Journal*, *702*(1), 707–715. doi:10.1088/0004-637X/702/1/707
- Sims, K. W. W., DePaolo, D. J., Murrell, M. T., Baldrige, W. S., Goldstein, S., Clague, D., & Jull, M. (1999). Porosity of the melting zone and variations in the solid mantle upwelling rate beneath Hawaii: Inferences from ^{238}U - ^{230}Th - ^{226}Ra and ^{235}U - ^{231}Pa disequilibrium. *Geochimica Et Cosmochimica Acta*, *63*(23), 4119–4138. doi:10.1016/S0016-7037(99)00313-0
- Sine, C. R., Wilson, D., Gao, W., Grand, S. P., Aster, R., Ni, J., & Baldrige, W. S. (2008). Mantle structure beneath the western edge of the Colorado Plateau. *Geophysical Research Letters*, *35*(10), L10303.
- Sisson, T. W., Kimura, J.-I., & Coombs, M. L. (2009). Basanite–nephelinite suite from early Kilauea: carbonated melts of phlogopite–garnet peridotite at Hawaii’s leading magmatic edge. *Contributions to Mineralogy and Petrology*, *158*(6), 803–829. doi:10.1007/s00410-009-0411-8
- Skulan, J., DePaolo, D. J., & Owens, T. L. (1997). Biological control of calcium isotopic abundances in the global calcium cycle. *Geochimica et Cosmochimica Acta*, *61*(12), 2505–2510. doi:10.1016/S0016-7037(97)00047-1
- Smiley, T. C. (1958). The geology and dating of Sunset Crater, Flagstaff, Arizona. In R. Y. Anderson & J. W. Harshbarger (Eds.), *9th Field Conference Guidebook of the Black Mesa Basin* (pp. 186–190). New Mexico Geologic Society.
- Smith, D. & Griffin, W. L. (2005). Garnetite xenoliths and mantle-water interactions below the Colorado Plateau, southwestern United States. *Journal of Petrology*, *46*(9), 1901–1924. doi:10.1093/petrology/egi042
- Smith, P. M. & Asimow, P. D. (2005). Adibat_1ph: A new public front-end to the MELTS, pMELTS, and pHMELTS models. *Geochemistry, Geophysics, Geosystems*, *6*(2), Q02004. doi:10.1029/2004GC000816
- Spandler, C., Yaxley, G., Green, D. H., & Rosenthal, A. (2007). Phase relations and melting of anhydrous K-bearing eclogite from 1200 to 1600 C and 3 to 5 GPa. *Journal of Petrology*, *49*(4), 771–795. doi:10.1093/petrology/egm039

- Spera, F. J. & Bohron, W. A. (2004). Open-system magma chamber evolution: an energy-constrained geochemical model incorporating the effects of concurrent eruption, recharge, variable assimilation and fractional crystallization (EC-E'RA χ FC). *Journal of Petrology*, 45(12), 2459–2480.
- Stauber, D. A. (1982). Two-dimensional compressional wave velocity structure under San Francisco Volcanic Field, Arizona, from teleseismic-P residual measurements. *Journal of Geophysical Research*, 87(NB7), 5451–5459.
- Sun, S.-S. & McDonough, W. F. (1989). Chemical and isotopic systematics of oceanic basalts: Implications for mantle composition and processes. In A. D. Saunders & M. J. Norry (Eds.), *Magmatism in the ocean basins* (Geological Society of London Special Publication, Vol. 42, pp. 313–345). Geological Society of London. doi:10.1144/GSL.SP.1989.042.01.19
- Tackley, P. J. & Stevenson, D. J. (1993). A mechanism for spontaneous self-perpetuating volcanism on the terrestrial planets. In D. B. Stone & S. K. Runcorn (Eds.), *Flow and Creep in the Solar System: Observations, Modeling and Theory* (NATO Science Series, Vol. 100, pp. 307–321). Kluwer Academic Publishers.
- Tanaka, K. L., Shoemaker, E. M., Ulrich, G. E., & Wolfe, E. W. (1986). Migration of Volcanism in the San-Francisco Volcanic Field, Arizona. *Geological Society of America Bulletin*, 97(2), 129–141.
- Teng, F. Z., Wadhwa, M., & Helz, R. T. (2007). Investigation of magnesium isotope fractionation during basalt differentiation: Implications for a chondritic composition of the terrestrial mantle. *Earth and Planetary Science Letters*, 261(1-2), 84–92.
- Teng, F.-Z., Li, W.-Y., Ke, S., Marty, B., Dauphas, N., Huang, S., . . . Pourmand, A. (2010). Magnesium isotopic composition of the Earth and chondrites. *Geochimica et Cosmochimica Acta*, 74(14), 4150–4166. doi:10.1016/j.gca.2010.04.019
- Thompson, R. N., Riches, a. J. V., Antoshechkina, P. M., Pearson, D. G., Nowell, G. M., Ottley, C. J., . . . Niku-Paavola, V. (2007). Origin of CFB magmatism: multi-tiered intracrustal picrite-rhyolite magmatic plumbing at Spitzkoppe, western Namibia, during early Cretaceous Etendeka magmatism. *Journal of Petrology*, 48(6), 1119–1154. doi:10.1093/petrology/egm012
- Till, C. B., Grove, T. L., & Krawczynski, M. J. (2012). A melting model for variably depleted and enriched lherzolite in the plagioclase and spinel stability fields. *Journal of Geophysical Research*, 117(B6), B06206. doi:10.1029/2011JB009044
- Tipper, E. T., Gaillardet, J., Galy, A., Louvat, P., Bickle, M. J., & Capmas, F. (2010). Calcium isotope ratios in the world's largest rivers: A constraint on the maximum imbalance of oceanic calcium fluxes. *Global Biogeochemical Cycles*, 24, GB3019. doi:10.1029/2009GB003574
- Tipper, E. T., Louvat, P., Capmas, F., Galy, A., & Gaillardet, J. (2008). Accuracy of stable Mg and Ca isotope data obtained by MC-ICP-MS using the standard addition method. *Chemical Geology*, 257(1-2), 65–75.

- Tormey, D. R., Grove, T. L., & Bryan, W. B. (1987). Experimental petrology of normal MORB near the Kane Fracture Zone: 22-25 N, mid-Atlantic ridge. *Contributions to Mineralogy and Petrology*, *96*, 121–139.
- Trull, T. W. & Kurz, M. D. (1993). Experimental Measurements of He-3 and He-4 Mobility in Olivine and Clinopyroxene at Magmatic Temperatures. *Geochimica Et Cosmochimica Acta*, *57*(6), 1313–1324.
- Ulrich, G. E. & Bailey, N. G. (1987). Geologic map of the SP Mountain part of the San Francisco volcanic field, north-central Arizona. Miscellaneous Field Studies Map MF-1956.
- Valentine, G. A. (2012). Shallow plumbing systems for small-volume basaltic volcanoes, 2: Evidence from crustal xenoliths at scoria cones and maars. *Journal of Volcanology and Geothermal Research*, *223-224*, 47–63. doi:10.1016/j.jvolgeores.2012.01.012
- van Wijk, J. W., Baldrige, W. S., van Hunen, J., Goes, S., Aster, R., Coblenz, D. D., . . . Ni, J. (2010). Small-scale convection at the edge of the Colorado Plateau: Implications for topography, magmatism, and evolution of Proterozoic lithosphere. *Geology*, *38*(7), 611–614. doi:10.1130/G31031.1
- Vervoort, J. D., Patchett, J. P., Blichert-Toft, J., & Albarede, F. (1999). Relationships between Lu–Hf and Sm–Nd isotopic systems in the global sedimentary system. *Earth and Planetary Science Letters*, *168*, 79–99.
- Vielzeuf, D. & Schmidt, M. W. (2001). Melting relations in hydrous systems revisited: application to metapelites, metagreywackes and metabasalts. *Contributions to Mineralogy and Petrology*, *141*(3), 251–267. doi:10.1007/s004100100237
- Wagner, T., Lee, J., Hacker, B. R., & Seward, G. (2010). Kinematics and vorticity in Kangmar Dome, southern Tibet: Testing midcrustal channel flow models for the Himalaya. *Tectonics*, *29*(6), 1–26. doi:10.1029/2010TC002746
- Walter, M. J. (1998). Melting of garnet peridotite and the origin of komatiite and depleted lithosphere. *Journal of Petrology*, *39*(1), 29–60. doi:10.1093/petroj/39.1.29
- Wang, R., Xia, B., Zhou, G., Zhang, Y., Yang, Z., Li, W., . . . Xu, L. (2006). SHRIMP zircon U-Pb dating for gabbro from the Tiding ophiolite in Tibet. *Chinese Science Bulletin*, *51*(14), 1776–1779. doi:10.1007/s11434-006-2027-y
- Wang, X., Ni, J. F., Aster, R., Sandvol, E., Wilson, D., Sine, C., . . . Baldrige, W. S. (2008). Shear-wave splitting and mantle flow beneath the Colorado plateau and its boundary with the great basin. *Bulletin of the Seismological Society of America*, *98*(5), 2526–2532. doi:10.1785/0120080107
- Watkins, J. M., DePaolo, D. J., Huber, C., & Ryserson, F. J. (2009). Liquid composition-dependence of calcium isotope fractionation during diffusion on molten silicates. *Geochimica Et Cosmochimica Acta*, *73*, 7341–7359. doi:10.1016/j.gca.2009.09.004
- Watson, S. & McKenzie, D. (1991). Melt generation by plumes: a study of hawaiian volcanism. *Journal of Petrology*, *32*(3), 501–537. doi:10.1093/petrology/32.3.501
- Wen, D., Liu, D., Chung, S., Chu, M., Ji, J., Zhang, Q., . . . Lo, C. (2008). Zircon SHRIMP U–Pb ages of the Gangdese Batholith and implications for Neotethyan subduction in

- southern Tibet. *Chemical Geology*, 252(3-4), 191–201. doi:10.1016/j.chemgeo.2008.03.003
- Wendlandt, E., DePaolo, D. J., & Baldrige, W. S. (1993). Nd and Sr isotope chronostratigraphy of Colorado Plateau lithosphere: Implications for magmatic and tectonic underplating of the continental crust. *Earth and Planetary Science Letters*, 116, 23–43. doi:10.1016/0012-821X(93)90043-9
- Wendlandt, E., Depaolo, D. J., & Baldrige, W. S. (1996). Thermal history of Colorado Plateau lithosphere from Sm–Nd mineral geochronology of xenoliths. *Geological Society of America Bulletin*, 108(7), 757–767. doi:10.1130/0016-7606(1996)108<0757
- Wenrich-Verbeek, K. J. (1979). The petrogenesis and trace-element geochemistry of intermediate lavas from Humphreys Peak, San Francisco Volcanic Field, Arizona. *Tectonophysics*, 61, 103–129.
- White, S. M., Crisp, J. A., & Spera, F. J. (2006). Long-term volumetric eruption rates and magma budgets. *Geochemistry Geophysics Geosystems*, 7(3), Q03010. doi:10.1029/2005GC001002
- Wimpenny, J., Gíslason, S. R., James, R. H., Gannoun, A., Pogge Von Strandmann, P. A. E., & Burton, K. W. (2010). The behaviour of Li and Mg isotopes during primary phase dissolution and secondary mineral formation in basalt. *Geochimica et Cosmochimica Acta*, 74(18), 5259–5279. doi:10.1016/j.gca.2010.06.028
- Wittke, J. H., Smith, D., & Wooden, J. L. (1989). Origin of Sr, Nd and Pb Isotopic Systematics in High-Sr Basalts from Central Arizona. *Contributions to Mineralogy and Petrology*, 101(1), 57–68.
- Wolfe, C. J., Solomon, S. C., Laske, G., Collins, J. A., Detrick, R. S., Orcutt, J. A., ... Hauri, E. H. (2011). Mantle p-wave velocity structure beneath the hawaiian hotspot. *Earth and Planetary Science Letters*, 303(3-4), 267–280. doi:10.1016/j.epsl.2011.01.004
- Wolfe, E. W., Newhall, C. G., & Ulrich, G. E. (1987). Geologic map of the northwest part of the San Francisco Volcanic Field, north-central Arizona. USGS Miscellaneous Field Studies Map MF-1957.
- Wolfe, E. W., Ulrich, G. E., Holm, R. F., Moore, R. B., & Newhall, C. G. (1987). Geologic map of the central part of the San Francisco Volcanic Field, north-central Arizona. Miscellaneous Field Studies Map MF-1959.
- Wombacher, F., Eisenhauer, A., Heuser, A., & Weyer, S. (2009). Separation of Mg, Ca, and Fe from geological reference materials for stable isotope ratio analyses by MC-ICP-MS and double-spike TIMS. *Journal of Analytical Atomic Spectrometry*, 24, 627–636. doi:10.1039/b820154d
- Wood, C. A. & Kienle, J. (1990). *Volcanoes of north america* (C. A. Wood & J. Kienle, Eds.). Cambridge: Cambridge University Press.
- Xu, R.-H., Schärer, U., & Allègre, C. J. (1985). Magmatism and Metamorphism in the Lhasa Block (Tibet): A Geochronological Study. *The Journal of Geology*, 93(1), 41–57.
- Yin, A. & Harrison, T. M. (2000). Geologic Evolution of the Himalayan-Tibetan Orogen. *Annual Review of Earth and Planetary Sciences*, 28, 211–280.

- Yogodzinski, G. M., Naumann, T. R., Smith, E. I., Bradshaw, T. K., & Walker, J. D. (1996). Evolution of a mafic volcanic field in the central Great Basin, south central Nevada. *Journal of Geophysical Research*, *101*(B8), 17425–17445.
- Young, E. D. & Galy, A. (2004). The Isotope Geochemistry and Cosmochemistry of Magnesium. In C. M. Johnson, B. L. Beard, & F. Albarede (Eds.), *Geochemistry of non-traditional stable isotopes* (Chap. 6, Vol. 55, pp. 197–230). Mineralogical Society of America.
- Zandt, G., Myers, S. C., & Wallace, T. C. (1995). Crust and mantle structure across the Basin and Range Colorado Plateau boundary at 37°N latitude and implications for Cenozoic extensional mechanism. *Journal of Geophysical Research-Solid Earth*, *100*(B6), 10529–10548. doi:10.1029/94JB03063
- Zhao, Z., Mo, X., Dilek, Y., Niu, Y., DePaolo, D. J., Robinson, P., ... Hou, Z. (2009). Geochemical and Sr–Nd–Pb–O isotopic compositions of the post-collisional ultrapotassic magmatism in SW Tibet: Petrogenesis and implications for India intra-continental subduction beneath southern Tibet. *Lithos*, *113*(1-2), 190–212. doi:10.1016/j.lithos.2009.02.004
- Zhao, Z., Xuanxue, M. O., Zhang, S., Tieying, G. U. O., Zhou, S., Dong, G., & Wang, Y. (2001). Post-collisional magmatism in Wuyu basin, central Tibet: evidence for recycling of subducted Tethyan oceanic crust. *Science in China Series D: Earth Sciences*, *44*, 27–34.
- Zhou, S., Mo, X., Zhao, Z., Qiu, R., Niu, Y., Guo, T., & Zhang, S. (2010). $^{40}\text{Ar}/^{39}\text{Ar}$ geochronology of post-collisional volcanism in the middle Gangdese Belt, southern Tibet. *Journal of Asian Earth Sciences*, *37*(3), 246–258. doi:10.1016/j.jseaes.2009.08.011
- Zindler, A. & Hart, S. R. (1986). Chemical Geodynamics. *Annual Review of Earth and Planetary Sciences*, *14*, 493–571.